

Surface processes recorded by rocks and soils on Meridiani Planum, Mars: Microscopic Imager observations during Opportunity's first three extended missions

Ken E. Herkenhoff,¹ John Grotzinger,² Andrew H. Knoll,³ Scott M. McLennan,⁴ Catherine Weitz,⁵ Aileen Yingst,⁶ Robert Anderson,⁷ Brent A. Archinal,¹ Raymond E. Arvidson,⁸ Janet M. Barrett,¹ Kris J. Becker,¹ James F. Bell III,⁹ Charles Budney,⁷ Mary G. Chapman,¹ Debbie Cook,¹ Bethany Ehlmann,⁸ Brenda Franklin,⁷ Lisa R. Gaddis,¹ Donna M. Galuszka,¹ Patricia A. Garcia,¹ Paul Geissler,¹ Trent M. Hare,¹ Elpitha Howington-Kraus,¹ Jeffrey R. Johnson,¹ Laszlo Keszthelyi,¹ Randolph L. Kirk,¹ Peter Lanagan,¹⁰ Ella Mae Lee,¹ Craig Leff,⁷ Justin N. Maki,⁷ Kevin F. Mullins,¹ Timothy J. Parker,⁷ Bonnie L. Redding,¹ Mark R. Rosiek,¹ Michael H. Sims,¹¹ Laurence A. Soderblom,¹ Nicole Spanovich,⁷ Richard Springer,⁷ Steve W. Squyres,⁹ Daniel Stolper,² Robert M. Sucharski,¹ Tracie Sucharski,¹ Rob Sullivan,⁹ and James M. Torson¹

Received 1 February 2008; revised 23 April 2008; accepted 19 May 2008; published 6 November 2008.

[1] The Microscopic Imager (MI) on the Mars Exploration Rover Opportunity has returned images of Mars with higher resolution than any previous camera system, allowing detailed petrographic and sedimentological studies of the rocks and soils at the Meridiani Planum landing site. Designed to simulate a geologist's hand lens, the MI is mounted on Opportunity's instrument arm and can resolve objects 0.1 mm across or larger. This paper provides an overview of MI operations, data calibration, and analysis of MI data returned during the first 900 sols (Mars days) of the Opportunity landed mission. Analyses of Opportunity MI data have helped to resolve major questions about the origin of observed textures and features. These studies support eolian sediment transport, rather than impact surge processes, as the dominant depositional mechanism for Burns formation strata. MI stereo observations of a rock outcrop near the rim of Erebus Crater support the previous interpretation of similar sedimentary structures in Eagle Crater as being formed by surficial flow of liquid water. Well-sorted spherules dominate ripple surfaces on the Meridiani plains, and the size of spherules between ripples decreases by about 1 mm from north to south along Opportunity's traverse between Endurance and Erebus craters.

Citation: Herkenhoff, K. E., et al. (2008), Surface processes recorded by rocks and soils on Meridiani Planum, Mars: Microscopic Imager observations during Opportunity's first three extended missions, *J. Geophys. Res.*, *113*, E12S32, doi:10.1029/2008JE003100.

1. Introduction

[2] The Mars Exploration Rover (MER) mission includes two essentially identical rovers, Spirit and Opportunity

[Crisp *et al.*, 2003]. The Athena science payload [Squyres *et al.*, 2003] on each rover includes a Microscopic Imager (MI). The MI is a fixed-focus camera mounted on a mechanical arm called the Instrument Deployment Device

¹U.S. Geological Survey, Flagstaff, Arizona, USA.

²Division of Geological and Planetary Sciences, California Institute of Technology, Pasadena, California, USA.

³Department of Organismic and Evolutionary Biology, Harvard University, Cambridge, Massachusetts, USA.

⁴Department of Geosciences, State University of New York at Stony Brook, Stony Brook, New York, USA.

⁵Planetary Science Institute, Tucson, Arizona, USA.

⁶Department of Natural and Applied Sciences, University of Wisconsin, Green Bay, Wisconsin, USA.

⁷Jet Propulsion Laboratory, California Institute of Technology, Pasadena, California, USA.

⁸Department of Earth and Planetary Sciences, Washington University, St. Louis, Missouri, USA.

⁹Department of Astronomy, Cornell University, Ithaca, New York, USA.

¹⁰Lunar and Planetary Laboratory, University of Arizona, Tucson, Arizona, USA.

¹¹NASA Ames Research Center, Moffett Field, California, USA.

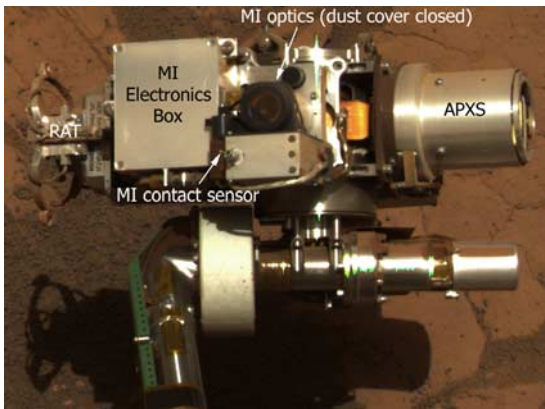


Figure 1. Pancam color (filters L4, L5, and L6) image of Opportunity's Instrument Deployment Device (IDD) turret (about 30 cm across), taken on sol 405 with illumination from top. Bright vertical lines are artifacts caused by blooming of saturated pixels.

(IDD). The MI includes the same charge-coupled device (CCD) detector and electronics as the other MER cameras [Bell *et al.*, 2003; Maki *et al.*, 2003]. MI images are 1024×1024 pixels in size, with a scale of 31 microns/pixel at best focus. The MI optics are protected by a retractable Kapton dust cover. The instrument includes a contact sensor that is used to accurately position the MI relative to rock targets (Figure 1). The camera design and experiment objectives were summarized by Herkenhoff *et al.* [2003].

[3] This paper provides an overview of Opportunity MI calibration, processing and analyses of data acquired through sol 900 (a sol is a Martian day, approximately 24 h and 40 min long). During the first 900 sols of the surface mission, the Opportunity rover acquired and returned hundreds of full-frame MI images (see http://pds-imaging.jpl.nasa.gov/Missions/Opportunity_MERB_mission.html or <http://an.rsl.wustl.edu/mer/merb/merb.htm> to search for and download Opportunity image data). Scientific results of the primary mission (through sol 90) were described previously [Squyres *et al.*, 2004a; Arvidson *et al.*, 2004; Herkenhoff *et al.*, 2004b], so this paper emphasizes the reduction and analysis of MI data acquired from sol 91 to 900 (during the first three extended missions). In addition, we provide further data analysis of observed textures related to grain size and lamina thickness for layered strata of the Burns formation [Grotzinger *et al.*, 2005]. These results support previous interpretations of the emplacement mechanisms for these strata.

[4] MI tactical operations, data processing, archiving, and high-level data products were discussed by Herkenhoff *et al.* [2006]. The MI on Opportunity is operated essentially identically to the MI on Spirit, and data are generally processed in the same way [Herkenhoff *et al.*, 2003], so that discussion is not repeated here.

2. In-Flight Calibration

[5] The results of MI calibration activities before the MER launches were summarized by Herkenhoff *et al.* [2003]; detailed information is available in the MI calibration report [Herkenhoff *et al.*, 2004a]. The collection and

application of Opportunity MI calibration data after launch (during cruise to Mars and the first 900 sols of landed operations) are described in this section.

2.1. Dark Current

[6] Because the MI has no shutter and its dust cover is not opaque, it is not possible to acquire useful MI dark current data on the surface of Mars. The MI is sensitive enough that starlight would affect nighttime images, and the dark current is difficult to measure at low temperatures, so we have not

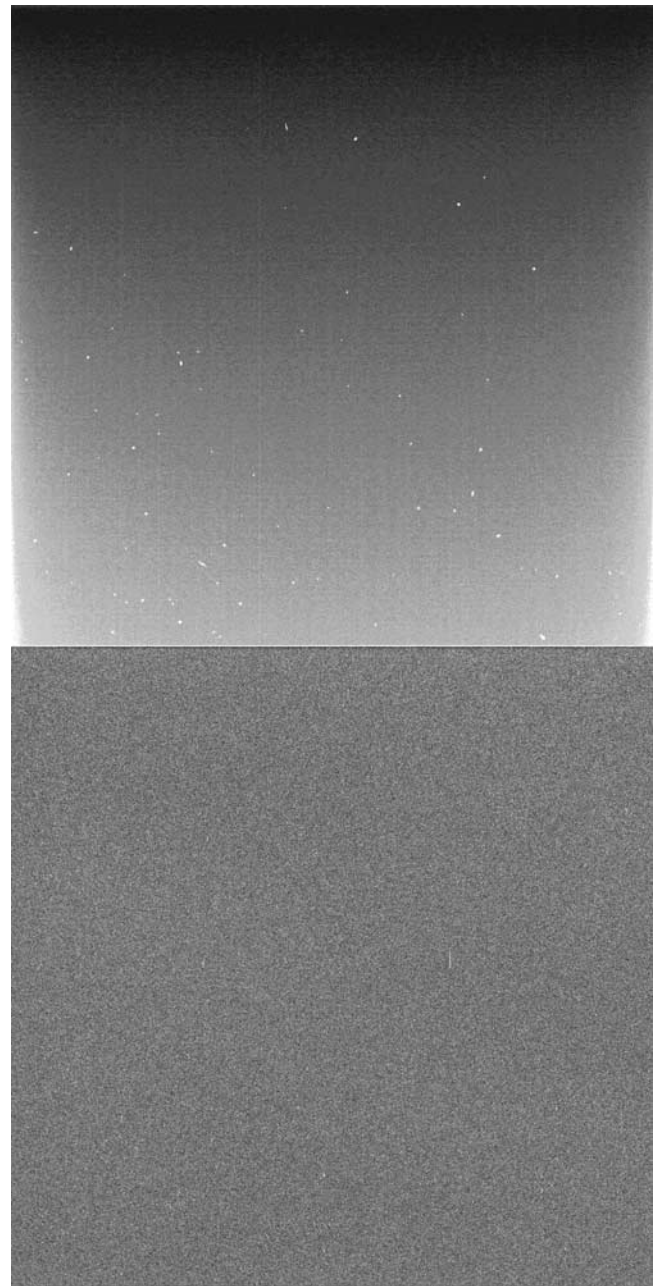


Figure 2. Microscopic Imager (MI) dark current images taken during first cruise instrument checkout on 30 July 2003. Contrast is enhanced to emphasize subtle features. (top) Zero-second exposure image 1M112776938 showing temporary radiation effects. (bottom) One hundred-second exposure image 1M112777598.

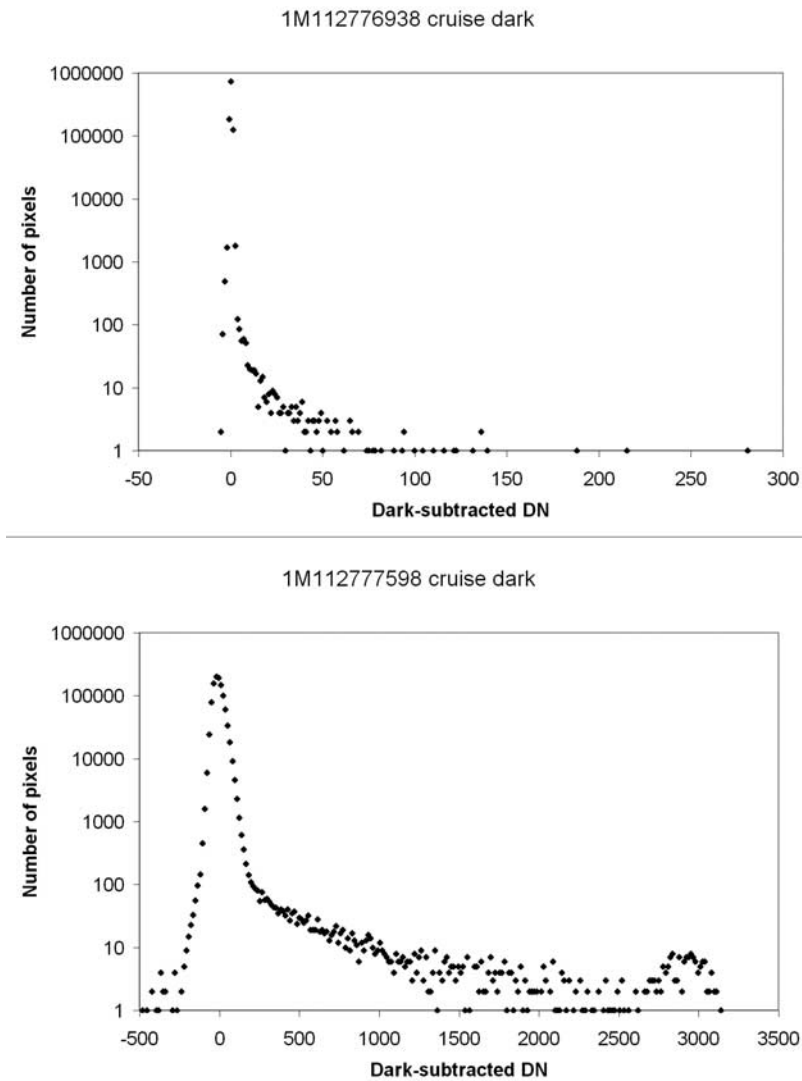


Figure 3. Histograms of MI dark current data acquired during first cruise instrument checkout on 30 July 2003. The MI dark current model was used to subtract average dark current variations from each image. (top) Zero-second exposure image. (bottom) One hundred-second exposure image.

attempted to acquire MI dark current data since Opportunity landed. However, dark current data were acquired twice during Opportunity's cruise to Mars, on 30 July and 4 December 2003. During cruise, Opportunity was encased in its aeroshell, and very little light was expected to illuminate the MI. Analysis of the MI data returned by the instrument checkout sequences indicates that no measurable light was incident on the camera (e.g., Figure 2). The temperature of the MI during the first checkout (CCD at -5.3°C) was higher than during the second checkout (CCD at -22.2°C), providing two data points to compare with the model for dark current temperature dependence. Full frame images and reference pixels were returned, losslessly compressed in each case. The cruise dark current observations are generally consistent with the dark current model developed using preflight calibration data [Herkenhoff *et al.*, 2004a]. Dark current data acquired after the MI was integrated onto the rover compare well with the standalone camera calibration data when the CCD temperature is decreased by 2.5°C . This

offset is likely due to the differences in how temperatures were recorded between preflight calibration and flight software.

[7] As expected, the cruise dark frames show the effects of radiation, probably from both the Mössbauer spectrometer and cosmic rays (Figure 2). These radiation sources generate spurious electrons in a few localized pixels, with typical peak amplitudes of a few 12-bit data numbers (DN) up to saturation (note vertical lines in the bottom of Figure 2 caused by "blooming" or spillover of excess charge into adjacent pixels). Such radiation effects are present in all MI data, but their low amplitude and random spatial distribution makes them very difficult to recognize in images of Mars. To evaluate the statistical effects of radiation on MI images, the MI dark current model [Herkenhoff *et al.*, 2004a] was used to subtract average dark current variations from the instrument checkout images. Histograms of the resulting image data are shown in Figure 3; the asymmetry in the histograms is primarily due to radiation effects. Assuming

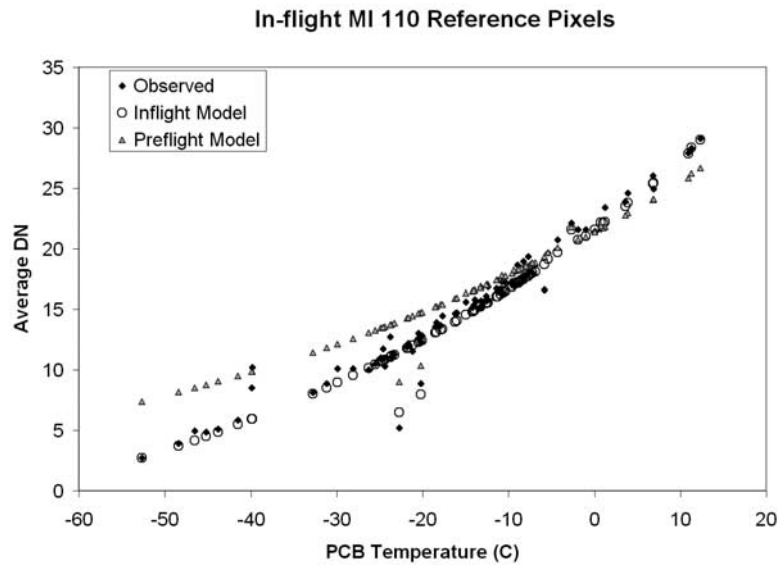


Figure 4. Average of observed reference pixel data in samples 4–14 and lines 412–612 compared with models based on preflight and in-flight calibration data. PCB is printed circuit board in the MI electronics box.

the shape of the histograms on the left side of the peaks represents the distribution of dark noise alone, radiation affects only 0.04% (~ 419) of the pixels in the 0 s dark frame (Figure 2, top). In this case, the CCD was affected by radiation only during the 5.2 ms frame transfer time and the 5.2 s readout time. More radiation effects accumulated during the 100 s dark frame (Figure 2, bottom), so that about 20% ($\sim 210,000$) of the pixels are affected by radiation and some of the pixels are saturated (see right side of Figure 3, bottom). The late-cruise dark data show similar levels of radiation effects. These results provide a crude estimate of the effects of radiation on MI data acquired on the surface of Mars: about 2000 pixels are affected per second of exposure time. This rate is expected to decrease during the mission as the Mössbauer reference source decays. Most Opportunity MI images were taken with exposure times of less than one second (maximum 1.8 s), so that less than 0.2% of the pixels in a typical MI image will be affected by radiation. Radiation statistics from the Spirit MI are essentially identical [Herkenhoff *et al.*, 2006].

[8] The zero-exposure dark images taken in cruise (Figure 2) also show linear features that are caused by a few slightly “hot” pixels being smeared during image transfer. While the capability exists in camera flight software to automatically correct such “bad” pixels on-board the rover, the magnitude of the spurious signal generated in these few pixels is too low to be a concern. Therefore, a table of bad pixel locations has not been loaded onto the rover and no correction is made.

[9] The MI CCD temperature was within the calibrated operating range (-55 to 5°C) for all images acquired during the first 340 sols of Opportunity’s mission. Later in the mission the CCD temperature sometimes exceeded 5°C , reaching 20°C on sol 560. The MI dark current model matches dark (including cruise checkout) data taken at up to 26°C and with exposure times less than 3 s to within 4 DN.

The dark current model was applied to the 100 s MI dark frame taken during the first cruise checkout, and reduced the standard deviation in a 101×101 pixel area at the center of the image from 91 DN to 47 DN. Similarly, the standard deviation in the same area in the 100 s dark frame taken during the second cruise checkout was reduced from 39 DN to 36 DN. These reductions in noise are not as great as seen when the model was applied to preflight dark images, due partly to a change in the “fixed” pattern of dark noise [Herkenhoff *et al.*, 2004a]; radiation also causes additional noise in the cruise data. Because MI images of the Martian surface were taken with exposure times of 1.8 s or less, the contribution of dark noise to relative calibration uncertainty is probably less than 4 DN. Therefore, in the absence of MI dark current data taken after landing, we conclude that dark current subtraction using the Opportunity MI dark current model contributes less than 4 DN to the uncertainty in both relative (pixel to pixel) and absolute radiometric calibration.

2.2. Reference Pixels

[10] The frame transfer CCD used in the MI shifts 1024-pixel lines, one at a time, into a serial register during image readout. The MER camera serial register includes 16 additional pixels at each end beyond the 1024 pixels used to receive image data from the CCD [Bell *et al.*, 2003]. These additional pixels are called “reference pixels” and they record the camera offset (or electronic bias, a constant value added to all image data) each time a line of pixels is read out of the MI. The offset of each camera can be adjusted by command, and the Opportunity MI (camera serial number 110) video offset was conservatively chosen to ensure that DN values would always exceed zero [Herkenhoff *et al.*, 2004a]. MI reference pixel data products were occasionally returned to Earth to verify that data clipping at 0 DN did not occur and to check the MI offset correction algorithm. The reference pixel data

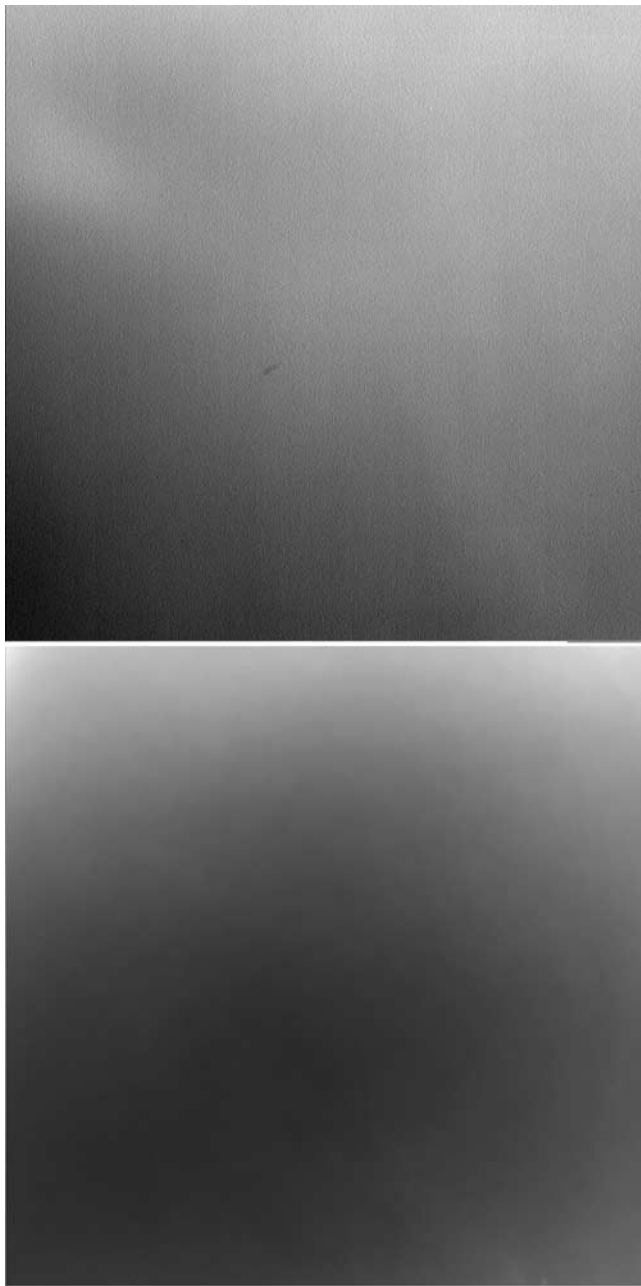


Figure 5. Sky flats acquired on sol 90. (top) MI image 1M136188650, taken with dust cover open and corrected for dark current. Note subtle structure near the upper left corner, possibly caused by scattering from the MI contact sensor or housing. (bottom) Radiometrically calibrated left Navcam image 1N136188772, acquired 2 min after the MI image. The field of view of the MI, about 24° , is entirely within the 45° field of view of the Navcam.

acquired after landing show that zero clipping did not occur. These data are compared with the reference pixel model developed using preflight calibration data in Figure 4. Reference pixel averages show a trend that is significantly different than the preflight data, with a standard deviation of 1.9 DN between the in-flight data and the model based on preflight data. A revised model, based on

the in-flight observations, fits the data much better, with a standard deviation of only 0.9 DN. The revised model has not been used to reprocess the MI images returned by Opportunity; we plan to analyze all the reference pixel data after the end of the mission before applying a new reference pixel model. The magnitude of the error in applying the preflight reference pixel model to in-flight MI data for which reference pixels were not returned is small (less than 1% for a well-exposed image).

[11] The variation in reference pixel values with line number changed during flight relative to the preflight calibration data, with a maximum standard deviation of

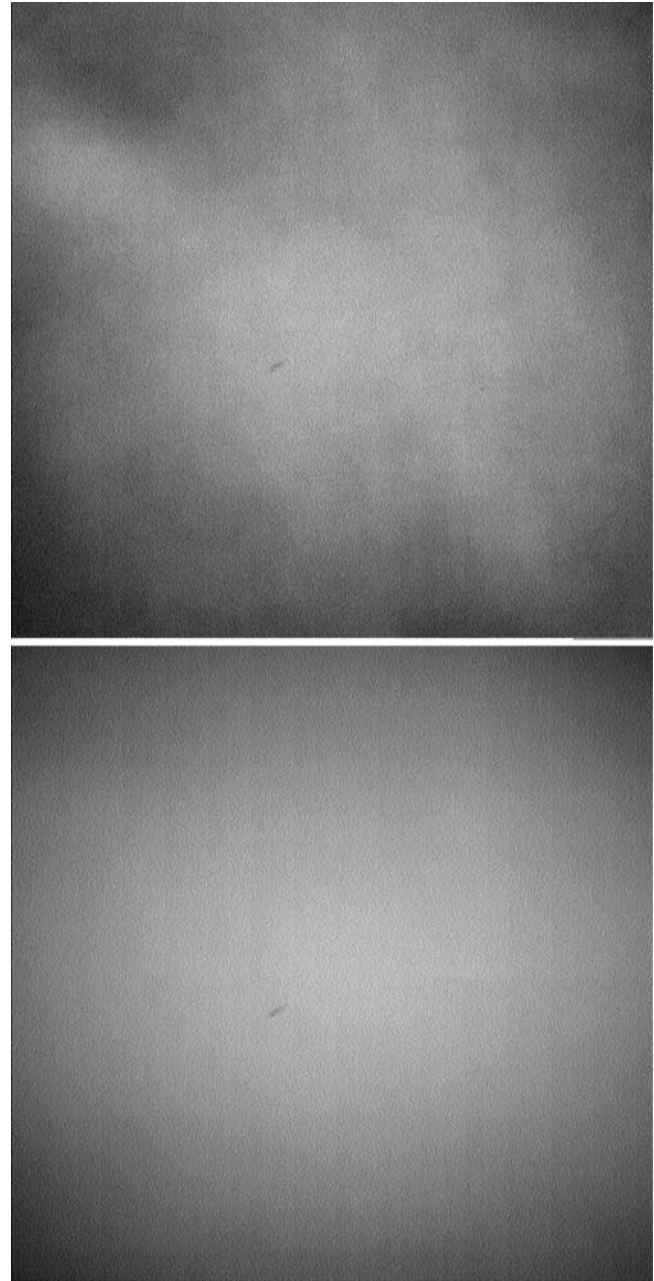


Figure 6. MI flat fields. (top) Processed sky flat acquired on sol 90. (bottom) Processed flat field acquired during preflight calibration. Note probable dust speck near center did not move after preflight calibration.



Figure 7. Ratio of dark-corrected sky flat taken with dust cover closed to dark-corrected sky flat taken with dust cover open. Both images acquired on sol 90. The vignetting at lower left is caused by black tape that was added to the MI dust cover to allow verification of cover state based on image data.

1.05 DN at line 1. Therefore, the maximum calibration error for MI images returned without simultaneous reference pixels (including dark current and offset errors described above) is about 4.2 DN.

2.3. Sky Flats

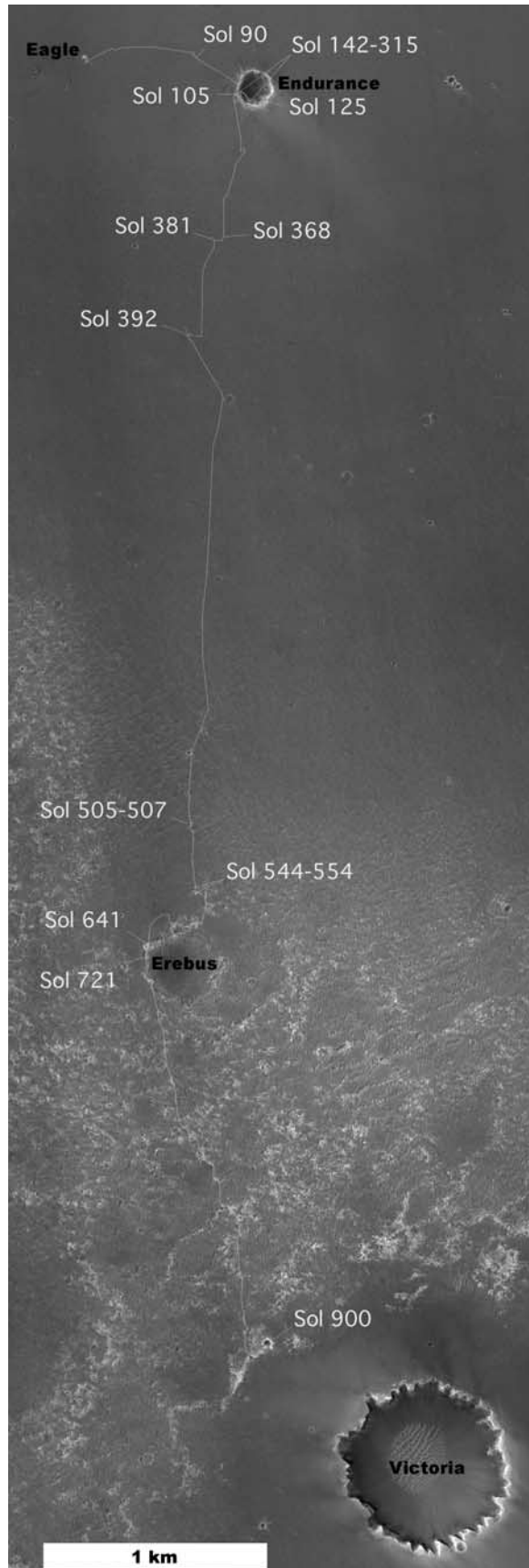
[12] As described in the MI calibration report [Herkenhoff *et al.*, 2004a], test schedule constraints did not allow flat field images to be acquired after integration of the MI dust cover. It was therefore necessary to determine the flat field sensitivity of the camera/dust cover combination using in-flight data. Images of the Martian sky, or “sky flats,” can be used as flat fields [Reid *et al.*, 1999] if variations in sky brightness can be quantified or modeled. To evaluate possible variations in sky brightness over the Opportunity landing site, Navigation Camera (Navcam) [Maki *et al.*, 2003] images were acquired at the same time as MI sky flats, showing the same patch of sky observed by the MI.

[13] The first set of MI/Navcam sky flats were acquired by Opportunity on sol 90, at the end of the primary mission. These sky flats were acquired at a solar scattering angle of 98° and showed no evidence of scattering of sunlight in the optics (Figure 5) and therefore were used to measure the flat field response of the MI with the dust cover open and closed. The MI sky flats were corrected for transfer smear by subtracting a “shutter” image onboard the rover, then corrected for dark current using the reference pixel data returned with the images and a model of the active area dark current. The left Navcam sky flat image was similarly processed and radiometrically calibrated by JPL’s Multi-mission Image Processing Laboratory (MIPL) [Alexander *et*

al., 2006], and the part of the image that viewed the same patch of sky as the MI sky flats was extracted. The Navcam sky flat was then low-pass-filtered to remove noise but preserve the variation in sky brightness across the image, and normalized to the average of the central 101×101 pixels. The dark-corrected MI sky flats were then divided by the low-pass-filtered, normalized Navcam sky flat to remove variations in sky brightness. The resulting image shows structure (Figure 6) not observed in preflight calibration data that is unlikely to be due to a change in response across the CCD. The difference between the normalized images shown in Figure 6 has a standard deviation of 0.9%, probably due (at least in part) to dust contamination of the MI optics. MI sky flats acquired on sols 367 and 697 were processed in the same way as the sol 90 sky flat and show similar but not exactly the same structure, perhaps indicating changes in dust contamination.

[14] We have not yet used the in-flight MI sky flats to update the flat field calibration files for the dust cover open state, pending analysis of more recently acquired sky flats. A ratio of the Pancam L3 (673 nm) and L5 (535 nm) [Bell *et al.*, 2003] sky images acquired on sol 697 shows a maximum 4% difference in the sky gradient, so the sky gradient at the Navcam effective wavelength (667 nm) [Soderblom *et al.*, 2008] is likely within 4% of the sky gradient at the MI effective wavelength (the difference in effective wavelength of the Pancam L3 and L5 filters is greater than the difference in the MI and Navcam effective wavelengths). Therefore, low-frequency errors in flat field correction using sky images are probably less than 4%.

[15] In order to determine the flat field response with the dust cover closed, sol 90 sky flats, taken with and without the dust cover, were corrected for dark current. The image taken through the dust cover was then divided by the image taken without the dust cover (Figure 7). MI images taken through the dust cover are radiometrically calibrated using the preflight data described above, then corrected for flat field by dividing by the ratio image. Close inspection of the sky images shows the effects of radiation; these effects have not yet been removed from the ratio image. The standard deviation of the central 101×101 pixels in the processed sol 90 sky flats is 3.0%, greater than the 2.8% standard deviation in the same region of preflight flat fields taken at room temperature [Herkenhoff *et al.*, 2004a]. Thermal noise should be less in the sol 90 sky flats (acquired when the CCD was at -5.4°C) than in the preflight flat fields taken under ambient conditions. The increase in noise is therefore probably caused by the radiation effects discussed above. Sky flats acquired on sol 367 (at a solar scattering angle of 120°) were processed in the same way and also have 3.0% noise in the central region. The difference between the sol 90 and sol 367 processed sky flats shows evidence of radiation effects, with a standard deviation of 0.9%. Hence, we use preflight flat field data to correct for pixel-to-pixel sensitivity variations in MI images, with the additional correction for images taken with the dust cover closed. When this calibration method is applied to the sol 90 sky flats, the noise in the central 101×101 pixels is reduced to 0.7%. This result indicates that the relative (pixel-to-pixel) radiometric calibration accuracy for this camera is better than 1%, except in localized areas where radiation contributes noise.



2.4. Calibration Accuracy

[16] The absolute radiometric accuracy of the Opportunity MI has been evaluated by comparing simultaneous images of the Martian sky obtained by Pancam and MI on sol 697. The radiance of the sky observed by Pancam and weighted by the spectral response of the MI is the same as the radiance measured by the MI to within 13%. The absolute radiometric calibration accuracy of the Pancam data is about 10% [Bell *et al.*, 2006]. We therefore conclude that the absolute radiometric accuracy of Opportunity MI data acquired through the first 3 extended missions is 20% or better [Herkenhoff *et al.*, 2004a].

[17] The relative (pixel-to-pixel) radiometric calibration accuracy is typically of greater interest to users of MI data, as it limits the ability to distinguish and measure small features in the images. On the basis of the results summarized above, the relative radiometric accuracy of well-exposed (>400 raw DN), calibrated MI data is $\pm 1.5\%$. The error in overall bias/offset correction when reference pixels are not returned with the image data is not included in this value, as it does not affect relative radiometric calibration accuracy.

[18] The MI data obtained during the first 900 sols of Opportunity's mission do not show any evidence for changes in geometric calibration at the level of accuracy measured before flight. Therefore, the geometric calibration results reported by Herkenhoff *et al.* [2004a] are believed to be valid: The Opportunity MI pixel scale is $30.5 \pm 0.9 \mu\text{m}$ and the radial distortion is less than 0.33 ± 0.03 pixels.

3. MI Communication Errors

[19] The MI is commanded by the rover computer over a serial communications interface. Between sols 176 and 826, Opportunity MI commands were not properly received 35 times. The rover flight software automatically resends commands that are not transmitted correctly, and in every case the commands were properly received on the second attempt. While these errors have not affected MI operations, they may be caused by degradation of the flex cable that connects the MI to the rover, or other hardware problems. Therefore the errors are a concern and have been studied by the MER engineering team. There are no clear correlations between the errors and IDD position, temperature, or frequency of imaging. The same communications interface is used to return MI data to the rover, so test images (constant DN) were used to diagnose the problem. However, these test images show only 3 flipped bits in dozens of images returned to date. This is puzzling, because the MI commands are much smaller (in terms of data volume transferred over the serial interface) than the test images. So while communication errors may have affected some MI images as they were transferred to the rover, such errors have not been detected. It appears

Figure 8. First 900 sols of Opportunity's traverse across Meridiani Planum, overlain on Mars Reconnaissance Orbiter High Resolution Imaging Science Experiment (HiRISE) image (illumination from lower left). Informal crater names shown in black.

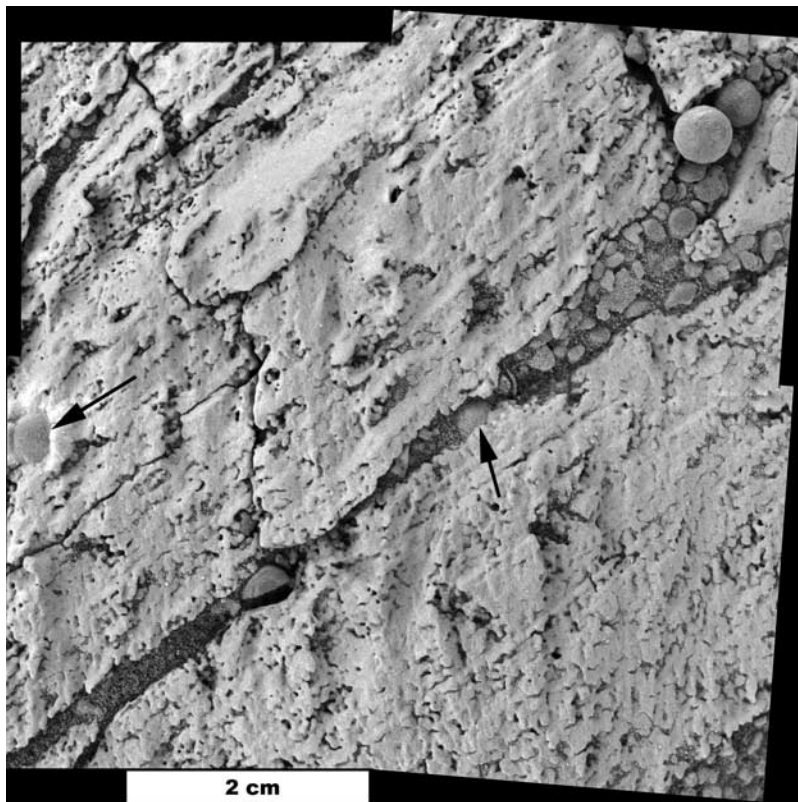


Figure 9. Mosaic of Siula Grande, taken on sol 142 with target in full shadow. Note embedded spherules (arrows) and laminae running through the target from lower left to upper right. Clast fragments lie within the topographic low at upper right.

unlikely that the cause of these errors will be found, as they are very infrequent.

4. Overview of Results

[20] The scientific results of MI observations acquired by Opportunity through sol 900 are summarized in this section. Results of the MI investigation during the first 90 sols of the Opportunity mission were summarized by *Herkenhoff et al.* [2004b] and have been discussed in several other publications [e.g., *Squyres et al.*, 2004a, 2004b; *Soderblom et al.*, 2004; *Grotzinger et al.*, 2005; *McLennan et al.*, 2005; *Sullivan et al.*, 2005; *Yen et al.*, 2005]. Observations of rocks on Meridiani Planum are discussed in section 4.1, followed by a discussion of soil observations. The locations at which the MI images shown in this paper were acquired are illustrated in Figure 8. In addition, the MI observed Opportunity's filter (F) and capture (C) magnets on sols 154 (F,C), 167 (F,C), 273 (F), 279 (C), 328 (C), 337 (C), 341 (F), and 538 (F). The MI was also used to image Opportunity's solar panels to assess contamination by dust and sand (see Table A1).

[21] As the MI was designed to mimic a geologist's hand lens, MI target surfaces were examined and analyzed using an approach similar to that used when observing hand samples in the field. Targets were characterized in terms of overall appearance (including location, context and color), lithology (mineralogy/composition as may be inferred by appearance, crystal form, cleavage, or unique mineral shape), surface texture (grain morphology and

appearance, size, sorting and fabric, including orientation), and a description of any sedimentary structures present. We divide our observations into soil targets and rock targets, where the term "target" refers to a specific point at which MI images were taken, and the term "feature" indicates a larger object (in the case of rocks) or region (in the case of soils) that may include several discrete targets.

4.1. Rock Observations and Classification

[22] During Opportunity's first phase of operation on Meridiani Planum, in Eagle and Endurance craters and points in between, the MER team established that the regional outcrop consists of sulfate-rich sandstones, deposited by wind, reworked locally by surface water, and cemented by minerals precipitated from acidic groundwater brines that percolated through accumulating sediments [*Squyres et al.*, 2004a, 2004b; *Squyres and Knoll*, 2005; *Clark et al.*, 2005; *McLennan et al.*, 2005; *Grotzinger et al.*, 2005]. Analyses of MI data played a major role in these discoveries, establishing that layered rocks consist of cemented sand grains, showing that many laminae in outcrop rocks are one or a few grains thick (a feature characteristic of eolian deposition), verifying that small-scale angles in bedding detected in Pancam images indeed reflect festoon cross-bedding, establishing the spatial and temporal relationships among sediment grains and diagenetic mineral phases, and characterizing the nature of critical microtextural features such as millimeter-scale spherules, grain sizes/shapes and secondary porosity. Early exploration also demonstrated that isolated cobbles and

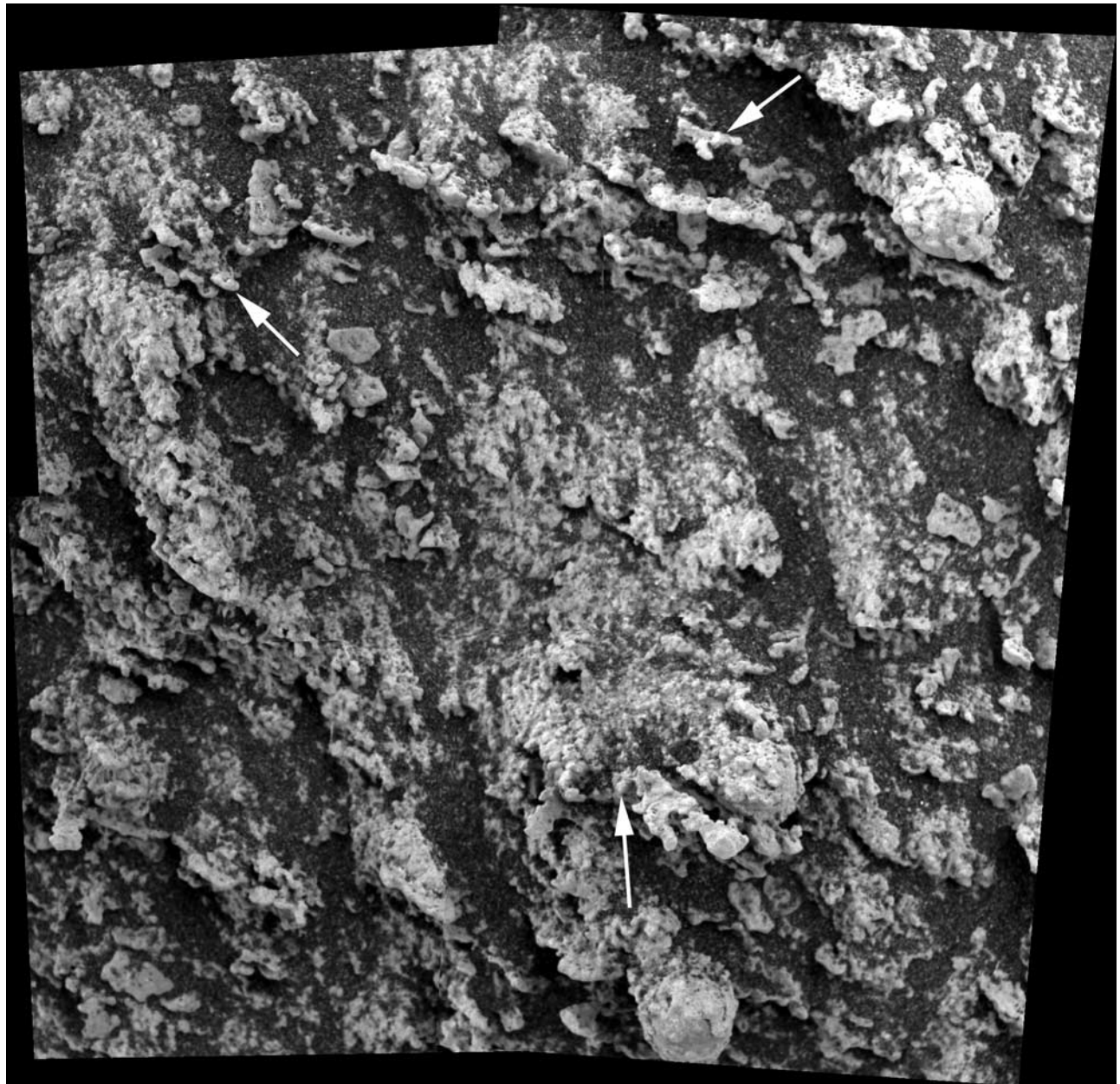


Figure 10. Mosaic of target Wanganui, taken on sol 282 with target fully shadowed. Note discontinuity of laminae, though individual layers are still visible at lower left. This irregular structure is most prominent here, although target B305 Paikea shows it to a lesser extent as well. Ridges on this target end in nodules or septa (arrows). Mosaic is about 5 cm across.

boulders on Meridiani Planum include basalt clasts ejected from nearby craters, as well as meteorites [Schröder *et al.*, 2008; J. Zipfel *et al.*, Bounce rock: A basaltic shergottite at Meridiani Planum, Mars, submitted to *Meteoritics and Planetary Science*, 2008]. Continuing MI operations have provided new views of rock textures that confirm and extend these early discoveries.

[23] Although the Meridiani outcrops represent a coherent succession of fairly homogeneous laminated sandstones, rock surfaces examined by the MI appear to fall into several distinct textural classes. Accordingly, outcrop rock surfaces and loose fragment targets have been divided into five classes based upon visible lithology, texture, and

sediment structure: laminar, nodular, angular, massive-dark, and massive-bright. The laminar, nodular and massive-bright classes are not discrete, but rather reflect variations on the theme of sedimentary rock deposition and diagenesis established early in the mission. The common element among rock and loose fragment targets in these classes is a recrystallization texture that in terrestrial rocks would be strongly associated with secondary mineral mobilization and chemical sedimentation. This texture, which takes on various degrees and characteristics as described below, nevertheless appears consistently throughout 6.5 km of horizontal traverse.

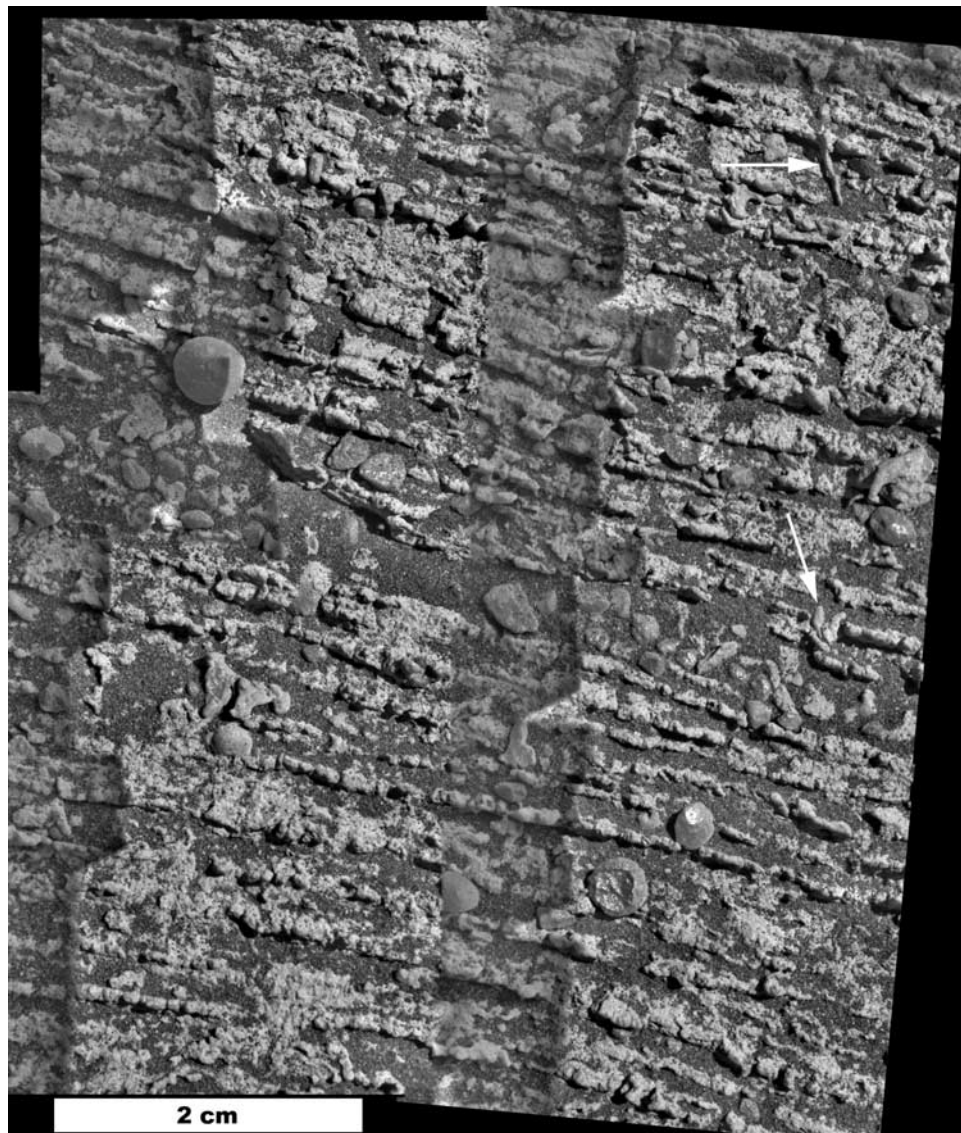


Figure 11. Mosaic of target Kahu from the rock Whatanga, taken on sol 310 with target partly shadowed (contrast reduced). Laminae are continuous through most of this target, punctuated by spherules and broken fragments of clasts presumed to be spherules. Laminae are bisected in several places (arrows); the explanation for this is unclear.

[24] In addition to rocks and fragments that are part of, or clearly derived from, the outcrops, the Opportunity MI also imaged a number of cobbles on the surface of Meridiani Planum. The cobbles can be divided into a single sample of iron meteorite and a series of exotic cobbles of broadly basaltic character.

[25] MI observations are summarized in Table A1 (see Appendix A). The terms used in Table A1 to describe images taken before and after abrasion by the Rock Abrasion Tool (RAT) are “preRAT” and “postRAT” [Gorevan *et al.*, 2003], respectively. Similarly, “prebrush” is used to describe images taken before brushing (without abrasion) by the RAT. One rock, with its associated targets (“Heatshield,” originally named “SpongeBob”) is classified separately as a meteorite and officially recognized as “Meridiani Planum” [Connolly *et al.*, 2006]. Two targets are not easily placed into this classification scheme:

“Barberton” (observed on sol 121) and “Tennessee” (observed on sol 139). The target Tennessee has been identified as an upper member of the Burns formation upper unit [Grotzinger *et al.*, 2005; McLennan *et al.*, 2005], and it has been suggested that Barberton is a stony meteorite [Schröder *et al.*, 2008].

4.1.1. Laminar Rock Surfaces

[26] The laminar class of targets is characterized chiefly by distinctive millimeter- to submillimeter-scale laminations visible to a greater or lesser extent for each target. Target surfaces are microscopically coarse and irregular. There are millimeter-scale spherules scattered throughout, some embedded within the rock, others lying on the surface. The spherules often stand higher than the surrounding surfaces, indicating greater resistance to the sandblasting that affects outcrop surfaces. This rock class is relatively homogeneous in reflectance, while embedded clasts such as spherules are

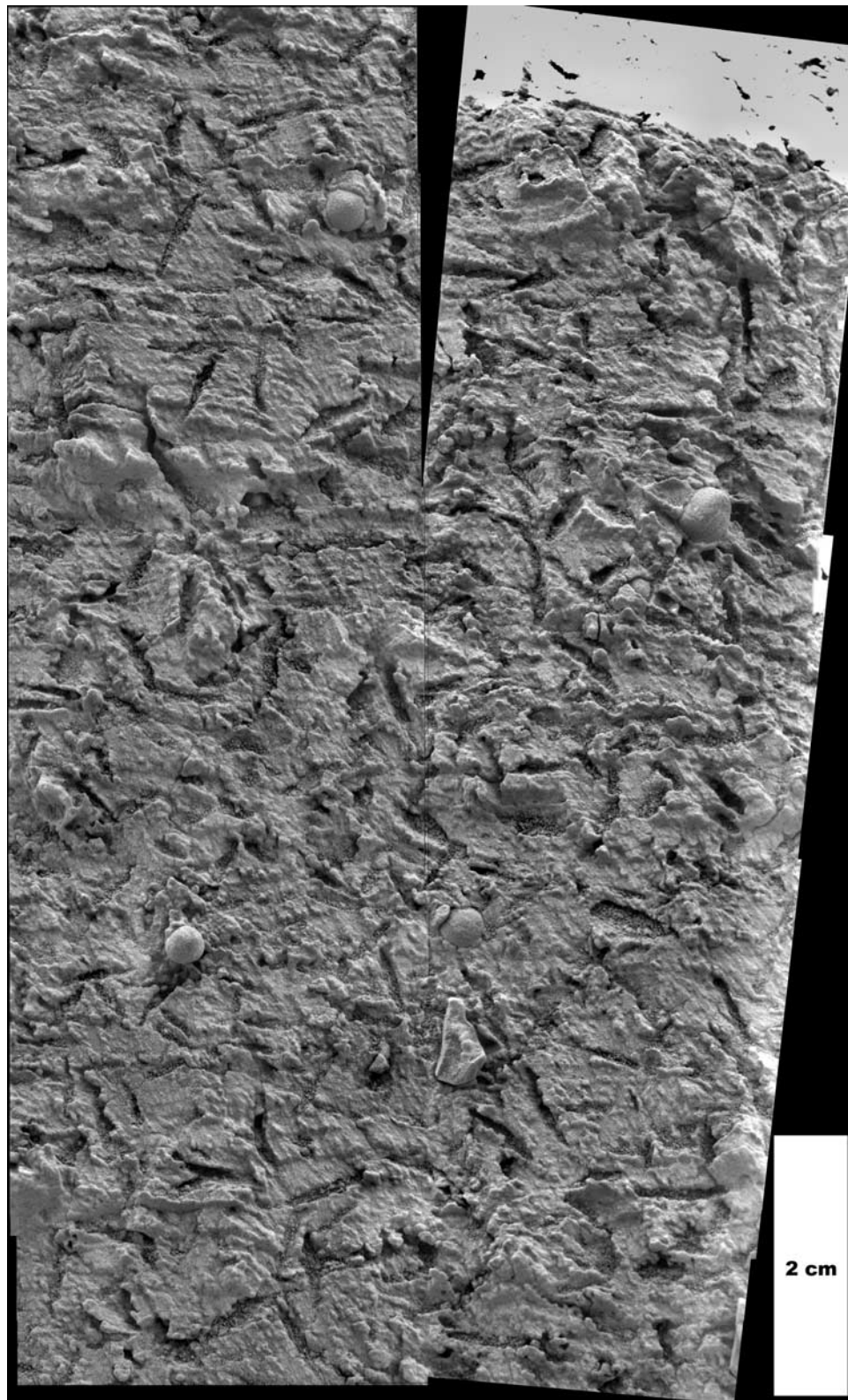


Figure 12. Mosaic of Diogenes, taken on sol 125 when target was mostly shadowed. Randomly oriented blade-shaped vacancies cut across laminar sequences.

slightly darker. Dark, loose grains of the basaltic sand observed regionally often collect in depressions. There are some similarities in the lamination, clastic textures, and

cementation features (e.g., spinose structures that end in rounded grains or grain aggregates) between the bright outcrop surfaces at Meridiani and the “Peace” class rocks

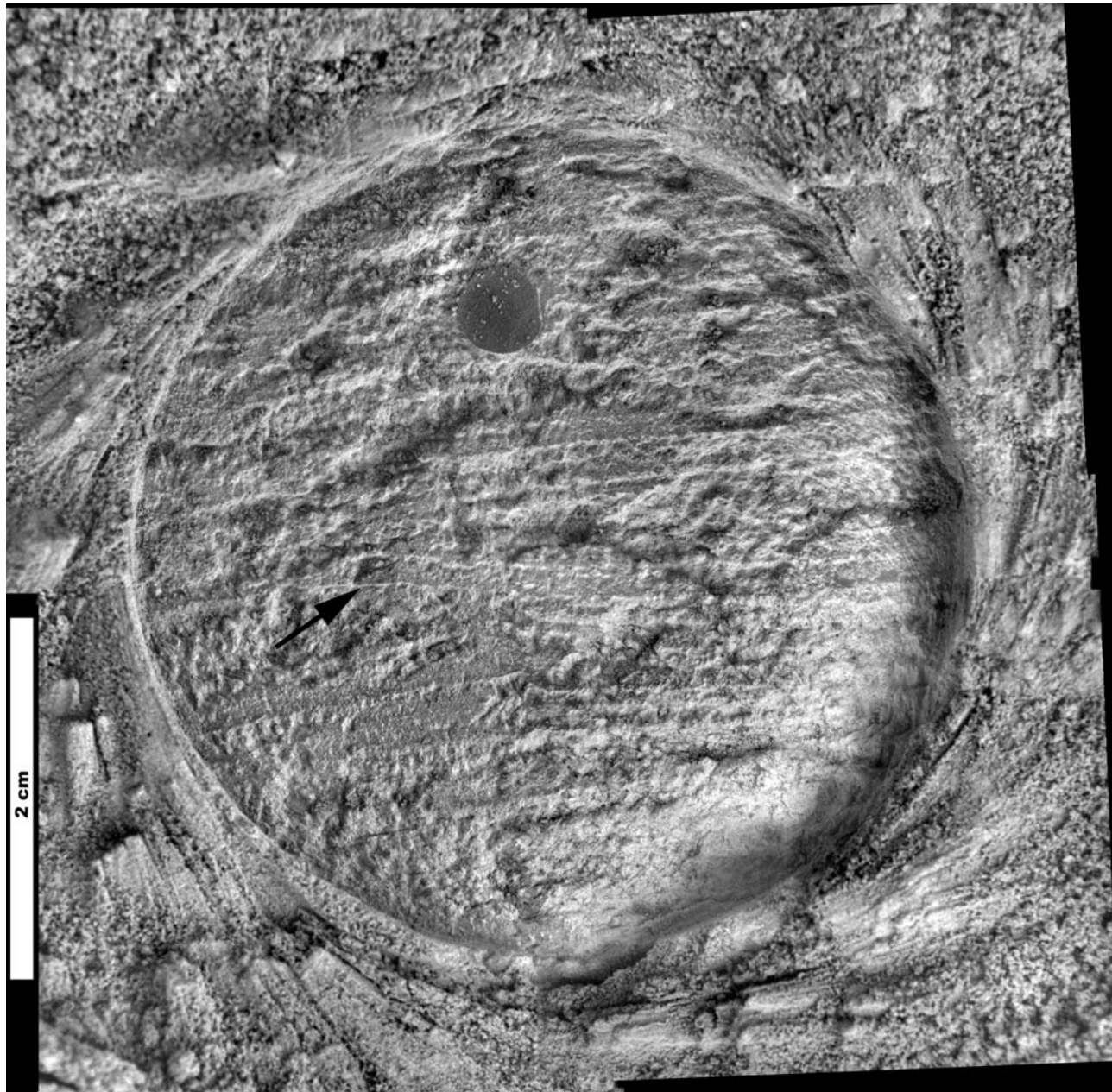


Figure 13. PostRAT mosaic of target Drammersfjord, taken on sol 162 with target fully shadowed. Laminae are shown extending from left to right in the mosaic, with slight departures from parallelism indicated by the arrow. This has been interpreted as a rippleform with possible cross-lamination by *Grotzinger et al.* [2005] and highlights the sedimentary nature of this rock class. Note also the spherule ground through by the Rock Abrasion Tool (RAT) in the upper center of the image, with superficial dust grains but showing no evidence for internal structure.

in Gusev Crater [*Herkenhoff et al.*, 2006], which are also interpreted to be sulfate-cemented sandstones [*Squyres et al.*, 2006].

4.1.1.1. Lithology

[27] Figure 9 shows an MI mosaic of the target “Siula Grande,” an outcrop in Endurance Crater. The most conspicuous feature in the mosaic is submillimeter lamination. In other Meridiani sedimentary rocks targets, the laminae are plainly composed of sand grains, commonly a single grain in thickness. Here, grains are only occasionally

discernable, suggesting remobilization and recrystallization of sulfate salts to form secondary, cement-dominated textures.

[28] The primary nature of the layering observed on laminar rock surfaces is indicated by the common geometric truncations of laminae associated with low-angle stratification and cross-lamination, as described by *Grotzinger et al.* [2005, 2006]. There is a range of coherence to the surface expression of these laminae, from thick and continuous, as seen at Siula Grande, to highly discontinuous, such that

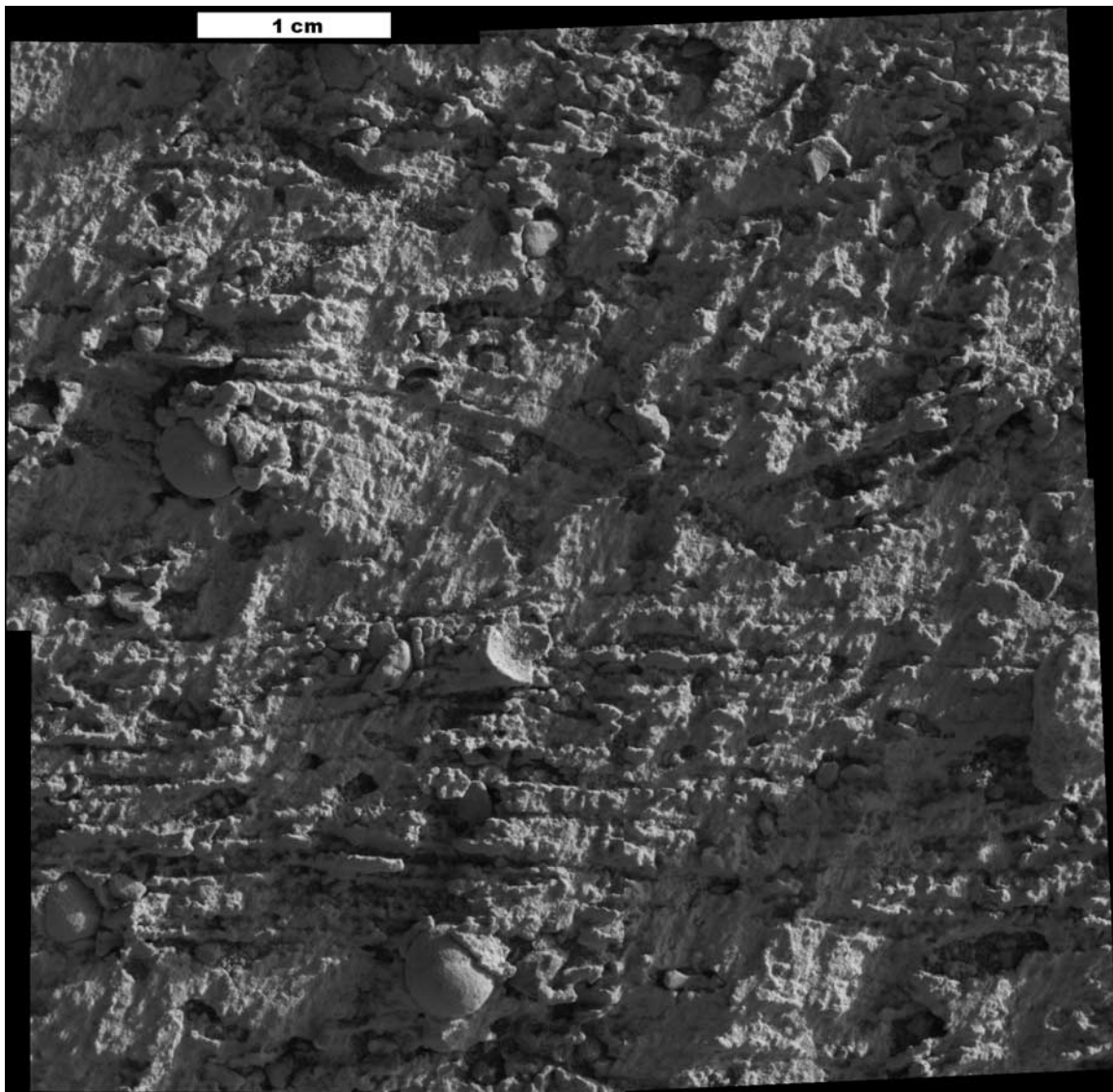


Figure 14. Mosaic of target Kettlestone from the rock Manitoba, taken on sol 152 with illumination from upper right. Note lens-shaped feature at left center. Possible origins of this feature and the surrounding texture include cross-bedding, pinch and swell features, and lithified ripple features.

individual laminae are seen only as small ridges because they stand out from an underlying rock surface that is mantled by darker, finer-grained material (e.g., “Wanganui,” shown in Figure 10, and “Kahu” on the rock “Whatanga,” shown in Figure 11). In the latter examples, most ridge edges are irregular, but end in small bulbous features, likely representing individual or small clusters of cemented sand grains. Some ridges are disrupted by spherules, supporting the interpretation of the spherules as concretions formed by diagenetic fluid flow (Figure 9). Flakes and ridges curve around spherules in many cases, consistent with their being cemented by secondary minerals. Examples of such structures can be seen in Figures 10–14.

[29] Well-sorted sandstones typically have abundant intergranular porosity, but those found in the Meridiani outcrops appear to have much of the primary porosity occluded by the formation of later cements. On the other hand, MI images revealed the common presence of secondary poros-

ity [Choquette and Pray, 1970] in the form of crystal molds (termed “vugs” by Squyres *et al.* [2004b]) and elongate to sheet-like vugs that in places have been greatly enlarged by later diagenetic processes [McLennan *et al.*, 2005; Perl *et al.*, 2007]. Moldic porosity, formed by the diagenetic precipitation and subsequent dissolution of an unidentified soluble mineral phase (such as sulfates or chlorides), occurs in some but not all sedimentary rock targets (e.g., “Diogenes,” shown in Figure 12). No preferred orientation is evident to first order for these pores [McLennan *et al.*, 2005].

4.1.1.2. Texture

[30] Individual or possibly aggregated grains within the laminae are poorly resolved in many targets because of diagenesis [McLennan *et al.*, 2005; Metz *et al.*, 2008]. In some cases (see section 4.1.1.3), however, grain shape, roundness, and size distribution can be measured. Grains are too small to resolve pitting, frosting, or fracture patterns.

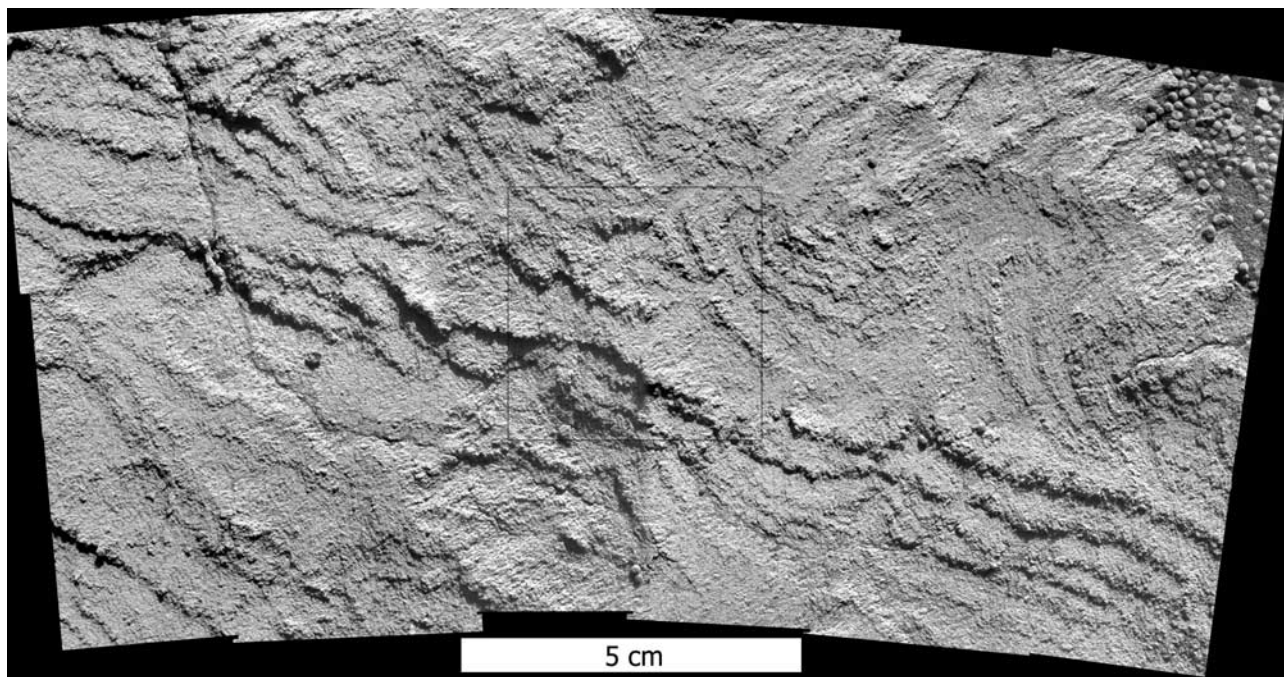


Figure 15. Mosaic of MI images of Overgaard, acquired on sols 721 and 723 with illumination from top. Box shows area used to gather data shown in Figure 29b.

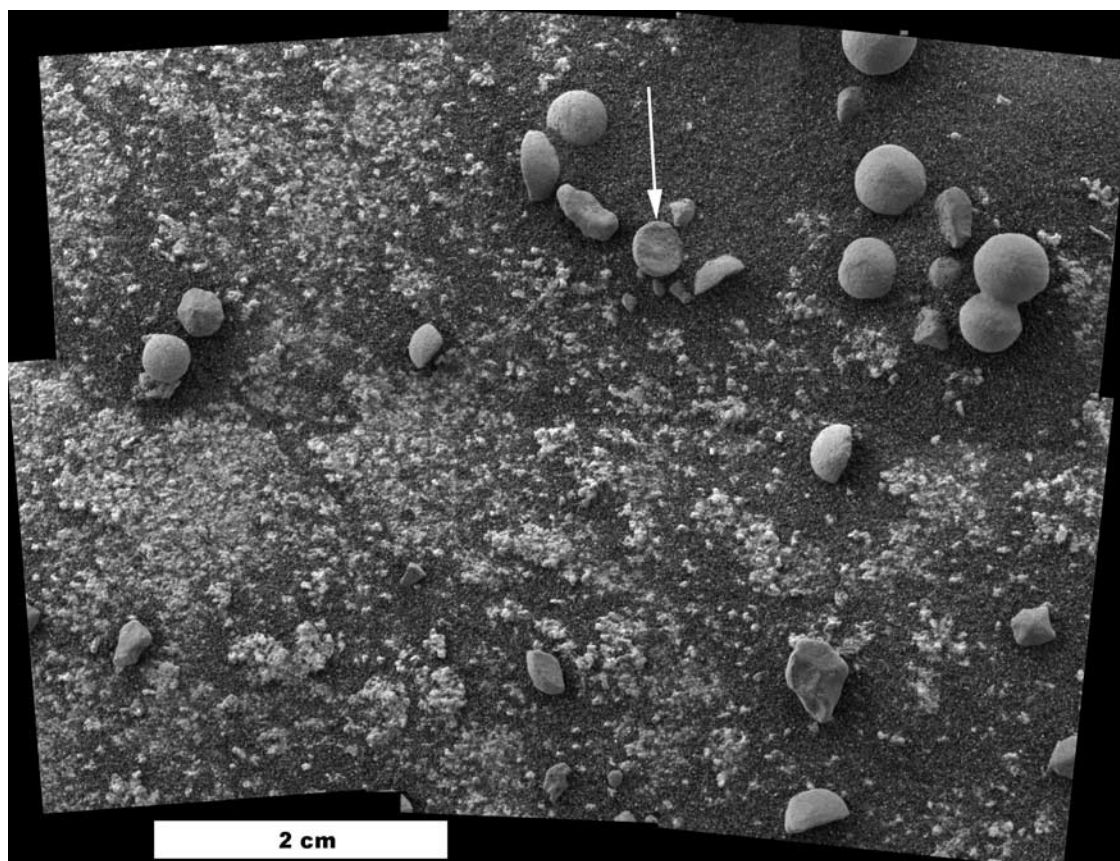


Figure 16. Mosaic of MI images of target Tuktoyuktuk, taken on sol 186 when fully shadowed. Texture appears similar to laminar rock surfaces, but no coherent laminae appear to be present. Several obviously broken spherules litter the surface (arrow).

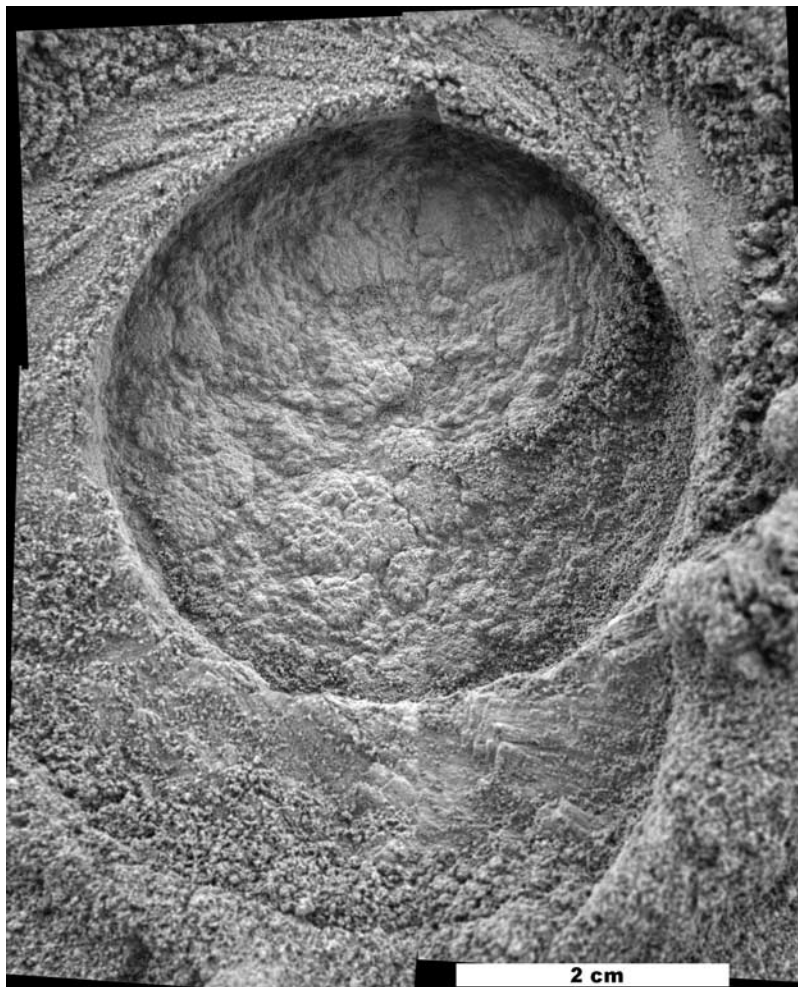


Figure 17. MI mosaic of target Holman_3, taken after RAT grinding on sol 178 when target was fully shadowed. Note unusual cauliflower-like texture within RAT hole.

Grains that can be resolved tend to be well sorted throughout exposed rock surfaces, imparting a granular appearance. Spherules embedded within laminar class targets average approximately 4 mm in diameter, with mean size decreasing along the southward traverse from Endurance toward Victoria Crater [Calvin *et al.*, 2008]. The spherules are nearly homogeneous and commonly lack any obvious internal structure (Figure 13) [Herkenhoff *et al.*, 2004b]. However, in rare cases, spherules display surficial banding parallel to the local lamination, similar to that seen in Eagle Crater [Squyres *et al.*, 2004b; McLennan *et al.*, 2005; Calvin *et al.*, 2008].

4.1.1.3. Sedimentary Structure

[31] Laminae range from very narrow, continuous layers ~800 μm thick (e.g., Figure 9) to wider, more broadly spaced layers 2 to 2.1 mm thick that display some undulation around lens-shaped features, such as those seen in the “Drammersfjord” (Figure 13) and “Kettlestone” (Figure 14) targets, to more discontinuous laminae, whose coherency breaks down to the point where individual layers can barely be traced (e.g., Wanganui, shown in Figure 10, and Wharenuui).

[32] MI images of “Overgaard,” near Erebus Crater, show well-sorted grains in trough-shaped laminae (Figure 15).

Stereo MI images of this target were used to create a Digital Elevation Model (DEM) using the techniques described by Herkenhoff *et al.* [2006]. The DEM shows that the topography of the outcrop is not correlated with bedding, so that the observed sedimentary structures are primary, not the result of erosion [Grotzinger *et al.*, 2006].

4.1.2. Nodular Rock Surfaces

[33] When viewed in preRAT MI images, nodular rock surfaces are very similar to laminar rock surfaces, with microscopically coarse and irregular bright texture standing high, and darker, finer grains lying in broader topographic lows. Darker spherules are scattered throughout and often stand higher than the surrounding rough texture. Some spherules are embedded within the rock surface, while others are found lying on the surface. In this class, however, no regular laminae can be seen, and postRAT images display a class-defining nodular texture within the RAT hole, as discussed in section 4.1.2.2. With the exception of “Kendall” (observed on sol 598), all nodular rocks occur in the lower wall of Endurance Crater.

4.1.2.1. Lithology

[34] Nodular rocks have a granular appearance on undisturbed surfaces, with discontinuous positive relief that stands out from the broad lower regions that are mantled

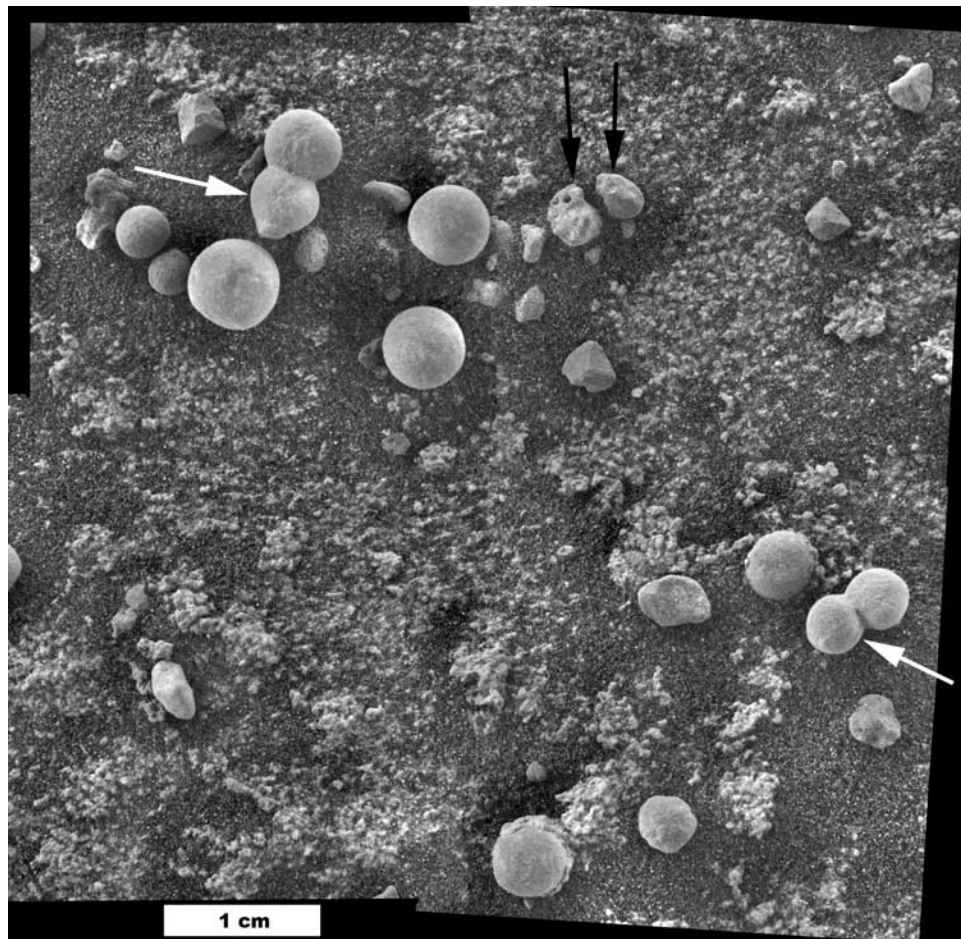


Figure 18. MI mosaic of target Campbell, taken on sol 182 when fully shadowed. The bimodality in size of larger clasts is shown in this image, including spherules and spherule doublets (white arrows; note that the example at upper left may have developed a third incipient spherule at the bottom), broken spherules, and irregular pitted clasts (black arrows).

by darker, finer-grained material. These bumps have a lower profile than the ridges of the laminar rock surfaces. The bumps show little organization or coherence when compared to laminar surfaces (e.g., at the target “Tuktoyuktuk,” shown in Figure 16, possibly because the target surface is parallel to bedding) but they have a similar reflectance and may be genetically related. Most bumps are irregular, but convex (the target “Razor Cluster” is a partial exception to this rule, displaying some sharp edges more similar to targets within the angular class). Where they exist on nodular rock surfaces, coherent ridges curve around spherules in many cases, consistent with their having been cemented in place. No cleavage planes, crystalline grains or other lithologic evidence is observable.

4.1.2.2. Texture

[35] The overall texture and surface morphology of nodular rock surfaces, as revealed in postRAT images, is bumpy (e.g., target “Holman_3,” Figure 17). This texture is unusual, reminiscent of cauliflower, and shows no preferred orientation. The texture could be the result of cemented grain aggregates or more resistant, larger grains supported by a cementing agent. Crystals in the cements are not resolved by the MI. In either case, these features have been

interpreted to be related to diagenetic recrystallization [McLennan *et al.*, 2005].

[36] Spherules, averaging 4.2 mm in diameter, are present both within and resting on nodular rock surfaces, and are nearly perfectly spherical [McLennan *et al.*, 2005]. In addition to spherules, other loose particles, with distinct size and shapes, are also commonly found on the rock surfaces; these are interpreted to be small eroded fragments of outcrop rocks. Spherule and spherule fragments that reside on the rock surfaces are more rugged and pitted than those embedded within the rocks (e.g., the target “Campbell,” Figure 18). Spherule doublets, and very rarely linearly aligned triplets, also occur more frequently in these images than in those of other rock classes, but the loose spherules on the surface may not have been derived from the outcrop they lie upon. Spherules that have been broken or abraded (Figure 13) do not show any evidence of internal structure at MI resolution [McLennan *et al.*, 2005].

[37] Some spherules in the stratigraphic section examined in Endurance Crater are surrounded by a 1 to 2 mm thick layer of recrystallized isopachous cement. Deeper in the stratigraphic section, the thickness of the cements around spherules increases to up to 4 mm and they have a different

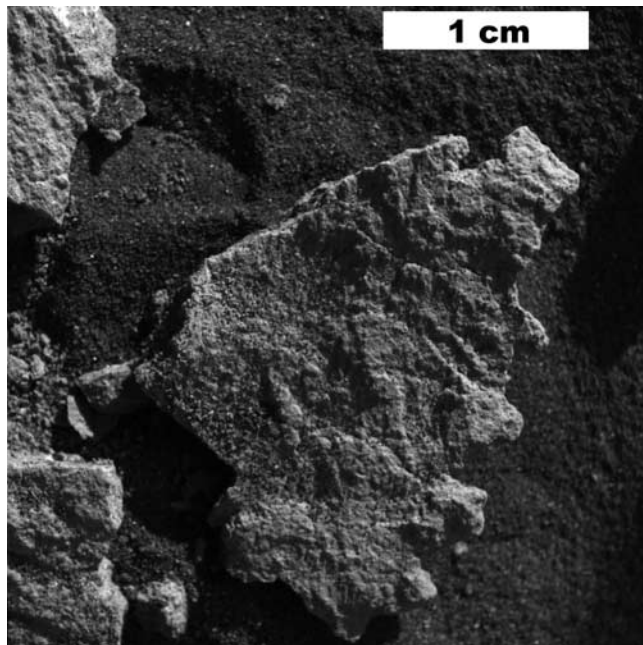


Figure 19. Radiometrically calibrated MI image 1M145775434 of target Sermilik, taken on sol 198 with illumination from upper right. Microtopography is easily discerned in this low Sun image.

character, being formed mainly from differentially cemented sand grains. In this same area, similar-appearing nodules occur that are not overgrowths on spherules [McLennan *et al.*, 2005].

4.1.2.3. Sedimentary Structure

[38] No obvious lamination structures are visible on nodular rock surfaces, either in preRAT or postRAT images. This indicates that, though the brighter bumps protruding from the dark mantling material may be genetically related to the laminar class rocks (that is, associated with a cementing agent), the nodular rocks have been subjected to more extensive secondary mineralization that obscures lamination [McLennan *et al.*, 2005]. It is also possible that these rock exposures are oriented closer to the bedding plane, further obscuring evidence for lamination.

4.1.3. Angular Rocks

[39] Rocks classed as angular are bright, discrete fragments, crisscrossed with fractures. Fragment edges range from very angular to subrounded, and are in this way somewhat similar to the target “Pot of Gold” imaged in Gusev Crater by the rover Spirit [Herkenhoff *et al.*, 2006]. Small cavities run nearly the length of the target “Arnold Ziffel,” subperpendicular to the majority of fractures, and are evident on the target “Sermilik” as well (Figure 19). On the basis of the association of rocks such as Razor Cluster with targets that look similar to laminar and nodular class rocks, angular rocks potentially represent a less weathered or freshly broken version of the material seen in these other two classes. Synthesis with Pancam images shows that the clast Sermilik is a fragment of a thin sheet of cement, of likely diagenetic origin, found in the same outcrops that contain nodular textures. The association of these two features may indicate diagenetic events specific to this

stratigraphic horizon, to the best of our knowledge exposed only deep within Endurance Crater.

4.1.3.1. Lithology

[40] The angular rocks have a granular appearance with relatively flat surfaces overall, as can be seen in Figure 19. Ridges and raised flat areas, in places perhaps only a single grain thick, are evident. Individual clastic grains or grain aggregates can also be seen, though the predominance of a cementing agent makes it difficult to determine the shape or crystalline structure of any of these grains. Particle edges are irregular and angular, consistent with an interpretation that these rocks are freshly broken clasts from a larger cemented sheet or outcrop. The fine grains may have occupied fractures before they were filled by secondary minerals, or may have been incorporated from the rocks forming the walls of the fractures.

4.1.3.2. Texture

[41] As noted above, grains are commonly too small (or too heavily coated with secondary cementing materials) to resolve shape, roundness, pitting, frosting, fracture patterns or other such diagnostic textural features. A few individual clastic grains or grain aggregates can be seen in the target Sermilik, where the sun angle is lower and microtopography is more easily discerned (Figure 19). If these structures represent individual grains, rather than aggregates, then the average grain size represented by this class is 300–350 μm in diameter. No preferred orientation of grains is evident.

4.1.3.3. Sedimentary Structure

[42] Faint lamination is occasionally visible in angular rocks, especially in the lower portion of the Arnold Ziffel target. There the laminae are about 1.2 mm thick, similar in



Figure 20. Focal section merge of five MI images of Nala, taken on sol 105 with illumination from upper left. The massive nature of the rock target can be seen, along with rounded, weathered edges and numerous pits. Area shown is 3 cm across.

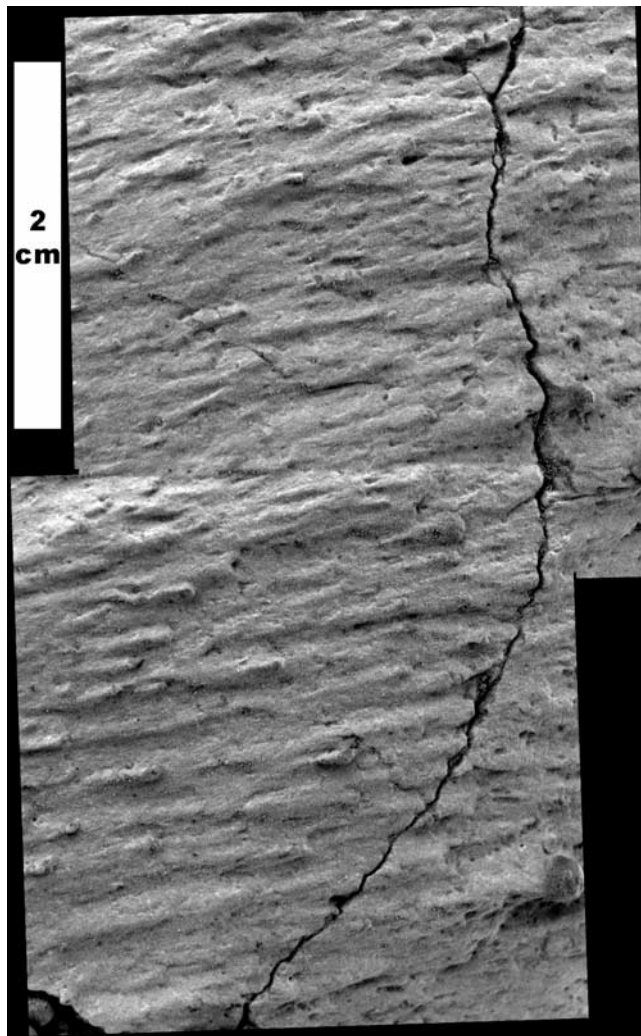


Figure 21. Target Normandy on the rock Omaha, taken on sol 392 when the target was fully shadowed. The streamlined “wind tails” on this rock are unique to the Opportunity MI collection.

overall texture to the laminae seen in the nodular and laminar rocks.

4.1.4. Massive-Dark Rocks

[43] Rocks in this class are massive-textured rocks that often display a somewhat granular, heavily fractured appearance, with rounded edges and numerous surface pits (e.g., “Nala,” Figure 20). Rock surfaces range from relatively flat and flush (e.g., “Barlach_3,” taken on sol 214) to undulating, with small knobs separated by fractures (e.g., “Twin Otter,” taken on sol 259). Fractures display a range of fill by surrounding darker soil, from entirely filled to relatively clean and empty.

4.1.4.1. Lithology

[44] Massive-dark rock surfaces are more heterogeneous in reflectance than other classes. No cleavage planes or other distinct lithologic feature is observed. No individual crystalline grains or crystal form pores are evident. Pits appear eroded along their edges, and have likely been wind abraded. Thus, if the pits represent crystal form molds, their shape is no longer discernable enough to be diagnostic.

4.1.4.2. Texture

[45] Targets in the massive-dark rock class have a somewhat granular appearance, best visible along the edges of fractures. Elsewhere, target surfaces display rounded edges, in places well developed, and an eroded, pitted texture. Individual grains are not resolved in MI images. As noted above, pits are abundant in several targets of this type (Figure 20). Pits have rounded edges for the most part and are narrow in profile with depth. In this sense, the pits look similar to low-grade cavernous weathering. Loose clasts lie within low-topography and fracture regions that are similar to those seen in other targets. The exception to this is the “Afar” target (taken on sol 210), which has much smaller clasts (averaging $\sim 465 \mu\text{m}$ diameter) packed closely into the visible fractures. No preferred orientation of grains is evident (grains are too small for any such orientations to be discernable at MI resolution).

4.1.4.3. Sedimentary Structure

[46] No obvious layering or lamination structures are visible in the massive-dark rock class. The exception to this statement is the target “Normandy” on the rock “Omaha” (Figure 21). A single fracture runs through the entire MI mosaic, but the surface itself is covered with positive topography, elongate teardrop-shaped features that are parallel to each other, somewhat similar to features identified as ventifacts imaged on an outcrop at Fram Crater [Sullivan *et al.*, 2005]. In some cases these features are truncated at a pit; in others, they are truncated at a discontinuous concavity. The embedded spherule visible at lower right in Figure 21 also has this type of feature sweeping away from it, which implies formation of the features subsequent to spherule genesis. These features are probably eolian erosional remnants (wind tails trailing more

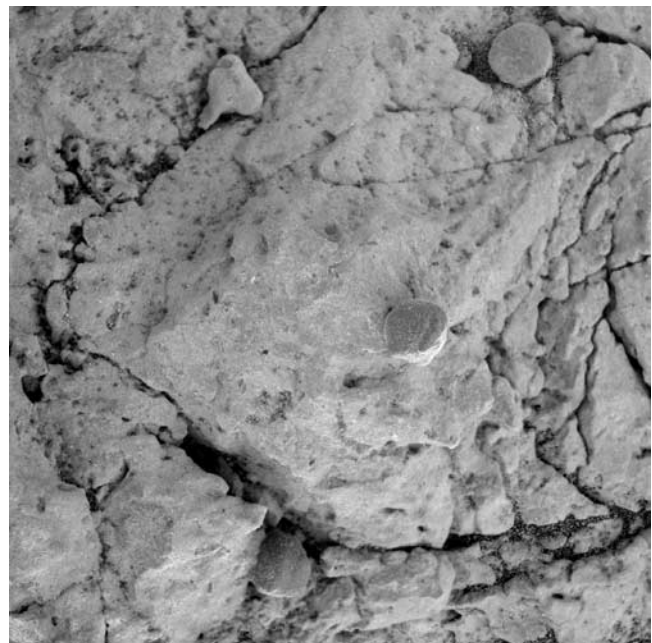


Figure 22. Focal section merge of four MI images of Russett, taken on sol 381 when target was fully shadowed. Sequence of fractures on right side shows range from massive rock to small fragments falling out of matrix. Area shown is 3 cm square.

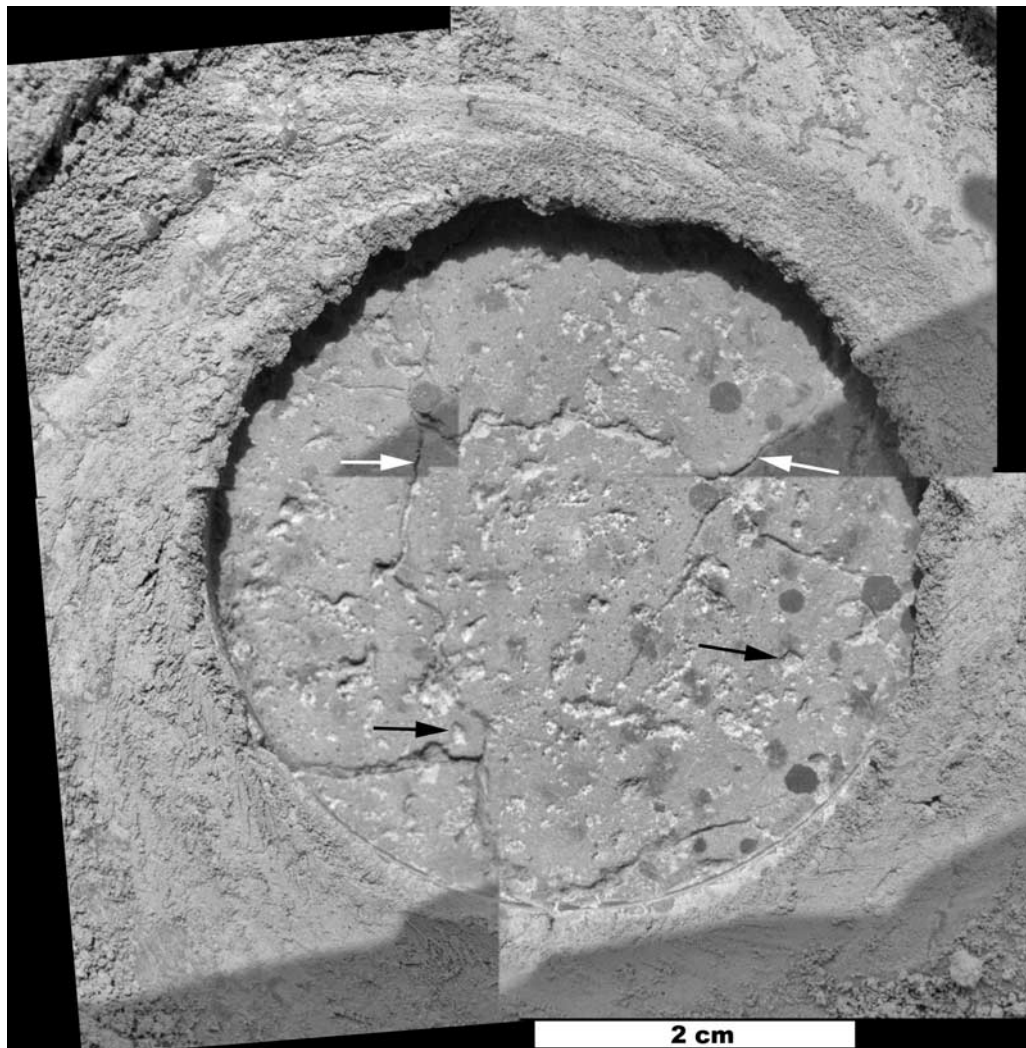


Figure 23. Mosaic of postRAT MI images of target One Scoop, taken on sol 546 when target was partly shadowed (illumination from top, shadow contrast reduced). Note spherules ground through by RAT, lacking internal structure and in some cases having irregular outlines. Negative topography structures range from short, somewhat rounded, truncated cavities (black arrows) to long, thin fractures (white arrows).

resistant grains) formed in an environment with a consistent strong wind direction; pits represent regions where the more resistant grains have been plucked [Sullivan *et al.*, 2005]. This interpretation is preferred over one in which the linear features represent primary sedimentary structure that has been highlighted by erosion because the linear features are parallel to the wind tails.

4.1.5. Massive-Bright Rocks

[47] This rock class is composed of massive-textured rocks that are similar to the massive-dark class in terms of moderate to heavy fracturing and other features (e.g., postbrush target “EmilNolde2” compared to “Lemon Rind”). However, surfaces commonly are brighter and display undulating topography resistant to the RAT, ranging in relief from very flat (e.g., Lemon Rind) to very irregular (e.g., “Russett Eye,” Figure 22). Rock surfaces are bisected by cracks that continue at least as deep as RAT holes (a few millimeters), while postRAT images show spherules and randomly oriented cavities similar to nodular and laminar

classes (as seen in the postRAT target “One Scoop,” shown in Figure 23). Angular grains (300–600 μm across), similar in reflectance and texture to the rock, are sprinkled across the surfaces of these targets.

4.1.5.1. Lithology

[48] Like the massive-dark class, this rock class has a somewhat granular appearance. However, proximity as well as similarity in reflectance and texture suggests that rocks of this type are the source of the smaller, angular clasts that are scattered throughout the soil samples (Figure 22). PostRAT images reveal veins/cracks and vacancies, both randomly oriented (Figure 23).

4.1.5.2. Texture

[49] No grains are resolved to allow evaluation of individual grain texture, sorting or size. Instead, this class is characterized by a brighter, massive but granular appearance and severe dissection by fractures. Fractures through targets in this class do not appear to be oriented relative to any specific surface of stratification. The same is true for

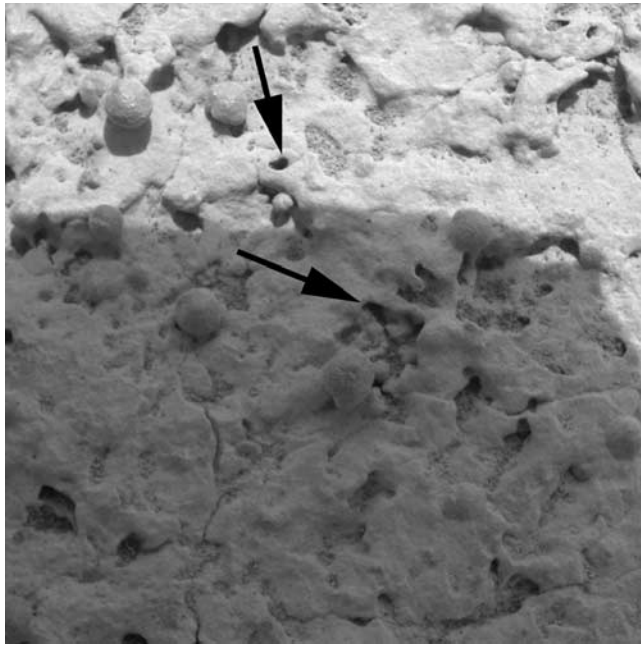


Figure 24. Focal section merge of seven MI images of target One Scoop, taken on sol 544 when target was partly illuminated from top. Cavities are scattered throughout the surface (arrowed). Area shown is 3 cm square.

structures such as cracks/veins and vugs visible in postRAT images. The shadow length in vugs is approximately $150\ \mu\text{m}$, indicating a depth no greater than this value. The depth of vugs appears to be homogeneous throughout these

surfaces, which may be consistent with a surface of stratification at that depth, parallel to the image plane.

[50] Cavities are randomly distributed in several preRAT target surfaces (e.g., “One Scoop1,” Figure 24). Those that have subrounded or more rounded rims average $300\text{--}400\ \mu\text{m}$ in diameter. As in the massive-dark class of rocks, the smoothed texture of cavern borders may indicate weathering. Also similar to other rock classes, postRAT images show dark, larger spherules in a fine-grained matrix. However, this class contains a few spherules that are slightly elongate (some are visible in Figure 24) and more irregular in cross section (e.g., Figure 23).

4.1.5.3. Sedimentary Structure

[51] No obvious sedimentary structures are associated with this class.

4.1.6. Heatshield Rock

[52] Heatshield rock (initially named SpongeBob, before its unique nature was discovered) was imaged first on sol 347. This rock displays a highly reflective surface, mantled by dust. Postbrush image sequences show that reflectance increases greatly once mantling dust is removed. The luster is highly metallic, with some mottling likely due to variations in the location and thickness of coatings. This rock, which has been identified as an iron meteorite and officially named Meridiani Planum, is described more fully by Schröder *et al.* [2008].

4.1.7. Exotic Cobbles

[53] Three exotic cobbles found on the way to Erebus Crater were imaged by the MI on sols 551, 554, and 641. These discrete particles were originally singled out for in situ examination because they differed fundamentally in composition from surrounding outcrop, and thus represent exotics. Several hypotheses have been suggested for the

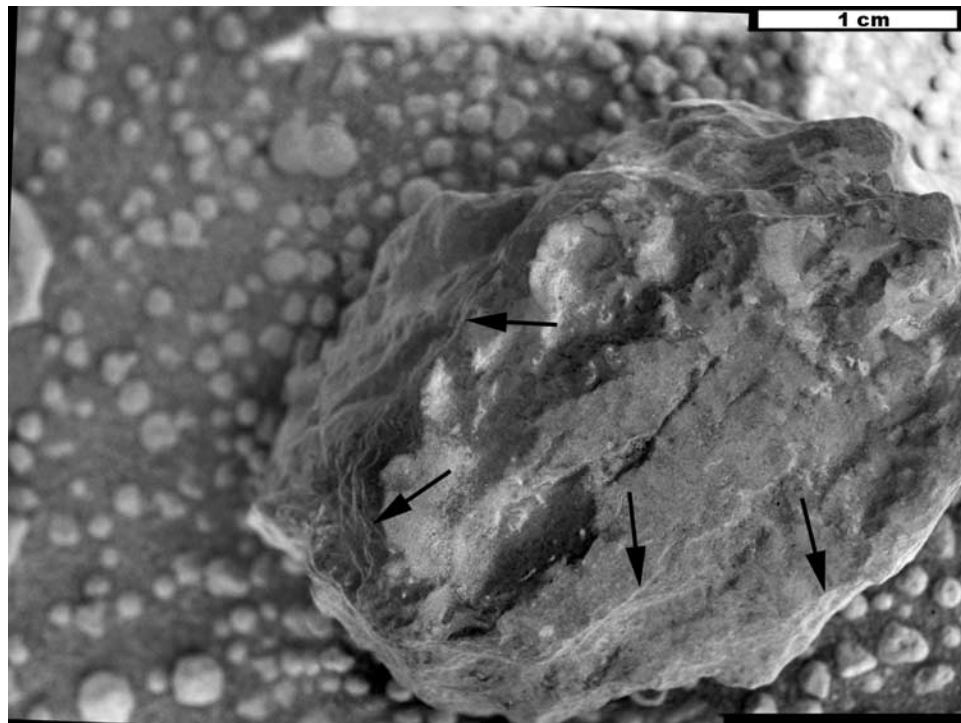


Figure 25. MI mosaic of cobble Arkansas, taken on sol 551 when target was mostly shadowed. Possible stratification indicated by arrows.

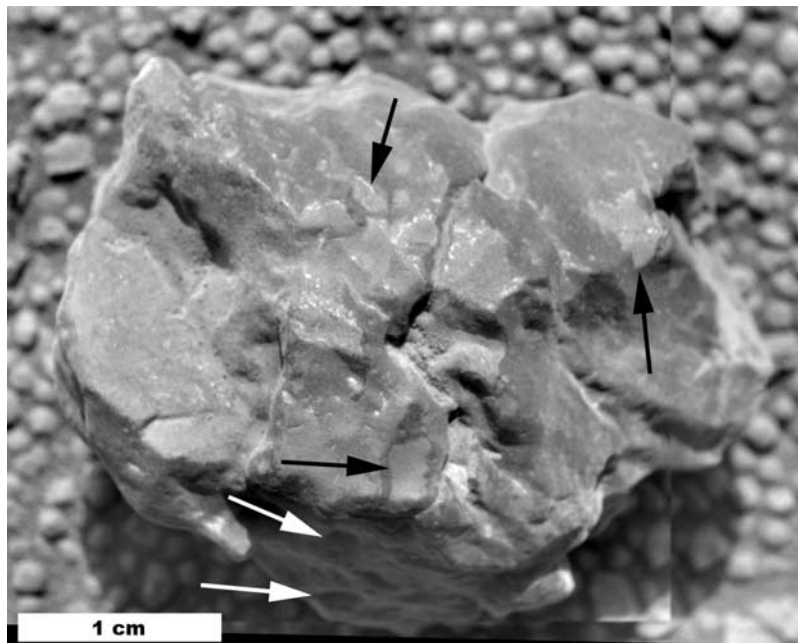


Figure 26. MI mosaic of cobble Perseverance, taken on sol 554 with illumination from top. Cobble has mottled appearance, with darker and lighter irregular areas (black arrows). Pits visible in shadowed region (white arrows).

origin of these cobbles, including an overlying stratum that was subsequently eroded away, impact-transported samples of deeper strata, locally derived impact melts, and resistant material such as rinds or fracture fillings [Jolliff *et al.*, 2006].

4.1.7.1. Arkansas

[54] Arkansas is a cobble approximately 9.45 cm long, sitting on a soil composed of large, rounded grains of similar reflectance that are embedded in a finer-grained matrix. Individual grains comprising the cobble cannot be resolved, and no crystal forms or cavities are evident, so cobble lithology is not diagnostic.

[55] The surface texture of this target is heterogeneous, with smooth areas bisected by shallow striations and giving way to sharp-edged pits, as seen in Figure 25. The pits may indicate alteration by ballistic or eolian impact. However, any detritus derived from these pits is not locally evident, arguing against in situ alteration. Because the cobble is in shadow, it is difficult to determine the overall luster.

[56] The sphericity of this cobble is approximately 0.79, a relatively high value, and elongation (length/width) is approximately 0.72. Because a portion of the cobble is not imaged, these values are necessarily minimum estimates. Quantitative roundness (which depends on the sharpness of clast corners) could not be determined definitively but can be estimated as angular to subangular, which indicates a quantitative roundness between 0.17 and 0.35 [Powers, 1953]. There is no evidence that breakage occurs along grain or crystal boundaries or fractures. Peeling along surfaces of stratification may be indicated by scalloping along the cobble edges (Figure 25). Individual grains or crystals comprising the cobble cannot be resolved, so neither grain fracture, sorting, nor preferred orientation of grains/crystals can be measured.

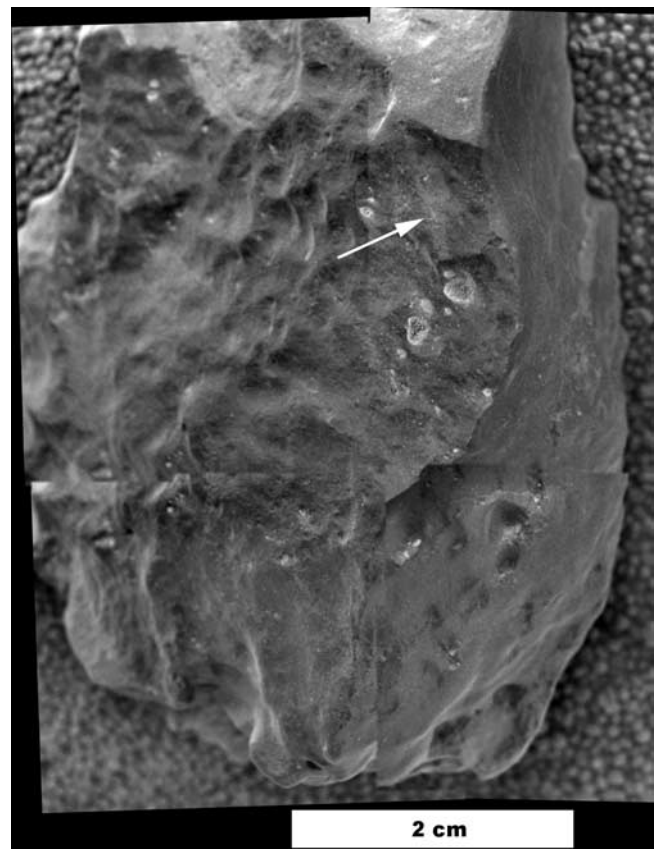


Figure 27. MI mosaic of cobble Antistasi, taken on sol 641 when fully shadowed. Cobble reflectance is heterogeneous, with irregular lighter areas (arrow) embedded in a darker mass.

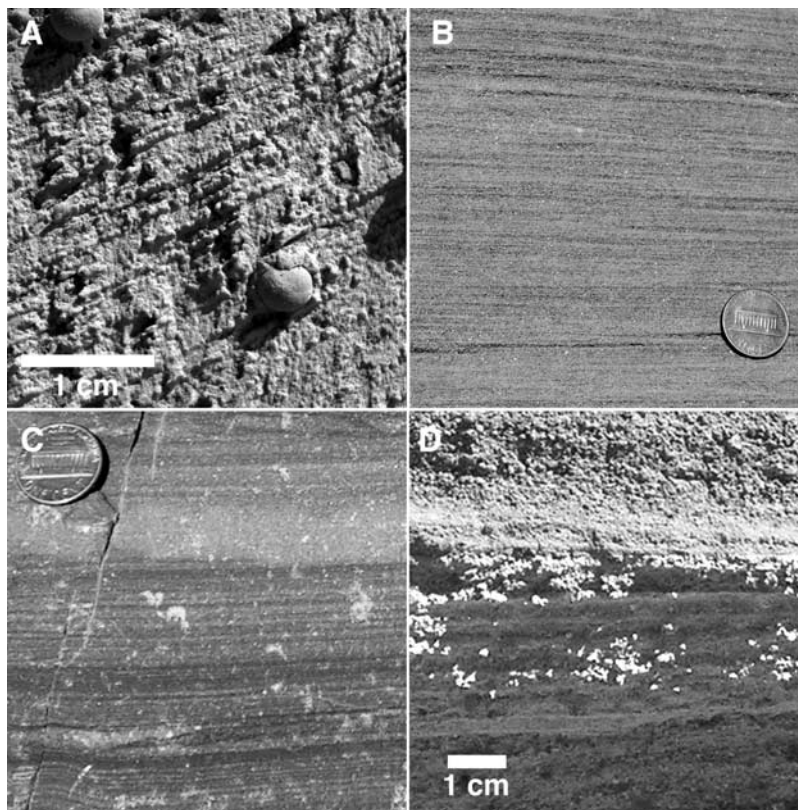


Figure 28. (a) Thin lamination in Burns formation at Endurance Crater. The thickness of individual laminae was measured normal to the trend of the stratification and compared to terrestrial eolian, fluvial, and base surge deposits. MI image 1M140976848 of Cobble Hill acquired on sol 144 with illumination from upper right. (b) Thin lamination in eolian, wind-ripple strata of the Jurassic Page sandstone, Arizona. (c) Thin lamination in fluvial, upper plane bed deposits of the Mesoproterozoic (1.4 Ga) Mt. Shields formation, Montana. (d) Thin lamination in pyroclastic base surge deposit (Pleistocene), Hunts Hole, New Mexico.

4.1.7.2. Perseverance and Antistasi

[57] These two cobbles are about as bright as the larger, rounded soil grains upon which they sit. “Perseverance” is approximately 10.2 cm long (Figure 26), while “Antistasi” is of indeterminate width (the entire cobble is not viewable in the MI images; Figure 27). These cobbles have a mottled appearance, with darker and lighter irregular areas. The cobble color is heterogeneous, with irregular rhomboid-shaped lighter areas embedded in a darker mass. It is not clear if these are individual coarse clasts in matrix or variations in reflectance stemming from coatings or the result of vagaries in reflection due to illumination angle. All mottled regions of Perseverance are fully interlocking, indicating that if these regions represent coarse grains, this cobble is a breccia. Additionally, dark spots 1–2 pixels in diameter appear on the surface of Perseverance. It is not clear if these spots are mantling soil grains, an artifact, or are integrated into the cobble. However, darker-grained mantling of soil seems the likely explanation. No crystal forms or cavities are evident in either cobble.

[58] Although the luster of Antistasi is difficult to determine because it was imaged while in shadow, the surface texture of Perseverance appears greasy or vitreous, and is heterogeneous, with smooth areas bisected by shallow crevices. The cobble has a blocky appearance, with cracks

and apparent seams running along the surface. This rock appears to have worn and weathered in blocks or sections. Edges have been smoothed and rounded, while pits are visible in the upper shadowed region (Figure 26). Antistasi has a heterogeneous texture in which nodules protrude past the mean surface level, while small pits and larger semicircular cavities result in a very angular surface (Figure 27).

[59] The sphericity of Perseverance is approximately 0.82, which would be considered a high sphericity value in a terrestrial setting. Elongation is approximately 0.69, a somewhat elongate particle. Because a portion of the cobble is not imaged, these values should be considered minimum values, and sphericity and elongation cannot be determined definitively. Quantitative roundness (which depends on the sharpness of clast corners) could not be determined directly for either cobble, but is estimated as angular to subangular, which can be translated to a roundness of 0.17–0.35 [Powers, 1953].

[60] There is no evidence that breakage occurs along grain boundaries or fractures on either cobble, nor do any potential coarse grains exhibit evidence for shattering, conchoidal fracturing, sorting or preferred orientation. Peeling along surfaces of stratification may be indicated by scalloping along a single edge of Perseverance, similar to Arkansas. No lamination is evident on Antistasi.

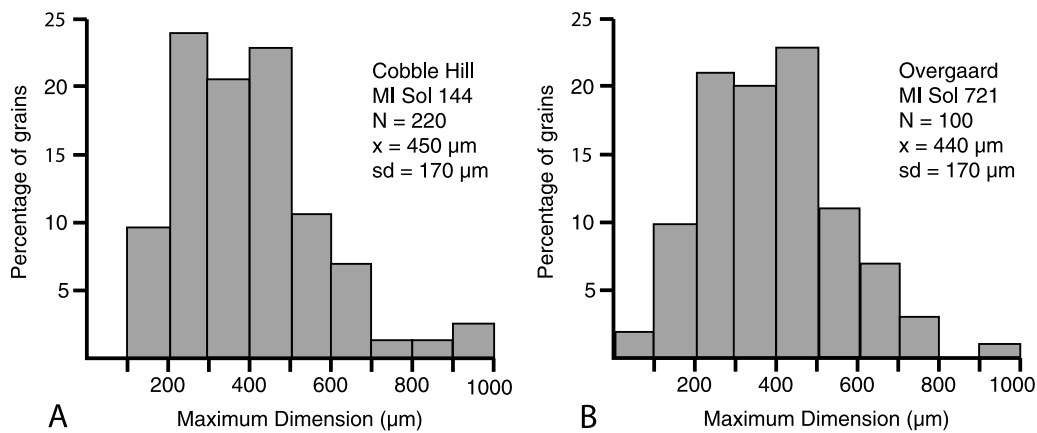


Figure 29. Grain size frequency distribution for Meridiani outcrop rocks imaged by the MI. (a) Cobble Hill, from a bed exposed within Endurance Crater. (b) Overgaard, from an outcrop block near Erebus Crater. N is the number of grains measured; x is mean grain size; and sd is standard deviation.

4.2. Interpretations

[61] The textures viewed by the MI are subject to three major influences. They may reveal details of depositional (or, in the case of volcanic or meteorite samples, igneous) origin and/or transport, they may reflect diagenesis, and they may reflect late stage alteration imparted since the outcrop rocks were exposed at the surface [Knoll *et al.*, 2008]. Furthermore, the apparent textures may reflect target orientation, such that laminated rocks viewed perpendicular to the depositional surface may appear massive. All of

these influences are apparent in targets illustrated above. Depositional features can be seen in the lamination, sedimentary structures, and grain size–frequency distribution of outcrop strata. Diagenesis is clearly recorded in the secondary (e.g., moldic) porosity, hematite concretions (“spherules”), and cement textures that envelop concretions. Postexposure features include sand abrasion textures as well as thin surficial veneers that appear to reflect limited interaction with fluids since formation of the present plains surface.

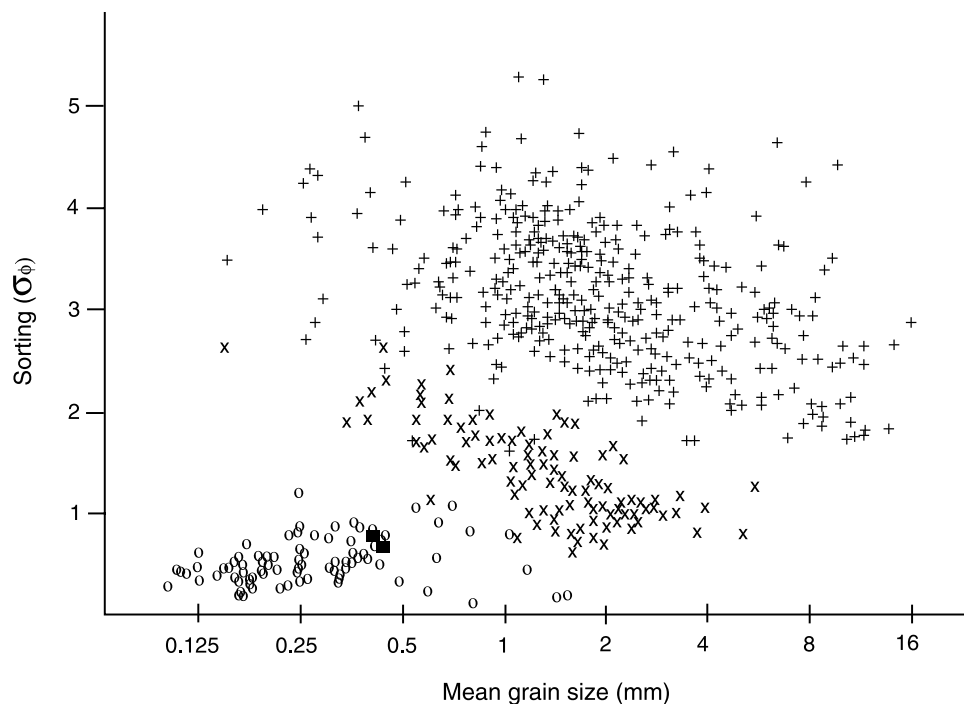


Figure 30. Mean grain size versus sorting for terrestrial surge deposits (pluses; data from Sparks [1976]), a subset of surge deposits separated into individual components and eliminating the fraction smaller than 125 μm (crosses; data from Sparks [1976]), terrestrial eolian sand deposits (circles; data from Ahlbrandt [1979]), and Meridiani Planum outcrop rocks (squares). For description of the sorting statistic, σ_ϕ , see text. Note that eolian sands and surge deposits occupy nonoverlapping portions of the field; Meridiani rocks unambiguously plot with eolian deposits.

Table 1. Microscopic Imager Images Used to Collect Lamination Thickness Data for Burns Formation

Sol	Image ID
42	1M131912406EFF05A6P2953M2M1
43	1M132015283EFF05A6P2952M2M1
124	1M139193264EFF2821P2956M2M1
144	1M140976788EFF3190P2916M2M1
310	1M155703832EFF38EVP2977M2M1
310	1M155704624EFF38EVP2977M2M1
310	1M155705230EFF38EVP2977M2M1
310	1M155706235EFF38EVP2956M2M1
310	1M155706610EFF38EVP2977M2M1
310	1M155707293EFF38EVP2977M2M1

[62] The laminar, nodular and massive-bright classes all contain obvious secondary features. Targets in these classes have been placed by *Grotzinger et al.* [2005] in the Burns formation upper unit, and the upper portion of the Middle Unit. Interpretations of specific rock classes are summarized in this section.

4.2.1. Laminar Rock Surfaces

[63] Lower-relief laminae, often emphasized by darker fine sand grains that accumulate in outcrop recesses, may represent less resistant layers. These laminae alternate with the more prominent layers that apparently have higher resistance to weathering and may reflect local variations in cementation. Laminae are in most cases only a single grain thick, consistent with eolian rather than fluvial depo-

sition [*Grotzinger et al.*, 2005]. The size and sorting of individual laminae suggest that they were formed by impact creep (similar to ripples in terrestrial eolian environments) of particles from a local source. *Grotzinger et al.* [2005] suggested that subcritical climbing of eolian ripples formed the millimeter-scale lamination observed in Endurance Crater. Grains are less well preserved at greater depths within Endurance Crater because of secondary cementation [*McLennan et al.*, 2005]: Laminar rocks grade into nodular rocks, providing strong evidence that nodular textures oriented during diagenesis, not deposition. Even where individual grains cannot be recognized, cross-bedding commonly is still visible (Figure 13), indicating transport of sand-sized grains in a bed load.

[64] The observations that laminae have similar thickness and nodules/septa are also similar in size may indicate that these nodules represent individual grains, well sorted and cemented together. The extent of physical weathering could then be determined by the extent to which these resistant grains stand out from the surface. It is not clear why abraded surfaces are so smooth, with no individual grain vacancies (plucked grains) or positive-relief grains remaining. Grain topography appears to be the main source of the overall texture rather than the morphology of the cementing agent, meaning the amount of cementing agent must be low.

[65] The centimeter-scale cross-lamination seen at Overgaard is diagnostic of deposition in flowing water. The

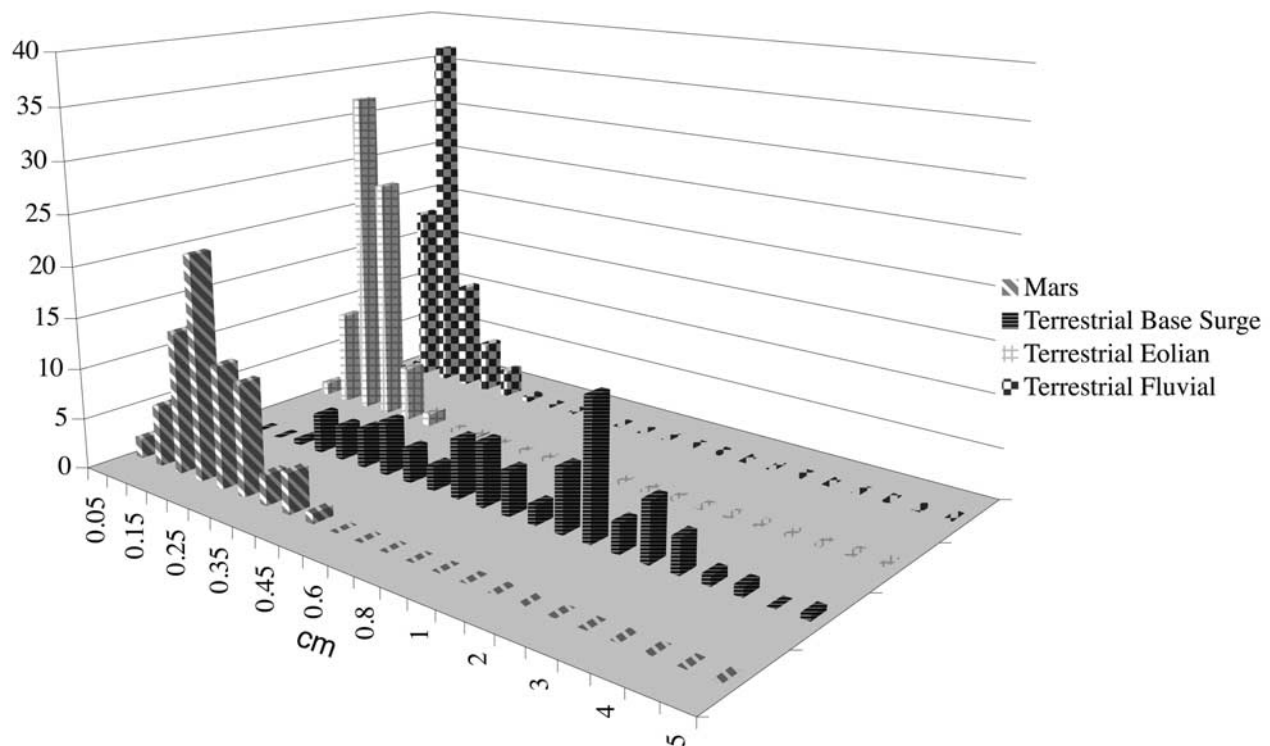


Figure 31. Histogram of lamination thickness in centimeters for Mars (Burns formation), terrestrial base surge (Hunts Hole), fluvial (Mt. Shields formation), and eolian (Page Sandstone) deposits. Note similarity between Burns and terrestrial eolian and fluvial deposits. However, the Burns laminae differ significantly from terrestrial base surge deposits.

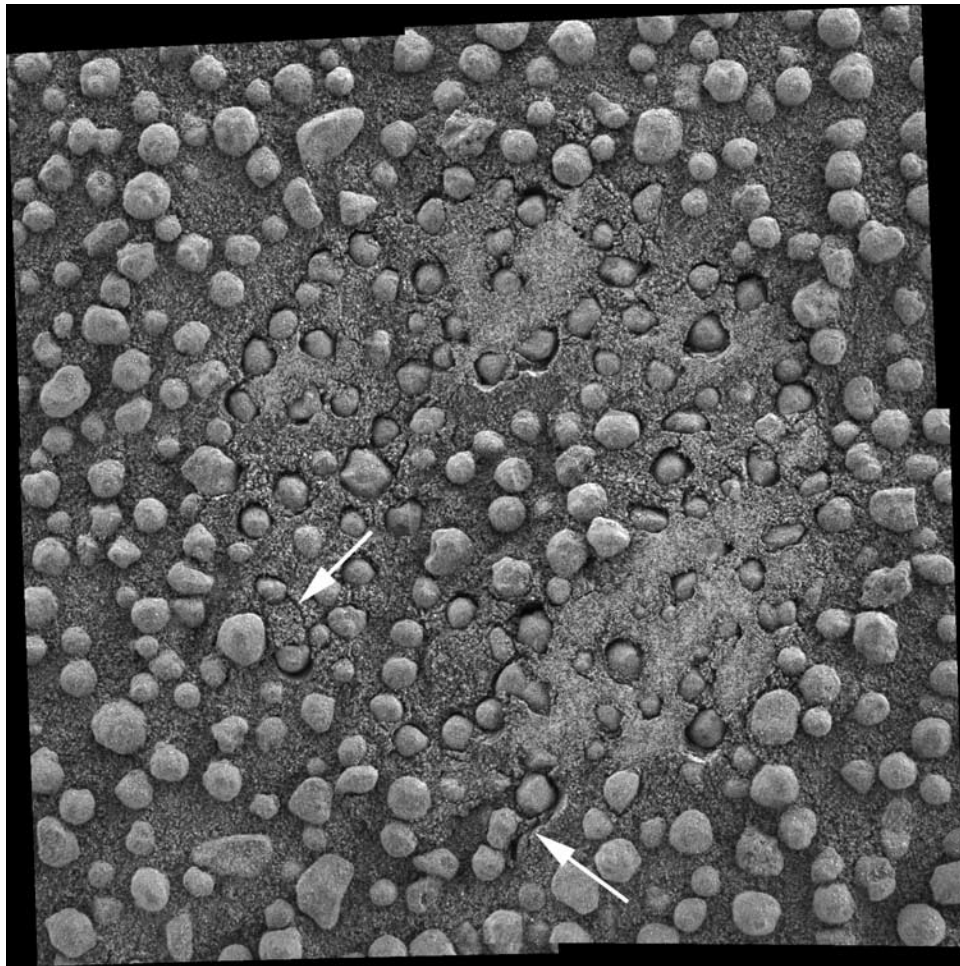


Figure 32. MI mosaic of soil target Troughplain, taken on sol 505 after Mössbauer contact when fully shadowed. Note three common soil components: irregular clasts, rounded particles, and subresolution salt-and-pepper grains. Some pitting of grains near center is indicated by general grain texture rather than conchoidal fracture. No coherent clodding is evident in the sample, but some cohesion is seen around some of the depressed grains (arrows indicate microscale soil fractures). MI mosaic is about 5 cm².

difference in gravity on the surface of Mars versus Earth affects the transition between the types of bed forms expected to be formed by fluid flow, but not their existence [Grotzinger *et al.*, 2005]. Therefore, the MI observations of Overgaard support the conclusion, based on previous observations in Eagle Crater, that water flowed across the surface of Mars in the distant past [Squyres *et al.*, 2004b; Herkenhoff *et al.*, 2004b].

4.2.2. Nodular Rock Surfaces

[66] As noted above, this class is genetically related to the laminar class, though no single-grain layers can be resolved. This relationship is evident in the similarity in grain size and shape, as well as the topography that can be seen below the level surface of abraded targets. Nearly all nodular class targets lie in lower Endurance, and appear to have been more affected by secondary cementation than the laminar rocks higher in the stratigraphic section. The isopachous cements, spherule overgrowths, and nodules may have been formed by the same diagenetic process, with variations in porosity, permeability, composition, or fluid residence time causing the various features [McLennan *et al.*, 2005]. In many ways, the observed nodular texture resembles a

“weathering” texture not uncommon in soluble rocks (i.e., evaporites). The texture can arise from a combination of differential lithification and partial removal of less lithified soluble or nonresistant phases, either by fluid percolation or by wind. The samples showing laminae appear to have formed in an environment where eolian processes deposited very thin (grain-scale thick) layers. The laminae were then cemented by fluid percolation and evaporation. Areas where the texture no longer shows the layering may have either had less cement or fluid available in that location or a subsequent episode of grain removal may have occurred. Grain removal may have been caused by wind action, which would preferentially remove less-resistant phases, or by reintroduction of a fluid that preferentially removed more soluble phases.

[67] Spherule doublets and linearly aligned triplets are expected for concretions but are unlikely in impact or volcanic environments. Observations of the relations between spherules and other features, notably the lack of disruption of stratification at spherule margins, suggest that the spherules formed largely by replacive (rather than displacive) growth [McLennan *et al.*, 2005].

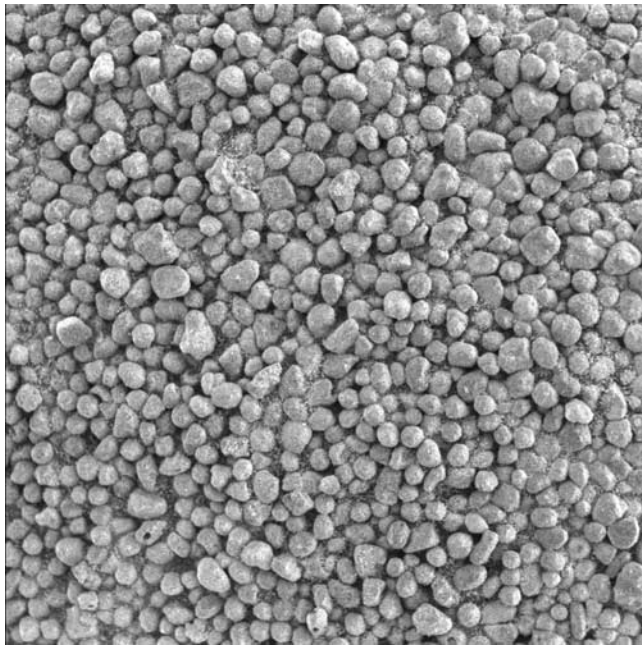


Figure 33. Radiometrically calibrated MI image IM160851916 of target RippleCrest_2, taken on sol 368 in full shadow. Note homogeneity of grain sizes, as observed on all ripple crests at Meridiani. Area shown is 31 mm square.

4.2.3. Angular Rocks

[68] Angular rocks most likely represent fragments of rocks in the other classes. They are classified separately here on the basis of texture rather than origin. The fine-fractured texture, platy appearance and sharp, angular edges all suggest that these rocks are composed of an unknown cementing material that is highly friable.

4.2.4. Massive-Dark Rocks

[69] The massive-dark rocks show little evidence of secondary cementation except for the Normandy target. This class may be representative of the Burns formation lower unit defined by *Grotzinger et al.* [2005], as many of the rocks in this class are either found within or on the outer rim of Endurance Crater, where the stratigraphic sequence might have been overturned.

4.2.5. Massive-Bright Rocks

[70] The cavities in massive-bright rocks may be associated with dissolved minerals or may have previously contained grains or grain aggregates that were preferentially removed by the RAT. The irregular, rough edges of these cavities are more consistent with the latter interpretation, but in either case, chemical dissolution/recrystallization by water is indicated.

4.2.6. Cobbles

[71] The exotic compositional nature of the cobbles argues against their being erosional remnants of an upper stratum [*Jolliff et al.*, 2006]. Pancam data show different spectral signatures for potential clasts and potential matrix, but this is not diagnostic, as varying mineralogy could be either external or internal. We favor the interpretation that the cobbles are remnants of a breccia, but the ultimate determination depends on whether or not the brighter segments of these cobbles represent intrinsic characteristics

(clasts in matrix) or external coatings with different reflectance.

4.2.7. Rock Outcrops

4.2.7.1. Grain Size Distribution

[72] Two sharply contrasting hypotheses have been proposed for the formation of layered rocks at Meridiani Planum. On the basis of grain size, centimeter-scale features identified as festoon cross-beds, and facies relationships in the measured section at Endurance Crater, the MER team interpreted Meridiani outcrop rocks as sandstones, deposited by wind and locally reworked by water [*Squyres et al.*, 2004b, 2006; *Grotzinger et al.*, 2005, 2006]. In contrast, *McCullom and Hynek* [2005] and *Knauth et al.* [2005] interpreted Meridiani rocks as volcanic and impact surge deposits, respectively. Microscopic images can play an important role in the resolution of this debate, because both hypotheses make predictions for the size and sorting of grains within layers. *Squyres et al.* [2006] briefly discussed grain size data from Meridiani outcrop rocks. Here we present grain size distributions and sorting data for MIs of two Meridiani samples: “Cobble Hill,” a bed exposed within Endurance Crater, imaged on sol 144 (Figure 28a), and Overgaard, an outcrop block within the “Olympia” outcrop pavement near Erebus Crater, imaged on sol 721 (Figure 15).

[73] Theoretical and experimental studies of the effects of Martian gravity and atmospheric density on saltation indicate that, while much stronger winds are required to move particles on Mars, the size of grains that are most easily moved by winds is only slightly larger on Mars than on Earth [*Greeley and Iversen*, 1985]. Hence, it is appropriate and useful to compare the size distribution of grains in terrestrial and Martian sandstones. *Ahlbrandt* [1979] published a textural interpretation of 506 eolian sands distributed widely across the Earth’s surface. Eolian deposits consist predominantly of medium- to fine-grained sand; in *Ahlbrandt’s* [1979] sample set, 85% of the deposits have mean grain size in the range 175–375 μm , and few deposits have mean grain sizes above 1 mm or below 62 μm . Eolian sands are also well to moderately well sorted, only slightly skewed toward larger sizes, and mesokurtic (similar to a normal distribution) to slightly platykurtic (relatively “broad shoulders” and tails shorter than predicted by a normal distribution). The size frequency distributions of grains in the two Meridiani outcrop samples display similar characteristics (Figure 29).

[74] The constituent grains of Meridiani outcrop rocks thus meet the predictions inherent in the eolian hypothesis, but are they equally compatible with surge hypotheses? *Sparks* [1976] plotted grain size data for more than 200 surge deposits. Figure 30 shows Sparks’ data on a plot of mean grain size versus sorting. Following convention, *Sparks* [1976] and *Ahlbrandt* [1979] both used the sorting statistic σ_ϕ :

$$\sigma_\phi = (\sigma_{84\text{th percentile}} - \sigma_{16\text{th percentile}})/2.$$

Sparks further examined a subset of 117 samples for which he separated individual components (pumice, lithic grains, and crystals) and redid the analysis, eliminating the fraction smaller than 125 μm . Because the MI cannot reliably



Figure 34. MI image 1M145849709, acquired on sol 199 of target Muffins while fully shadowed, merged with enhanced color from Pancam filters R2 (754 nm), R7 (1009 nm), and R1 (436 nm). Concretions are spherical in shape and relatively blue in color, while popcorn grains are yellower and more irregular in shape. Area shown is 31 mm square.

measure grains less than 100 μm in diameter, this coarser subset is also plotted in Figure 30. In combination, focus on individual components and dismissal of fines result in better sorting. For comparison, we also plotted *Ahlbrandt's* [1979] measurements of eolian sands in Figure 29.

[75] Surge and eolian deposits have nonoverlapping distributions in Figure 30; mean grain sizes overlap at the finer end of the surge grain distribution, but eolian deposits are uniformly better sorted. Because surge deposits do not predict a grain size distribution similar to eolian sands, MI-based quantitative grain size measurements provide a compelling test of eolian versus surge hypotheses. The two

boxes in Figure 30 show the two Meridiani sandstone targets. Clearly, the ancient Martian samples plot within the field for eolian sands but well outside of the field for surge deposits. Thus, MI observations provide strong support for the hypothesis that Meridiani outcrop rocks formed largely by the deposition of windborne grains.

4.2.7.2. Lamination Thickness Distribution

[76] Recently, ancient sedimentary environments on Mars have been investigated using images of outcrops at hand specimen scales by both Opportunity and Spirit [Grotzinger *et al.*, 2005; 2006; Lewis *et al.*, 2008]. We now take the study of the Opportunity landing site a step further by

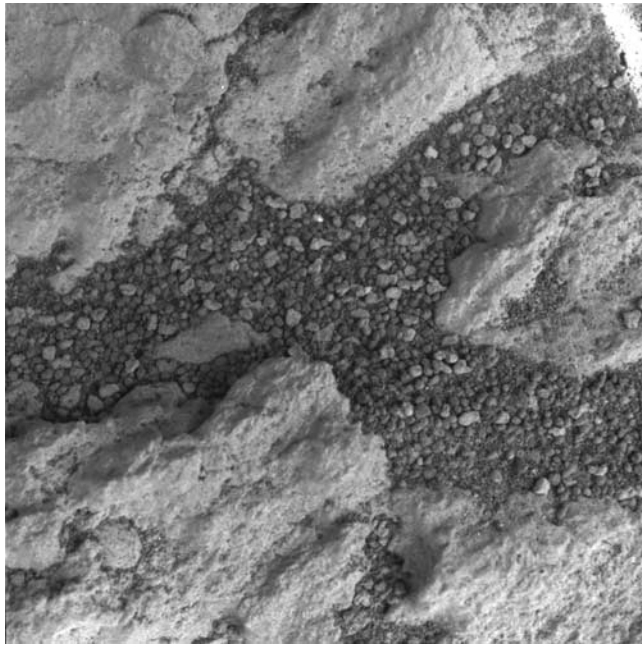


Figure 35. Radiometrically calibrated MI image 1M147006074 of target Munch on rock Escher, taken on sol 212 when mostly shadowed. Small grains can be seen in soil located between crevices in the outcrop. On the basis of Pancam spectra, the larger, brighter grains appear to be pieces of the outcrop while the smaller, darker grains are likely to be basaltic in composition. Area shown is 31 mm square.

quantifying the distribution of lamination thickness, which is readily measured from MI images of the stratification (Figure 30). In terrestrial systems this approach is helpful in distinguishing depositional mechanisms [Rothman and Grotzinger, 1995; Carlson and Grotzinger, 2001]. Here, we describe measurements of lamination thickness from the Burns formation and compare these to measurements for rocks from known terrestrial depositional environments. The goal is to evaluate whether we can discriminate among competing hypotheses for the origin of the Burns formation.

[77] The presence of thin, rhythmic, planar lamination has been interpreted to result from migration of wind ripples, and thus has been used to infer eolian deposition for this facies of the Burns formation [Grotzinger *et al.*, 2005, 2006; Metz *et al.*, 2008]. This interpretation is supported by other data including the presence of large-scale cross-stratification composed of uniformly fine grain size. However, other workers have suggested that these facies could have formed during volcanic or impact-induced base surges [McCollom and Hynke, 2005; Knauth *et al.*, 2005]. These alternative hypotheses have been based primarily on qualitative interpretations of the Burns formation middle unit and without consideration of the particular sedimentologic details of the deposits. In this paper we have measured lamination thicknesses of strata from the middle unit of the Burns formation and from terrestrial rocks known to have formed by base surge, eolian, and even fluvial processes. Lamination thicknesses were measured from images of terrestrial strata and

compared with those from Martian sediments based on images returned by Opportunity (Table 1).

[78] Images acquired by Opportunity were selected so that the camera pointing direction was coplanar with the bedding, so no corrections for apparent dip were required in order to obtain true thickness. Thicknesses were acquired by measuring the distance between successive laminae, normal to bedding. A similar approach was used for terrestrial strata. We attempted to eliminate the problem of missing laminations by only measuring strata that were contiguous and were most clearly resolved in the images. However, there are some uncertainties in the minority of measurements where laminations are not parallel and the thickness between the two is variable. In these situations the average thickness between the two laminae was measured.

[79] Histograms were compiled for both Martian strata and each terrestrial example (Figure 31). Martian laminae from the Burns formation (exposed in Endurance and Eagle craters) are roughly normally distributed, with a mean thickness 0.20 ($1\sigma = 0.08$) cm, based on 75 laminae ($n = 75$). Results for terrestrial eolian deposits from the Jurassic Page Sandstone from the Colorado Plateau are also approximately normally distributed with a mean lamination thickness of 0.14 cm ($1\sigma = 0.05$ cm; $n = 427$). The fluvial, “upper plane bed” facies from the Mt. Shields formation from the Proterozoic Belt Supergroup, Montana, has a similar distribution with mean lamina thickness of 0.14 cm ($1\sigma = 0.05$ cm; $n = 190$). Finally, we measured lamination thicknesses for Pleistocene pyroclastic base surge deposits from Hunts Hole, New Mexico. The distribution of lamina thickness from Hunts Hole is significantly different from the others, with a mean thickness of 1.04 cm ($1\sigma = 0.84$ cm; $n = 156$).

[80] In a comparison of the Martian histogram to the terrestrial analogs (Figure 29) it is qualitatively and quantitatively apparent that the volcanic base surge deposit, which for our purposes also serves as an analog for an impact base surge, has a significantly different distribution (as well as mean) compared to the Martian strata. The terrestrial eolian and fluvial examples, on the other hand, have similar averages and distributions. With the acknowledgment that we have only examined a few environments, we suggest that the middle unit of the Burns formation was not formed by a volcanic base surge event or impact event. Although the distribution of lamination thickness by itself does not allow discrimination between fluvial and eolian origins, the broader context of these deposits does suggest a preference for eolian over fluvial deposition. Planar lamination at the scale observed in the Burns formation could form as a result of sediment transport in high-velocity, upper flow regime subaqueous flows [Southard and Boguchwal, 1990]. However, planar-laminated deposits formed in the upper flow regime are often on the order of tens of centimeters thick [Metz *et al.*, 2008], in contrast to the thickness of planar-laminated deposits in the Burns formation which is on the order of several meters thick at “Burns Cliff” [Grotzinger *et al.*, 2005]. While possible in terrestrial deposits, this is rare [Metz *et al.*, 2008]. Therefore, we suggest that an eolian origin for the planar- to low-angle-laminated deposits in the Burns formation is the most likely depositional process.

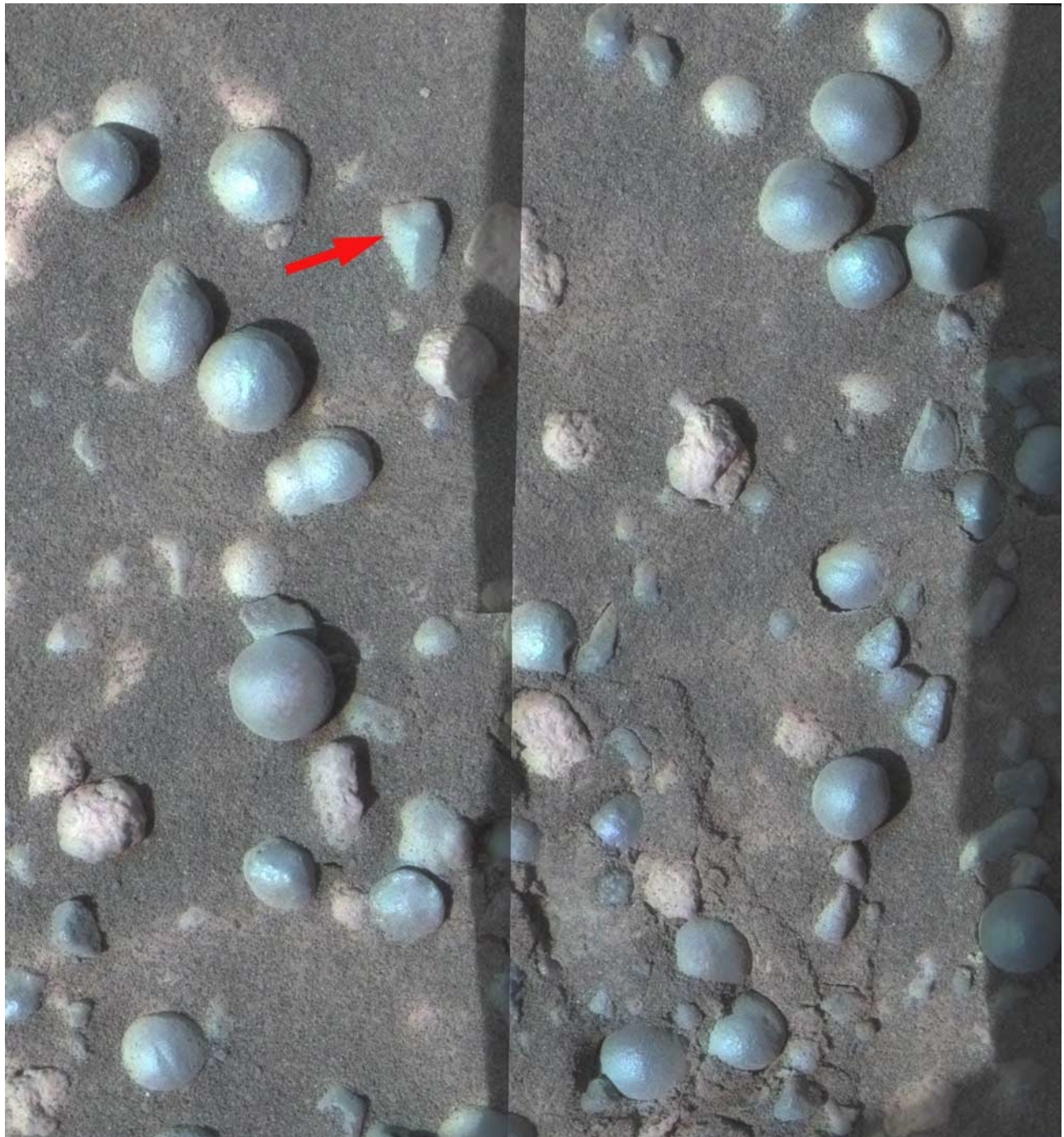


Figure 36. MI mosaic of Blueberries2, acquired on sol 221, merged with enhanced color from Pancam filters L2 (753 nm), L5 (535 nm), and L6 (482 nm). Arrow shows rock fragment that is spectrally different from the spherules as seen in 13-filter Pancam data. Shadow edge is visible at right edge of each frame (illumination from lower left); mosaic is about 5 cm across.

4.3. Soil Observations and Interpretations

[81] The majority of soils observed by the MI between sols 91 and 900 represent the lag that dominates the plains of Meridiani Planum. These lag soils consist of a mixture of different grains, including basaltic sand, dust, millimeter-scale spherules interpreted as concretions released during outcrop erosion, spherule fragments, coated partly buried spherules, basalt fragments, sedimentary outcrop fragments,

and centimeter-size cobbles [Soderblom *et al.*, 2004; Weitz *et al.*, 2006]. Beneath the lag surface, the soils are dominated by basalt sands and dust. MI observations of the soils have been valuable for determining the sizes, shapes, and morphologies of the various grains that compose the soils. In particular, the grain morphology can be used to infer the nature of the source rock, mineralogy of the grain, and degree of abrasion during transport [e.g., Tucker, 1981]. In

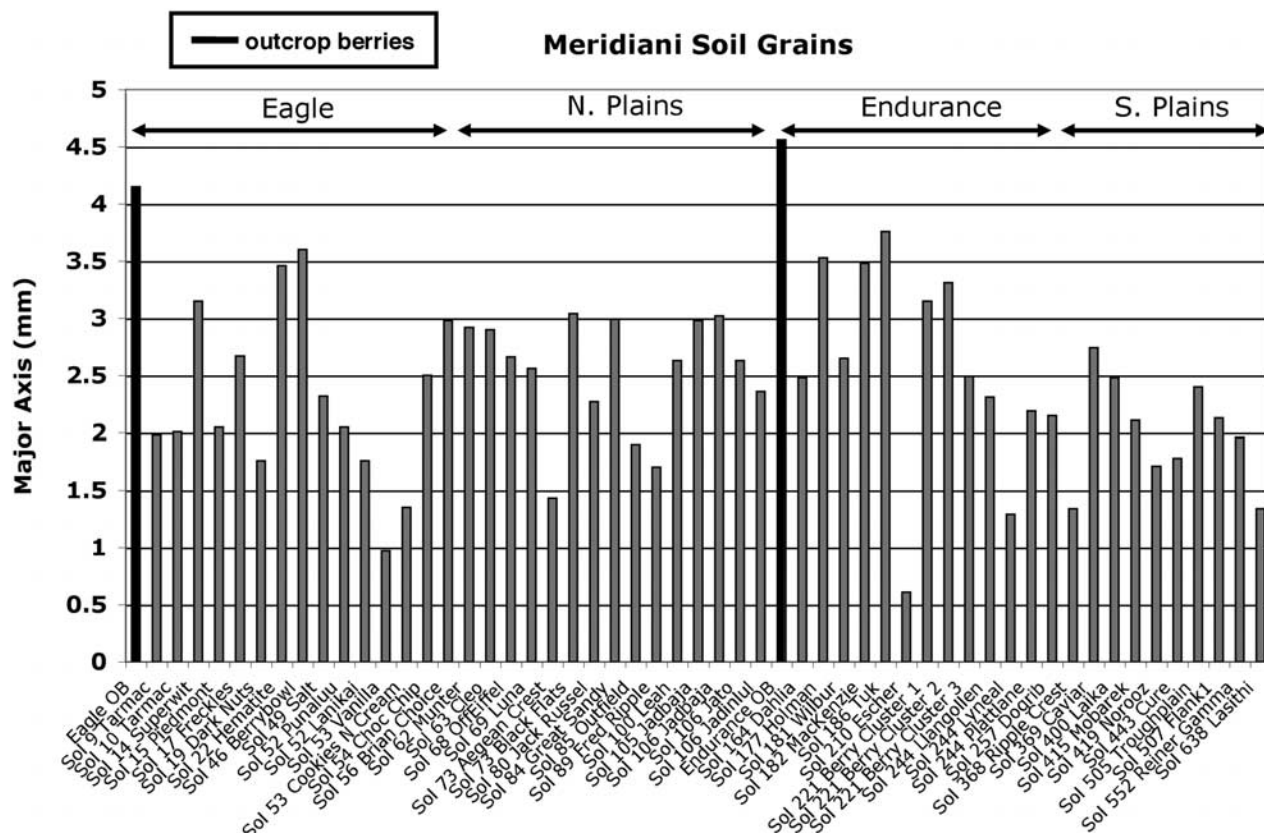


Figure 37. Plot showing average major axis of grains in MI images of various soils at Meridiani Planum. Also shown are average lengths of outcrop spherules (concretions) still embedded within rocks at Eagle (Eagle outcrop berry) and Endurance (Endurance outcrop berry) craters. Grains within Eagle and Endurance have a greater range of sizes compared to the plains. Grains measured on ripple crests tend to be similar in size. Northern interripple plains have slightly larger average grain sizes compared to southerly interripple plains, which is a reflection of the smaller sizes of spherules in the southern soils.

places where the soil has been disturbed by the rover wheels or landing airbags, larger grains are pushed into the finer-grained soil by the full diameter of the grains. This compaction indicates the presence of a large population of smaller grains, as is the case at Gusev Crater [Arvidson *et al.*, 2004]. Figure 32 shows a typical soil that has been compressed by one of the IDD instruments; all four common soil components previously identified in earlier sols [Yen *et al.*, 2005] (i.e., dust, small grains, irregular clasts, and more rounded clasts) can be seen here. Absent from this image are spherules, shown to be rich in hematite [Klingelhöfer *et al.*, 2004; Morris *et al.*, 2006], which are also common to a greater or lesser extent in MI soil targets.

4.3.1. Primary Mission Summary

[82] During the initial 90 sols of the mission, MI observations were dominated by soils within Eagle Crater and a few in the plains between Eagle and Endurance craters. The soils within Eagle Crater varied considerably in their grain sizes and shapes [Soderblom *et al.*, 2004; Weitz *et al.*, 2006]. Grains near the center of the crater were generally smaller than those near the outcrop and one soil at the center of Eagle was composed of dark sand ripples [Sullivan *et al.*, 2005]. Soils closer to the outcrop tended to have larger spherules because wind erosion of the outcrop enabled the

more resistant spherules embedded in the outcrop to concentrate in the adjacent soils. Patches of soil composed exclusively of dark sand were observed by the MI between outcrop blocks in Eagle (sol 27 “Red Sea”), while patches of soil composed of only dust were found just outside the crater rim in the downwind direction (sol 59 “Dendrites”). The composition of the bright dust (grains not resolved by the MI) has been interpreted to derive from a global unit, rather than local rocks and other loose particles, while the darker grains show a basaltic mineralogy that reflects either similarities in parent rock lithology or another global unit [Yen *et al.*, 2005]. Neither of these components appears to have been derived from local materials, as they are compositionally more similar to other soils across the planet than the local rocks, outcrops and loose particles [Yen *et al.*, 2005]. These authors conclude that fine-grained soil particles are likely the product of eolian transport and redistribution. The pitted, abraded texture of the larger, irregular clasts supports this claim.

4.3.2. First Three Extended Missions

[83] Soils in the plains between Eagle and Endurance craters do not show the same heterogeneities in grain sizes and shapes as those seen within Eagle Crater. Instead, the soils can be divided into ripples and interripples soils.

Grains on ripples are dominated by hematite-rich spherules of a remarkably homogeneous size distribution (1.3–1.8 mm diameter) with finer basalt sand and dust interspersed between the spherules [Weitz *et al.*, 2006]. The spherules display high levels of rounding and sphericity (seen at the target “RippleCrest_2” in Figure 33) and act as an armoring agent [Soderblom *et al.*, 2004; Sullivan *et al.*, 2005]. This size range is significantly smaller than that observed for spherules in the immediately underlying outcrop material and may indicate derivation from overlying outcrops that formed under a differing hydrodynamic diagenetic regime.

[84] Soils that are not located on the ripples are a mixture of spherules, rock fragments, basalt sand, and dust. Many of the millimeter-size rock fragments and larger centimeter-size cobbles are interpreted as pieces of meteorites, impact ejecta, or the outcrop lithology [Weitz *et al.*, 2006; Squyres *et al.*, 2006].

[85] Examination of the soils within Endurance Crater reveals grains not seen on the plains or at Eagle Crater. Rounded grains informally termed “popcorn” are found in association with outcrop lower down the walls of Endurance Crater (Figure 34). They are interpreted as originating within the outcrop rocks from a secondary generation of cementation and recrystallization formed around a variety of nucleation sites, including, but not restricted to the spherules [McLennan *et al.*, 2005].

[86] MI images of the outcrop near the floor of Endurance Crater also include cracks and depressions filled with small granules and basaltic sand (Figure 35). Weitz *et al.* [2006] measured the sizes of these grains to be 0.61 ± 0.22 mm, which represents the smallest population of grains resolved by the MI (i.e., >0.1 mm) thus far at Meridiani. There are actually two different types of grains seen at “Escher,” with the larger, more irregularly shaped and brighter grains interpreted to be pieces of the outcrop while the smaller, darker grains appear to be basalt granules mixed in with the finer basalt sand. Additional soils near the floor of Endurance have spherules similar in size to the 4.5 mm diameter spherules still embedded in the outcrop (Figure 36). MI images of these soils also show centimeter-size rock fragments that are more angular in shape than the spherical spherules, perhaps representing impact ejecta or meteorite fragments now mixed into the soils.

[87] Examination of the ripples and interripple plains encountered after egress from Endurance Crater shows similar grains to those seen earlier in the plains soils. The main difference between these more southerly soils appears to be in the sizes of the grains that compose the lag deposit of the interripple plains. Figure 37 shows a plot of the average size of soil grains measured in each MI image. The size of the grains in the northerly plains between Eagle and Endurance craters is slightly larger than the grains seen in the soils as Opportunity drove south away from Endurance Crater. The size difference is most obvious in the spherules that compose the interripple plains, with those to the south being about 1 mm smaller. Weitz *et al.* [2006] attribute the smaller sizes of spherules in the southerly soils to smaller sizes of spherules observed in the local outcrop rocks that are weathering out and mixing into the soils as windblown sand grains erode the outcrop.

[88] The size of spherules that compose the soils on the ripples (Figure 33) remained similar even though the ripples



Figure 38. Radiometrically calibrated MI image 1M173193890 of target Track, acquired on sol 507 in full shadow. Soil within track created by rover wheels is composed of fine grains and appears relatively high in reflectance, suggesting a high proportion of dust. Mössbauer imprint into soil (lower left) is well preserved, indicating that soil becomes consolidated when force is applied. Area shown is 31 mm square.

are larger in overall size [Sullivan *et al.*, 2007]. Opportunity spent a significant amount of time studying “Purgatory Ripple,” where the rover was stuck for several weeks in the fine-grained soils of the ripple interior (Figure 38).

5. Conclusions

[89] The data returned by Opportunity’s Microscopic Imager have provided key constraints in the interpretation of MER observations of various types of rocks and soils on Meridiani Planum. Evidence for both primary sedimentary structures and secondary mineralization is seen in MI images. Digital elevation models of MI stereo observations of the rock target Overgaard support the previous conclusion that liquid water once flowed across the surface of Meridiani Planum. The grain size and lamina thickness distributions observed in sandstones in the Burn formation indicate that they were formed by eolian deposition. Soil grain sizes and shapes are more homogeneous on the Meridiani plains than in Eagle Crater, with well-sorted spherules dominating ripple surfaces. The size of spherules between ripples decreases by about 1 mm from north to south along Opportunity’s traverse.

[90] The relative (pixel-to-pixel) radiometric calibration accuracy of typical MI data acquired during the first three extended missions is 1.5%, and the absolute radiometric calibration accuracy is 20% or better. The MI continues to acquire good images as the rover explores Victoria Crater. MI data acquired after sol 900 will be described and discussed in future publications.

Table A1. Summary of Opportunity MI Observations, Sols 1–900

Sol	Starting Image ID	Target	Feature	Target Type	No. ^a	CS ^b	S/M ^c	Relation to RAT/MB ^d	Pancam Sequence ^e
2	1M128363423	NA	NA	Health Check	1	C	M	NA	None
9	1M128996928	Sidewalk	MerLot	Soil	5	O	M	NA	p2369, Sol 008
10	1M129070954	Tarmac	MerLot	Soil	5	O	M	PreMB	p2374, Sol 012
10	1M129071300	Tarmac	MerLot	Soil	1	C	M	PreMB	p2374, Sol 012
12	1M129247958	Tarmac	MerLot	Soil	5	O	M	PostMB	p2374, Sol 012
12	1M129248319	Tarmac	MerLot	Soil	1	C	M	PostMB	p2374, Sol 012
14	1M129426120	Wit	Target	Soil	15	C	S	PreMB	p2549, Sol 014
14	1M129430151	Wit	Target	Soil	5	C	M	PostMB	p2549, Sol 014
15	1M129514765	Piedmont	Stone Mt.	Soil	5	O	M	NA	p2549, Sol 014
15	1M129515505	Robert E	Stone Mt.	Outcrop	10	O	S	NA	p2549, Sol 014
17	1M129692361	Freckles	BerryFlats	Soil	5	O	M	PreMB	p2555, Sol 017
17	1M129695788	Freckles	BerryFlats	Soil	3	O	M	PostMB	p2555, Sol 017
18	1M129781117	DarkNuts	Bravo_Flats	Soil	5	O	M	PreMB	p2557, Sol 018
19	1M129869615	DarkNuts	Bravo_Flats	Soil	5	O	M	PreMB	p2557, Sol 018
19	1M129875002	DarkNuts	Bravo_Flats	Soil	3	O	M	PostMB	p2565, Sol 019
20	1M129958677	Flashy2	Charlie_Flats	Soil	5	O	M	PreMB	p2564, Sol 020
20	1M129959233	Flashy2	Charlie_Flats	Soil	1	C	M	PreMB	p2564, Sol 020
20	1M129961977	Flashy2	Charlie_Flats	Soil	3	O	M	PostMB	p2564, Sol 020
22	1M130137047	Hema2	Hematite Slope	Soil	5	O	M	PreMB	p2565, Sol 021
22	1M130137481	Hema2	Hematite Slope	Soil	1	C	M	PreMB	p2565, Sol 021
23	1M130225038	Hema2	Hematite Slope	Soil	3	O	M	PostMB	p2565, Sol 021
23	1M130225457	Hematrack1	Hematite Slope	Soil (track)	7	O	M	NA	p2565, Sol 021
23	1M130225938	Hematrack1	Hematite Slope	Soil (track)	1	C	M	NA	p2565, Sol 021
24	1M130314030	Hematrench wall2	BigDig	Trench	7	O	M	PreMB	p2385, Sol 026
24	1M130314510	Hematrench wall2	BigDig	Trench	1	C	M	PreMB	p2385, Sol 026
24	1M130314813	Hematrench1	BigDig	Trench	7	O	M	PreMB	p2385, Sol 026
24	1M130315505	Hematrench1	BigDig	Trench	1	C	M	PreMB	p2385, Sol 026
25	1M130404206	Hematrench1	BigDig	Trench	1	O	M	Post MB	p2385, Sol 026
25	1M130404446	HemaTrenchWall	BigDig	Trench	5	O	M	NA	p2385, Sol 026
25	1M130404829	Hematrench wall2	BigDig	Trench	1	O	M	NA	p2385, Sol 026
25	1M130404892	HemaTrenchWall2Below	BigDig	Trench	5	O	M	NA	p2385, Sol 026
25	1M130405277	HemaTrenchWall5	BigDig	Trench	5	O	M	NA	p2385, Sol 026
26	1M130491401	Hematrench wall2	BigDig	Trench	3	O	M	Post MB	p2385, Sol 026
27	1M130580128	Shalt	Stone Tablet	Outcrop	5	O	M	PreMB	p2546, Sol 041
27	1M130580905	Shalt	Stone Tablet	Outcrop	1	C	M	PreMB	p2546, Sol 041
27	1M130585004	Red Sea	Stone Tablet	Outcrop	5	O	M	PreMB	p2546, Sol 041
27	1M130585376	Red Sea	Stone Tablet	Outcrop	1	C	M	PreMB	p2546, Sol 041
28	1M130669576	TopMI	McKittrick	Outcrop	5	O	M	PreMB	p2533, Sol 037
28	1M130669958	TopMI	McKittrick	Outcrop	1	C	M	PreMB	p2533, Sol 037
28	1M130670167	UpperMI	McKittrick	Outcrop	5	O	M	PreMB	p2533, Sol 037
28	1M130670552	UpperMI	McKittrick	Outcrop	1	C	M	PreMB	p2533, Sol 037
28	1M130670761	MiddleRAT	McKittrick	Outcrop	10	O	S	PreMB	p2533, Sol 037
28	1M130671514	MiddleRAT	McKittrick	Outcrop	1	C	M	PreMB	p2533, Sol 037
28	1M130671710	LowerMI	McKittrick	Outcrop	5	O	M	PreMB	p2533, Sol 037
28	1M130672136	LowerMI	McKittrick	Outcrop	1	C	M	PreMB	p2533, Sol 037
28	1M130672440	GuadalupeRATLower	Guadalupe	Outcrop	10	O	S	PreMB	p2387, Sol 027
28	1M130673194	GuadalupeRATLower	Guadalupe	Outcrop	1	C	M	PreMB	p2387, Sol 027
28	1M130673422	Middle	Algerita	Outcrop	5	O	M	NA	p2531, Sol 036
28	1M130673852	Middle	Algerita	Outcrop	1	C	M	NA	p2531, Sol 036
29	1M130759958	McRATRight	McKittrick	Outcrop	5	O	M	PreRAT	p2533, Sol 037
29	1M130760302	McRATRight	McKittrick	Outcrop	1	C	M	PreRAT	p2533, Sol 037
29	1M130760650	GuadalupeRATRight	Guadalupe	Outcrop	10	O	S	NA	p2531, Sol 036
29	1M130761427	GuadalupeBerry	Guadalupe	Outcrop	5	O	M	NA	p2387, Sol 027
29	1M130761822	GuadalupeBerry	Guadalupe	Outcrop	1	C	M	NA	p2387, Sol 027
29	1M130762034	McKittrick_base	McKittrick	Outcrop	5	O	M	NA	p2546, Sol 041
29	1M130762436	McKittrick_base	McKittrick	Outcrop	1	C	M	NA	p2546, Sol 041
29	1M130762666	JimsBerry	McKittrick	Outcrop	5	O	M	NA	p2546, Sol 041
29	1M130763016	JimsBerry	McKittrick	Outcrop	1	C	M	NA	p2546, Sol 041
30	1M130846336	GuadalupeRATTop	Guadalupe	Outcrop	5	O	M	NA	p2387, Sol 027
30	1M130859270	MiddleRAT	McKittrick	Outcrop	12	O	S	PostRAT	p2533, Sol 037
33	1M131117213	MiddleRAT	McKittrick	Outcrop	3	O	M	PostRAT	p2533, Sol 037
34	1M131201538	King2	Guadalupe	Outcrop	3	O	M	PreRAT	p2387, Sol 027
34	1M131212713	King2	Guadalupe	Outcrop	3	O	M	PostRAT	p2598, Sol 035
35	1M131295970	King3	Guadalupe	Outcrop	6	O	S	PostRAT	p2598, Sol 035
35	1M131296470	King3	Guadalupe	Outcrop	2	C	M	PostRAT	p2598, Sol 035
38	1M131556907	Paydirt1	IDD_Fine_soil	Soil	10	O	S	PreMB	p2536, Sol 037
38	1M131557959	Paydirt1	IDD_Fine_soil	Soil	2	C	M	PreMB	p2536, Sol 037
38	1M131558117	Paydirt1	IDD_Fine_soil	Soil	10	O	S	PostMB	p2536, Sol 037
38	1M131559248	Paydirt1	IDD_Fine_soil	Soil	2	C	M	PostMB	p2536, Sol 037
38	1M131559422	Capture magnet	Rover	Magnet	6	O	S	NA	p2536, Sol 037
38	1M131564197	Capture magnet	Rover	Magnet	1	C	M	NA	p2536, Sol 037
38	1M131564268	Filter magnet	Rover	Magnet	6	O	S	NA	p2536, Sol 037

Table A1. (continued)

Sol	Starting Image ID	Target	Feature	Target Type	No. ^a	CS ^b	S/M ^c	Relation to RAT/MB ^d	Pancam Sequence ^e
38	1M131564733	Filter magnet	Rover	Magnet	1	C	M	NA	p2536, Sol 037
39	1M131647578	LCc3	Last Chance	Outcrop	18	O	S	NA	p2538, Sol 038
39	1M131649892	LCb9	Last Chance	Outcrop	48	O	S	NA	p2538, Sol 038
39	1M131653201	LCb9	Last Chance	Outcrop	14	O	M	NA	p2538, Sol 038
39	1M131654287	LCa7	Last Chance	Outcrop	48	O	S	NA	p2538, Sol 038
40	1M131733971	LCc4	Last Chance	Outcrop	6	O	S	NA	p2538, Sol 038
40	1M131734473	LCa2	Last Chance	Outcrop	12	O	S	NA	p2538, Sol 038
40	1M131735575	LCb2	Last Chance	Outcrop	6	O	S	NA	p2538, Sol 038
41	1M131830206	East Dells	Dells	Outcrop	48	O	S	NA	p2263, Sol 017
42	1M131912346	Mojo2	Flatrock	Outcrop	6	O	S	PreRAT	p2549, Sol 042
43	1M132015283	Mojo2	Flatrock	Outcrop	3	O	M	Mid-RAT	p2547, Sol 042
45	1M132180461	Mojo2	Flatrock	Outcrop	6	O	S	PostRAT	p2560, Sol 045
45	1M132180881	Mojo2	Flatrock	Outcrop	1	C	M	PostRAT	p2560, Sol 045
46	1M132266828	Bluecrop	Berry_Bowl	Spheres	5	O	M	PreMB	p2563, Sol 020
46	1M132267223	Rubel2	Berry_Bowl	Spheres	5	O	M	NA	p2563, Sol 020
47	1M132355397	Rubel2	Berry_Bowl	Spheres	5	O	M	NA	p2563, Sol 020
48	1M132444176	Empty	Berry_Bowl	Spheres	3	O	M	PreBrush	p2563, Sol 020
48	1M132444465	Tripleberry	Berry_Bowl	Spheres	3	O	M	NA	p2563, Sol 020
48	1M132444642	Empty	Berry_Bowl	Spheres	3	O	M	PostBrush	p2568, Sol 048
49	1M132535500	Filling	Raspberry_Newton	Outcrop	6	O	S	NA	p2584, Sol 051
49	1M132535896	Filling	Raspberry_Newton	Outcrop	1	C	M	NA	p2584, Sol 051
49	1M132536108	Salt	PatioDirt	Soil	6	O	S	NA	p2584, Sol 051
49	1M132536524	Salt	PatioDirt	Soil	1	C	M	NA	p2584, Sol 051
50	1M132624624	Enamel1	RealSharksTooth	Outcrop	6	O	S	NA	p2571, Sol 049
50	1M132625172	Lamination	LaminatedShark	Outcrop	6	O	S	NA	p2571, Sol 049
52	1M13280806	Punaluu	Goal5_hematite_waves	Soil	5	O	M	PostMB	p2588, Sol 052
52	1M132808464	Lanikai	Goal5_hematite_waves	Soil	5	O	M	NA	p2588, Sol 052
53	1M132896233	Vanilla	Goal3_bouncemark	Soil	5	O	M	PostMB	p2598, Sol 053
53	1M132896619	Cookies'n cream	Goal3_bouncemark	Soil	5	O	M	NA	p2599, Sol 053
54	1M132982784	Coconut2	Goal4_center_soil	Soil	3	O	M	NA	p2530, Sol 054
54	1M132983130	ChocolateChip	Goal4_center_soil	Soil	5	O	M	NA	p2530, Sol 054
55	1M133068975	Mbone	Goal2	Trench	5	O	M	PostMB	p2543, Sol 055
55	1M133069353	Bright	Goal2	Trench	14	O	S	NA	p2543, Sol 055
55	1M133070382	RippleFour	Goal2	Soil	5	O	M	NA	p2543, Sol 055
55	1M133070785	RippleOne	Goal2	Soil	5	O	M	NA	p2543, Sol 055
55	1M133072174	WallOne	Goal2	Trench wall	5	O	M	NA	p2543, Sol 055
55	1M133072557	WallTwo	Goal2	Trench wall	5	O	M	NA	p2543, Sol 055
56	1M133157787	Brian's Choice	Goal1_low hematite	Soil	5	O	M	PostMB	p2548, Sol 056
59	1M133421524	Dendrites	Mont Blanc	Soil	5	O	M	NA	p2558, Sol 059
59	1M133421936	Les Hauches	Mont Blanc	Soil	5	O	M	PreMB	p2558, Sol 059
59	1M133422280	Les Hauches	Mont Blanc	Soil	1	C	M	PreMB	p2558, Sol 059
61	1M133598234	Les Hauches	Mont Blanc	Soil	3	O	M	PostMB	p2559, Sol 061
62	1M133692453	Munter	DarkPatch	Soil	3	O	M	PostMB	p2563, Sol 062
63	1M133775959	Cleo_3	White_streak	Soil	5	O	M	PreMB	p2572, Sol 063
63	1M133781967	Cleo_3	White_streak	Soil	1	O	M	PostMB	None
65	1M133954829	Achsel	BounceRock	Rock	7	O	M	NA	p2570, Sol 063
65	1M133955529	Cake	BounceRock	Rock	20	O	S	PreRAT	p2570, Sol 063
65	1M133957122	Cake	BounceRock	Rock	4	C	M	PreRAT	p2570, Sol 063
65	1M133957622	Traube	BounceRock	Rock	5	O	M	NA	p2570, Sol 063
65	1M133958382	Glanz2	BounceRock	Rock	5	O	M	PreMB	p2570, Sol 063
67	1M134130985	Case	BounceRock	Rock	25	O	S	PostRAT	p2581, Sol 068
67	1M134131328	Case	BounceRock	Rock	4	C	M	PostRAT	p2581, Sol 068
67	1M134138588	Eifel	BounceRock	Rock	3	O	M	PostMB	p2581, Sol 068
67	1M134143520	Loreley	BounceRock	Rock	3	O	M	PostMB	p2581, Sol 068
67	1M134143872	Fips2	BounceRock	Rock	5	O	M	PostMB	p2581, Sol 068
68	1M134219713	Glanz2	BounceRock_Soil	Soil	5	O	M	NA	p2570, Sol 063
69	1M134308944	Luna2	RightSoil	Soil	5	O	M	NA	p2581, Sol 068
69	1M134315180	Grace	RedHerring	Rock	3	O	M	PostMB	p2581, Sol 068
69	1M134320050	Wrigley2	RedHerring	Rock	3	O	M	PostMB	p2581, Sol 068
69	1M134320496	Ginny_2	RedHerring	Rock	5	O	M	NA	p2581, Sol 068
69	1M134320614	Maggie	RedHerring	Rock	3	O	M	PostMB	p2581, Sol 068
73	1M134664420	Aegean_crest	Seas	Soil	5	O	M	PreMB	p2589, Sol 073
73	1M134671768	Aegean_crest	Seas	Soil	3	O	M	PostMB	p2589, Sol 073
73	1M134672075	Black_Flats	Seas	Soil	5	O	M	PreMB	p2589, Sol 073
80	1M135284013	Jeff'sChoice	DogPark	Trench	3	O	M	PostMB	p2421, Sol 081
80	1M135284363	JackRussel	DogPark	Soil	5	O	M	PreMB	p2421, Sol 081
80	1M135284929	RipX	DogPark	Trench edge	7	O	M	NA	p2421, Sol 081
80	1M135285495	BeagleBurrow	DogPark	Trench floor	5	O	M	PreMB	p2421, Sol 081
80	1M135285968	NewRipXbelow	DogPark	Trench wall	5	O	M	NA	p2421, Sol 081
80	1M135292516	JackRussel	DogPark	Soil	3	O	M	PostMB	p2421, Sol 081
80	1M135296825	BeagleBurrow	DogPark	Trench floor	3	O	M	PostMB	p2421, Sol 081
84	1M135640864	Great Sandy	Nullarbor	Soil	5	O	M	PreMB	p2530, Sol 084

Table A1. (continued)

Sol	Starting Image ID	Target	Feature	Target Type	No. ^a	CS ^b	S/M ^c	Relation to RAT/MB ^d	Pancam Sequence ^e
84	1M135646608	Great Sandy	Nullarbor	Soil	3	O	M	PostMB	p2530, Sol 084
85	1M135729716	Outfield	Baseball	Soil	5	O	M	NA	p2533, Sol 085
85	1M135737791	Infield	Baseball	Rock	3	O	M	NA	p2533, Sol 086
86	1M135817578	Golf	Pilbara	Rock	5	O	M	PreRAT	p2532, Sol 085
87	1M135906881	Golf	Pilbara	Rock	25	O	S	PostRAT	p2542, Sol 088
89	1M136083473	Fred_Ripple	PHOTIDD_plains	Ripple	5	O	M	NA	p2551, Sol 091
89	1M136083929	Nougat	PHOTIDD_plains	Track	5	O	M	NA	p2551, Sol 091
90	1M136188650	Sky Flat	NA	Sky	1	O	M	NA	None
90	1M136188715	Sky Flat	NA	Sky	1	C	M	NA	None
91	1M136268404	Fred_Ripple	PHOTIDD_plains	Ripple	3	O	M	PostMB	p2551, Sol 091
100	1M137060845	Leah	Work_Volume	Soil	4	O	S	PostMB	p2570, Sol 101
105	1M137503553	Jab_bal_ja	LionStone	Soil	5	O	M	NA	p2577, Sol 104
105	1M137503964	Kimba	LionStone	Ripple	5	O	M	NA	p2577, Sol 104
105	1M137504426	Elsa	LionStone	Rock	5	O	M	NA	p2577, Sol 104
105	1M137504868	Nala	LionStone	Rock	10	O	S	PreMB	p2577, Sol 104
106	1M137593003	Jad_Ben_Lul	LionStone	Soil	5	O	M	NA	p2577, Sol 104
106	1M137593451	Jato	LionStone	Soil	5	O	M	NA	p2577, Sol 104
106	1M137593860	Jad_In_Lul	LionStone	Soil	5	O	M	NA	p2577, Sol 104
107	1M137681149	Numa	LionStone	Rock	5	O	M	PreRAT	p2577, Sol 104
107	1M137690620	Numa	LionStone	Rock	5	O	M	PostRAT	p2582, Sol 108
108	1M137781951	Numa	LionStone	Rock	12	O	S	PostRAT	p2582, Sol 108
121	1M138924738	Barberton	NA	Cobble	8	O	S	NA	p2535, Sol 123
122	1M139013191	Barberton	NA	Cobble	2	O	M	NA	p2535, Sol 123
123	1M139112545	McDonnell	Hilltop	Soil	4	O	S	PostMB	p2538, Sol 126
124	1M139191039	Center_0	Pyrrho	Rock	60	O	M	NA	p2531, Sol 123
125	1M139279856	Tier1	Diogenes	Rock	13	O	S	NA	p2297, Sol 117
125	1M139280874	Tier2	Diogenes	Rock	17	O	S	NA	p2297, Sol 117
125	1M139282371	Tier3a	Diogenes	Rock	15	O	S	NA	p2297, Sol 117
125	1M139283860	Tier5a	Diogenes	Rock	15	O	S	NA	p2297, Sol 117
138	1M140434086	Tennessee	Tennessee3	Rock	3	O	M	PreRAT	p2374, Sol 135
139	1M140522167	Vols	Tennessee3	Rock	15	O	S	PostRAT	p2550, Sol 140
142	1M140791410	Siula_Grande	Kentucky	Rock	23	O	S	NA	p2378, Sol 139
142	1M140793161	K2	Kentucky	Rock	23	O	S	NA	p2378, Sol 139
143	1M140877373	Cobble Hill	Kentucky	Rock	5	O	M	NA	p2378, Sol 150
144	1M140976080	C-D Boundary	Kentucky	Rock	15	O	S	NA	p2378, Sol 152
145	1M141058167	Virginia	Layer C	Rock	5	O	M	PreRAT	p2378, Sol 158
145	1M141058620	Cobble Hill	Layer C	Rock	15	O	S	PostRAT	p2575, Sol 150
146	1M141149876	London	Ontario	Rock	5	O	M	PreRAT	p2378, Sol 158
146	1M141150332	Virginia	Layer C	Rock	15	O	S	PostRAT	p2575, Sol 150
148	1M141321671	Offset from Virginia	Layer C	Rock	1	O	M	MB	p2378, Sol 158
148	1M141321918	Offset from London	Ontario	Rock	5	O	M	PreRAT	p2378, Sol 158
149	1M141409684	London_centered	Ontario	Rock	15	O	S	PostRAT	p2575, Sol 150
151	1M141588116	Grindstone (E1)	Manitoba	Rock	5	O	M	NA	p2576, Sol 151
152	1M141690013	Grindstone (E1)	Manitoba	Rock	20	O	S	PostRAT	p2384, Sol 157
152	1M141691232	Kettlestone	Manitoba	Rock	4	O	S	NA	p2384, Sol 157
153	1M141764810	Kettlestone	Manitoba	Rock	4	O	M	PreRAT	p2576, Sol 151
154	1M141867533	Kettlestone	Manitoba	Rock	20	O	S	PostRAT	p2384, Sol 157
154	1M141868883	Filter magnet	Rover	Magnet	2	O	M	NA	p2384, Sol 157
154	1M141869148	Capture magnet	Rover	Magnet	4	O	M	NA	p2384, Sol 157
158	1M142208743	NW_Territory	Hallvard	Soil	15	O	S	NA	p2586, Sol 161
160	1M142386190	Drammensfjord	Millstone	Rock	4	O	S	PreRAT	p2590, Sol 167
162	1M142563957	Drammensfjord	Millstone	Rock	24	O	S	PostRAT	p2586, Sol 161
164	1M142741514	My_Dehlia	Millstone	Soil	8	O	S	NA	p2384, Sol 157
165	1M142829753	Dehlia	Millstone	Soil	6	O	S	PreMB	p2590, Sol 167
167	1M143007937	Dehlia	Millstone	Soil	1	O	M	PostMB	p2586, Sol 161
167	1M143009398	Filter magnet	Rover	Magnet	2	O	M	NA	p2586, Sol 161
167	1M143009680	Capture magnet	Rover	Magnet	2	O	M	NA	p2586, Sol 161
173	1M143541826	Arnold_Ziffel	Hoghead	Rock	8	O	S	PreMB	p2598, Sol 170
174	1M143629134	Arnold_Ziffel	Hoghead	Rock	20	O	S	PreMB	p2598, Sol 170
175	1M143717908	Arnold_Ziffel	Hoghead	Rock	1	O	M	PostMB	p2532, Sol 175
176	1M143807453	RazorCluster	Trac_2	Rock	8	O	S	NA	p2598, Sol 170
177	1M143895966	Holman_3	Diamond Jenness	Rock	16	O	S	PreRAT	p2533, Sol 176
177	1M143905332	Holman_3	Diamond Jenness	Rock	16	O	S	PostRAT1	p2537, Sol 180
178	1M143991176	Holman_3	Diamond Jenness	Rock	16	O	S	PostRAT2	None
179	1M144073802	Holman_3	Diamond Jenness	Rock	1	O	M	PostMB	p2537, Sol 180
181	1M144251105	Wilbur	NA	Razorback	14	O	S	NA	p2599, Sol 174
182	1M144339348	Campbell	Mackenzie	Rock	16	O	S	PreRAT	p2404, Sol 177
184	1M144516877	Campbell	Mackenzie	Rock	16	O	S	PostRAT	p2544, Sol 184
186	1M144694762	Tuktoyuktuk_2	Inuvik	Rock	16	O	S	PreRAT	p2545, Sol 186
188	1M144872486	Tuktoyuktuk_2	Inuvik	Rock	16	O	S	PostRAT	p2547, Sol 188
190	1M145040248	Diagnostic sequence	NA	NA	1	C	M	Stowed	None
191	1M145129332	Diagnostic sequence	NA	NA	2	C	M	Stowed	None

Table A1. (continued)

Sol	Starting Image ID	Target	Feature	Target Type	No. ^a	CS ^b	S/M ^c	Relation to RAT/MB ^d	Pancam Sequence ^e
192	1M145218357	Diagnostic sequence	NA	NA	3	C	M	Stowed	None
193	1M145306274	Diagnostic sequence	NA	NA	4	C	M	NA	None
194	1M145395042	Diagnostic sequence	NA	NA	14	C	M	NA	None
194	1M145404757	Bylot	Axel Heiberg	Rock	16	O	S	PreRAT	p2548, Sol 193
195	1M145483830	Diagnostic sequence	NA	NA	10	C	M	NA	None
195	1M145494624	Bylot	Axel Heiberg	Rock	16	O	S	PostRAT	p2551 Sol 195
196	1M145582021	Diagnostic sequence	NA	NA	8	O	M	NA	None
197	1M145671814	Diagnostic sequence	NA	NA	6	O	M	NA	None
197	1M145671944	Sermilik	South_Bylot	Rock	16	O	S	PreMB	p2555, Sol 199
198	1M145759658	Diagnostic sequence	NA	NA	5	C	M	NA	None
198	1M145775434	Sermilik	South_Bylot	Rock	1	O	M	PostMB	p2556, Sol 200
199	1M145849155	Diagnostic sequence	NA	NA	8	C	M	NA	None
199	1M145849586	Berry Fondue	Muffins	Rocks	4	O	S	NA	p2553, Sol 197
199	1M145850034	Jiffy Pop	Muffins	Rocks	16	O	S	PreRAT	p2553, Sol 197
199	1M145852528	Jiffy Pop	Muffins	Rocks	16	O	S	PostRAT	p2555, Sol 199
200	1M145938896	Diagnostic sequence	NA	NA	6	C	M	NA	None
210	1M146814536	Diagnostic sequence	NA	NA	12	C	M	NA	None
210	1M146827327	Afar	Escher	Rock	3	O	M	NA	p2423, Sol 208
210	1M146827625	Jibuti	Escher	Rock	3	O	M	NA	p2423, Sol 208
210	1M146827984	Mondrian	Escher	Rock	3	O	M	NA	p2423, Sol 208
210	1M146828308	Kandinsky	Escher	Rock	3	O	M	NA	p2423, Sol 208
210	1M146828625	Klee	Escher	Rock	3	O	M	NA	p2423, Sol 208
210	1M146828953	Kirchner	Escher	Rock	3	O	M	PreRAT	p2423, Sol 208
210	1M146829297	Feininger	Escher	Rock	3	O	M	NA	p2423, Sol 208
210	1M146829609	Penrose	Escher	Rock	3	O	M	NA	p2423, Sol 208
212	1M147005150	Afar2	Escher	Rock	1	O	M	NA	p2423, Sol 208
212	1M147005587	Macke	Escher	Rock	3	O	M	NA	p2423, Sol 208
212	1M147005805	Munch	Escher	Rock	12	O	S	NA	p2423, Sol 208
212	1M147006540	FranzMarc	Escher	Rock	6	O	S	NA	p2423, Sol 208
212	1M147006944	Jibuti2	Escher	Rock	12	O	S	NA	p2423, Sol 208
212	1M147007732	Leger	Escher	Rock	6	O	S	NA	p2423, Sol 208
212	1M147008140	Penrose	Escher	Rock	22	O	S	NA	p2423, Sol 208
212	1M147009691	Mondrian2	Escher	Rock	18	O	S	NA	p2423, Sol 208
214	1M147179974	Barlach_3	Escher	Rock	14	O	S	NA	p2573, Sol 214
214	1M147182851	EmilNolde2	Escher	Rock	12	O	S	PostBrush	p2576, Sol 217
214	1M147186322	Kirchner_3	Escher	Rock	12	O	S	PostBrush	p2576, Sol 217
216	1M147358380	Fritz	Escher	Rock	1	O	M	PostMB	p2571, Sol 214
217	1M147449328	OttoDix	Escher	Rock	4	O	M	PostBrush	p2576, Sol 217
217	1M147450170	EmilNolde	Escher	Rock	1	O	M	NA	p2576, Sol 217
218	1M147534910	EmilNolde	Escher	Rock	1	O	M	NA	p2423, Sol 208
219	1M147627778	Kirchner	Escher	Rock	12	O	S	PostRAT	p2582, Sol 220
219	1M147628934	EmilNolde	Escher	Rock	6	O	M	NA	p2423, Sol 208
221	1M147801692	Cluster 1	Berry Cluster	Soil	4	O	S	NA	p2425, Sol 220
221	1M147802247	Cluster 2	Berry Cluster	Soil	4	O	S	NA	p2425, Sol 220
221	1M147802811	Cluster 3	Berry Cluster	Soil	4	O	S	NA	p2425, Sol 220
222	1M147892861	Jawlensky	Berry Cluster	Soil	3	O	M	NA	p2425, Sol 220
222	1M147893081	Duchamp	Berry Cluster	Soil	3	O	M	NA	p2425, Sol 220
235	1M149055213	MB on Berry Cluster	Berry Cluster	Soil	3	O	M	PostMB	p2586, Sol 235
236	1M149144118	Auk	NA	Soil	3	O	M	PostRAT	p2587, Sol 236
238	1M149323195	Aukling	NA	Soil	3	O	M	PostMB	p2588, Sol 237
239	1M149399471	Target_4	Ellesmere	Rock	20	O	S	NA	p2421, Sol 207
239	1M149400926	Brads_B	Ellesmere	Rock	3	O	M	NA	p2421, Sol 207
239	1M149401329	No_Coating	Ellesmere	Rock	3	O	M	NA	p2421, Sol 207
240	1M149488339	Barbeau_3	Ellesmere	Rock	3	O	M	NA	p2421, Sol 207
241	1M149576969	Tuck_1 (Jeffs_tuck1)	Ellesmere	Rock	3	O	M	NA	p2574, Sol 215
241	1M149577357	Brads_e (Jeffs_e)	Ellesmere	Rock	3	O	M	NA	p2574, Sol 215
241	1M149577694	Brads_c	Ellesmere	Rock	3	O	M	NA	p2574, Sol 215
244	1M149843462	Lynéal_2	Welshampton	Soil	3	O	M	NA	p2111, Sol 220
244	1M149843780	Llangollen	Welshampton	Soil	3	O	M	NA	p2111, Sol 220
244	1M149844096	Platt_lane	Welshampton	Soil	3	O	M	NA	p2111, Sol 220
249	1M150287403	void for MB/APXS	Rocknest	Soil	1	O	M	NA	p2595, Sol 249
257	1M150997709	Dogrib	Tlcho_2	Soil	15	O	S	NA	p2532, Sol 257
258	1M151088588	Otter	Wopmay	Rock	20	O	S	PreMB	p2533, Sol 258
258	1M151090220	Jenny	Wopmay	Rock	20	O	S	NA	p2533, Sol 258
258	1M151091865	Hiller	Wopmay	Rock	20	O	S	NA	p2533, Sol 258
259	1M151175070	Jet Ranger2	Wopmay	Rock	20	O	S	NA	p2533, Sol 258
259	1M151176732	Twin_Otter	Wopmay	Rock	20	O	S	NA	p2533, Sol 258
262	1M151444557	Hercules	Wopmay	Rock	17	O	S	NA	p2533, Sol 258
273	1M152419233	Filter Magnet	Rover	Magnet	1	O	M	NA	p2428, Sol 244
279	1M152950634	Capture Magnet	Rover	Magnet	1	O	M	NA	p2440, Sol 278
282	1M153216850	Wanganui	NA	Rock	20	O	S	NA	p2539, Sol 283
305	1M155258733	Paikaea	BlackCow	Rock	24	O	S	PreBrush	p2556, Sol 306

Table A1. (continued)

Sol	Starting Image ID	Target	Feature	Target Type	No. ^a	CS ^b	S/M ^c	Relation to RAT/MB ^d	Pancam Sequence ^e
305	1M155260302	Wharenhui	BlackCow	Rock	24	O	S	PreBrush	p2558, Sol 310
305	1M155262242	Contact	BlackCow	Rock	12	O	S	PreBrush	p2350, Sol 312
306	1M155347644	Paikea	BlackCow	Rock	3	O	M	PreRAT	p2554, Sol 305
306	1M155354110	Paikea	BlackCow	Rock	24	O	S	PostRAT	p2132, Sol 306
307	1M155446235	Wharenhui	BlackCow	Rock	24	O	S	PostRAT	p2135, Sol 307
310	1M155703832	Kahu	BlackCow	Rock	24	O	S	NA	p2350, Sol 312
310	1M155705468	Pohutu	BlackCow	Rock	24	O	S	NA	p2350, Sol 312
311	1M155796685	Wharenhui	BlackCow	Rock	24	O	S	PostRAT #2	p2138, Sol 311
319	1M156502186	1A	Tracks	Soil	10	O	S	NA	p2571, Sol 319
319	1M156502975	2A	Tracks	Soil	10	O	S	NA	p2571, Sol 319
321	1M156679106	Tilted_contact2	Solar Panel	Rover	12	O	M	NA	p2275, Sol 292
328	1M157300520	Capture Magnet	Rover	Magnet	2	O	M	N/A	p2363, Sol 333
334	1M157833767	Left_edge to Right_edge	Heatshield	Heatshield	15	O	S	NA	p2580, Sol 331
334	1M157834885	Upper_left_edge	Heatshield	Heatshield	7	O	M	NA	p2363, Sol 333
334	1M157835453	Upper_right_edge	Heatshield	Heatshield	7	O	M	NA	p2363, Sol 333
337	1M158099569	Capture Magnet	Rover	Magnet	1	O	M	NA	p2363, Sol 333
337	1M158099874	Strawman	Flankshield edge	Heatshield	20	O	S	NA	p2363, Sol 333
341	1M158454638	Strawman	Flankshield edge	Heatshield	84	O	S	NA	p2536, Sol 358
341	1M158461880	Filter Magnet	Rover	Magnet	2	O	M	NA	p2536, Sol 358
347	1M158987338	Squidward	SpongeBob Rock	Meteororite	20	O	S	NA	p2591, Sol 346
349	1M159166786	Squidward	SpongeBob Rock	Meteororite	18	O	S	PostBrush	p2596, Sol 352
352	1M159431039	Plankton	SpongeBob Rock	Meteororite	6	O	S	NA	p2596, Sol 352
352	1M159431435	Patrick	SpongeBob Rock	Meteororite	6	O	S	NA	p2596, Sol 352
356	1M159790263	Mosaic	Heatshield	Heatshield	54	C	S	NA	p2585, Sol 344
358	1M159963976	Stack 1	Heatshield	Heatshield	6	O	S	NA	p2585, Sol 344
358	1M159964549	Stack 4	Heatshield	Heatshield	6	O	S	NA	p2585, Sol 344
367	1M160762814	Dr_Bob	Trench	Soil	6	O	S	NA	p2550, Sol 367
367	1M160777622	Sky Flat	NA	Sky	1	O	M	NA	None
367	1M160777676	Sky Flat	NA	Sky	1	C	M	NA	None
368	1M160851441	Left_Of_Peanut	Trench_Ripple	Soil	3	O	M	PostMB	p2374, Sol 372
368	1M160851712	Ripple_Crest2b	Trench_Ripple	Soil	6	O	S	NA	p2550, Sol 367
369	1M160940162	Ripple_Crest2b	Trench_Ripple	Soil	3	O	M	PostMB	p2550, Sol 367
369	1M160940408	Caviar_Tweaked	Trench_Ripple	Soil	5	O	S	NA	p2550, Sol 367
370	1M161025869	Caviar_Tweaked	Trench_Ripple	Soil	12	O	S	PostAPXS	p2374, Sol 372
371	1M161124667	Dr_Bob	Trench	Soil	6	O	S	NA	p2550, Sol 367
372	1M161206695	Scruffy	Trench	Soil	5	O	S	PreMB	None
373	1M161305508	Scruffy	Trench	Soil	3	O	M	PostMB	p2551, Sol 373
381	1M162002974	BridgeOfNose	Russet	Rock	4	O	M	NA	p2557, Sol 381
381	1M162003290	Eye	Russet	Rock	4	O	M	NA	p2557, Sol 381
392	1M162982278	Omaha	Normandy	Rock	8	O	S	PreMB	p2569, Sol 394
400	1M163692299	Laika	Yuri	Rock	5	O	S	NA	p2570, Sol 401
400	1M163692601	Gagarin	Yuri	Rock	16	O	S	PreBrush	None
401	1M163783449	Gagarin	Yuri	Rock	17	O	S	PostBrush	p2570, Sol 401
403	1M163958457	Gagarin	Yuri	Rock	20	O	S	PostRAT	p2578, Sol 405
415	1M165025801	Mobarek	Ripple	Soil	12	O	S	PostMB	p2584, Sol 415
419	1M165379069	Norooz	Ripple	Ripple Crest	16	O	S	PostMB	p2585, Sol 421
420	1M165468145	Mayberooz	Ripple	Ripple Crest	20	O	S	PostMB	p2585, Sol 421
443	1M167510235	Cure	Recovery_Soil	Rock	25	O	S	PostMB	p2598, Sol 446
443	1M167509641	Sky Flat	NA	Sky	1	C	M	NA	p2678, Sol 443
498	1M172392189	New_Track_Adjusted_Normal	North Dune	Soil	3	O	M	NA	p2553, Sol 498
498	1M172392548	New_Face	North Dune	Soil	24	O	S	NA	p2553, Sol 498
498	1M172394680	New_Crest_Section	North Dune	Soil	13	O	S	NA	p2553, Sol 498
505	1M173015987	OldTrack	Purgatory	Tracks	6	O	S	NA	p2542, Sol 480
505	1M173016762	TroughPlain	Purgatory	Soil	16	O	S	NA	p2542, Sol 480
507	1M173191265	Flank1	Purgatory	Soil	24	O	S	PostMB	p2561, Sol 510
507	1M173193120	Track2	Purgatory	Tracks	24	O	S	PostMB	p2558, Sol 504
510	1M173457453	Cleat_Tab	Purgatory	Tracks	6	O	S	NA	p2561, Sol 510
510	1M173457920	Torment_Track	Purgatory	Tracks	6	O	S	NA	p2558, Sol 504
538	1M175943090	Solar Panel	Solar Panel	Rover	12	O	S	NA	p2570, Sol 538
538	1M175944388	Filter Magnet	Rover	Magnet	2	O	M	NA	None
544	1M176475875	OneScoop	Ice Cream	Rock	32	O	S	PreRAT	p2351, Sol 543
544	1M176477935	Cone	Ice Cream	Rock	24	O	S	NA	p2351, Sol 543
545	1M176565126	OneScoop	Ice Cream	Rock	24	O	S	PostBrush	p2572, Sol 544
546	1M176653418	OneScoop	Ice Cream	Rock	8	O	S	PostRAT	p2577, Sol 549
549	1M176920001	OneScoop	Ice Cream	Rock	16	O	S	PostRAT	p2577, Sol 549
551	1M177097312	Arkansas	Cobbles	Cobbles	6	O	S	PreMB	p2579, Sol 550
551	1M177097714	Reinner Gauss	Cobbles	Soil	6	O	S	NA	p2579, Sol 550
552	1M177193311	Reinner Gauss	Cobbles	Soil	4	O	M	NA	p2579, Sol 550
554	1M177373140	Reinner Gauss	Cobbles	Soil	4	O	M	NA	p2579, Sol 550
554	1M177373436	Perseverance	Cobbles	Rock	7	O	S	NA	p2583, Sol 555
555	1M177452357	Reinergamma Squash	Cobbles	Cobbles	6	O	S	PostMB	p2583, Sol 555
556	1M177542286	Lemon Rind	Fruitbasket	Rock	24	O	S	PreBrush	p2584, Sol 556

Table A1. (continued)

Sol	Starting Image ID	Target	Feature	Target Type	No. ^a	CS ^b	S/M ^c	Relation to RAT/MB ^d	Pancam Sequence ^e
556	1M177546448	Lemon Rind	Fruitbasket	Rock	24	O	S	PostBrush	p2585, Sol 556
558	1M177725854	Strawberry_RAT	Fruitbasket	Rock	5	O	S	PreRAT	p2584, Sol 556
558	1M177729682	Strawberry_RAT	Fruitbasket	Rock	20	O	S	PostRAT	p2591, Sol 561
560	1M177905696	Lemon Rind	Fruitbasket	Rock	24	O	S	PostRAT	p2591, Sol 561
561	1M177984943	Strawberry_RAT	Fruitbasket	Rock	1	O	M	PostRAT	p2591, Sol 561
593	1M180828164	Penguin	Elephant	Rock	6	O	S	PostBrush	p2595, Sol 593
598	1M181272513	Kendall	Deception	Rock	24	O	S	PostMB	None
633	1M184376888	Kalavrita	Olympia	Rock	20	O	S	PreRAT	p2143, Sol 633
633	1M184381719	Kalavrita	Olympia	Rock	20	O	S	PostRAT	p2562, Sol 639
638	1M184820806	Lashiti	Olympia	Rock	3	O	M	NA	p2562, Sol 639
638	1M184823465	Ziakas	Olympia	Rock	24	O	S	PostBrush	p2562, Sol 639
641	1M185092422	Antistasi	Olympia	Rock	32	O	S	PreMB	p2570, Sol 645
647	1M185621425	CCT	Rover	Rover	5	O	M	PreMB	None
649	1M185797617	Jerome_mod	Olympia	Rock	6	O	S	NA	None
649	1M185798015	Heber	Olympia	Rock	6	O	S	NA	None
654	1M186241681	IDD Unstow Fault	IDD Unstow Fault	IDD Fault	60	C	M	NA	None
659	1M186695172	IDD Unstow Fault	IDD Unstow Fault	IDD Fault	2	C	M	NA	None
660	1M186783478	IDD Unstow Fault	IDD Unstow Fault	IDD Fault	3	C	M	NA	None
661	1M186870220	IDD Unstow Fault	IDD Unstow Fault	IDD Fault	2	C	M	NA	None
664	1M187313971	IDD Unstow Fault	IDD Unstow Fault	IDD Fault	4	C	M	NA	None
667	1M187414115	IDD Unstow Fault	IDD Unstow Fault	IDD Fault	1	C	M	NA	None
668	1M187473647	IDD Unstow Fault	IDD Unstow Fault	IDD Fault	2	C	M	NA	None
671	1M187750968	Williams	Olympia	Rock	6	O	S	NA	p2585, Sol 661
673	1M187928269	Williams	Olympia	Rock	4	O	M	NA	p2585, Sol 661
677	1M188282853	Williams	Olympia	Rock	12	O	M	NA	p2585, Sol 661
679	1M188460876	Ted	Rimrock	Rock	24	O	S	PreBrush	None
684	1M188904882	Ted	Rimrock	Rock	24	O	S	PostBrush	None
686	1M189086032	Hunt	Rinrock	Rock	12	O	S	NA	None
691	1M189529263	Ted	Rimrock	Rock	24	O	S	PostRAT	P2567, Sol 691
697	1M190076212	Sky Flat	NA	Sky	1	O	M	NA	p2888, Sol 697
697	1M190076266	Sky Flat	NA	Sky	1	C	M	NA	p2888, Sol 697
708	1M191044935	Scotch	Overgaard (lower)	Rock	72	O	S	NA	p2580, Sol 708
714	1M191579848	Scotch_mod (Doublemalt)	Overgaard (lower)	Rock	36	O	M	NA	p2580, Sol 708
715	1M191668551	Branchwater	Overgaard (lower)	Rock	36	O	S	NA	p2580, Sol 708
716	1M191759857	Bourbon	Overgaard (lower)	Rock	36	O	S	NA	p2580, Sol 708
719	1M192011534	DonGiovanni	Overgaard (upper)	Rock	6	O	S	NA	p2580, Sol 708
719	1M192011823	DonGiovanni	Overgaard (upper)	Rock	6	O	S	NA	p2580, Sol 708
719	1M192022228	Salzburg-Nachtmusich	Overgaard (upper)	Rock	60	O	S	NA	p2580, Sol 708
721	1M192199876	Salzburg	Overgaard (upper)	Rock	54	O	S	NA	p2580, Sol 708
723	1M192377404	Salzburg	Overgaard (upper)	Rock	54	O	S	NA	p2580, Sol 708
727	1M192731134	Rough_Rider	Roosevelt	Rock	24	O	S	NA	p2595, Sol 725
727	1M192379647	Bull_Moose	Roosevelt	Rock	24	O	S	NA	p2595, Sol 725
727	1M192382573	Falla	Roosevelt	Soil	12	O	S	NA	p2595, Sol 725
727	1M192382752	Panama_Canal	Roosevelt	Soil	8	O	S	NA	p2532, Sol 729
732	1M193165650	Vicos	Bellmont	Rock	7	O	S	NA	p2441, Sol 674
732	1M193175681	Tara	Bellmont	Rock	16	O	S	NA	p2441, Sol 674
732	1M193176805	Chaco	Bellmont	Rock	6	O	S	NA	p2441, Sol 674
733	1M193264508	Verdun	Bellmont	Rock	12	O	S	NA	p2441, Sol 674
791	1M198405616	Buffalo Springs	NA	Rock	6	O	S	PostBrush	p2575, Sol 792
804	1M199557346	Brookville	Default	Rock	12	O	S	PreBrush	None
806	1M199734920	Brookville	Default	Rock	24	O	S	PostBrush	p2588, Sol 807
811	1M200179063	Pecos River	NA	Ripple banding	29	O	S	NA	p2592, Sol 813
811	1M200181202	Fort Sumner	NA	Ripple banding	30	O	S	NA	p2592, Sol 813
818	1M200800253	Cheyenne	Pueblo Loco?	Rock	6	O	S	PreBrush	None
819	1M200888996	Cheyenne	Pueblo Loco?	Rock	24	O	S	PostBrush	p2595, Sol 821
825	1M201422806	Alamogordo Creek	Shawnee Trail	NA	8	O	S	NA	p2596, Sol 825
826	1M201510475	Grenada	Shawnee Trail	NA	6	O	S	NA	None
879	1M206216366	Westport	NA	Rock	6	O	S	NA	p2548, Sol 879
880	1M206304356	Fort Graham	NA	Soil	6	O	S	NA	p2548, Sol 880
886	1M206837038	Joseph McCoy	Jesse Chisholm	Cobbles	32	O	S	NA	p2906, Sol 886
886	1M206839061	Haiwassee	Jesse Chisholm	Cobbles	8	O	S	NA	p2906, Sol 886
886	1M206839638	Ignatius	Jesse Chisholm	Cobbles	8	O	S	NA	p2906, Sol 886
893	1M207460999	Baltra	Beagle	Rock	5	O	M	PostMB	p2131, Sol 893
894	1M207547188	Baltra	Beagle	Rock	24	O	S	PostRAT	p2558, Sol 896

^aNo. is number of images in stack.^bCS is dust cover state (C is closed, O is open).^cS/M is stereo (S) or monoscopic (M) observation.^dRAT/MB is Rock Abrasion Tool or Mössbauer observation.^ePancam sequence is best multispectral observation of same target.

Appendix A

[91] Targets observed by the MI were often also observed by Pancam and sometimes by the other IDD instruments as well. Table A1 summarizes MI observations during the first 900 sols of Opportunity's mission and shows the relationship of each MI observation to RAT or Mössbauer (MB) [Klingelhöfer *et al.*, 2003] observations of the same target. The far right column lists the sequence ID and sol of acquisition of Pancam images of the same target. In some cases, the target was modified by the RAT or MB contact but not observed by Pancam after the modification; in these cases the entry is "none."

[92] **Acknowledgments.** We thank the MER rover planners for their outstanding support of Opportunity IDD operations: Brian K. Cooper, Jeff Biesiadecki, Frank Hartman, Scott Maxwell, John Wright, Jeng Yen, Chris Leger, Robert Bonitz, Eric Baumgartner, Khaled Ali, Ashitey Trebi-Ollennu, and Mark Maimone. We also thank the NASA Ames MER support team: Matthew Deans, Laurence Edwards, Joel Hagen, Clayton Kunz, David Lees, Randy Sargent, Michael Wagner, and Anne Wright. Software tools developed at Cornell University by the Pancam team continue to be very useful in tracking and managing MI data products; we thank Elaina McCartney for her repeated assistance in operations planning. The MIPL MER team quickly generated many MI mosaics: Doug Alexander, Amy Chen, Oleg Pariser, Bob Deen, Jeff Hall, Mike Cayan, Vadim Klocho, Elmain Martinez, and Charles Thompson. We also appreciate the support received from the MER team at the USGS in Flagstaff: Jeff Anderson, Tammy Becker, Chris Isbell, Brian Lipkowitz, Dave MacKinnon, Jac Shinaman, Deborah Soltesz, Sean Varga, and Robert Wallace. Boris Semenov of JPL's Navigation and Ancillary Information Facility supported MI geometric processing by providing SPICE kernels in a timely fashion. This work was performed for the Jet Propulsion Laboratory, California Institute of Technology, sponsored by the National Aeronautics and Space Administration. The use of trade, product, or firm names in this paper does not imply endorsement by the U.S. Government.

References

- Ahlbrandt, T. S. (1979), Textural parameters of eolian deposits, *U.S. Geol. Surv. Prof. Pap.*, 1052, 21–52.
- Alexander, D. A., et al. (2006), Processing of Mars Exploration Rover imagery for science and operations planning, *J. Geophys. Res.*, *111*, E02S02, doi:10.1029/2005JE002462.
- Arvidson, R. E., et al. (2004), Localization and physical property experiments conducted by Opportunity at Meridiani Planum, *Science*, *306*, 1730–1733, doi:10.1126/science.1104211.
- Bell, J. F., III, et al. (2003), Mars Exploration Rover Athena Panoramic Camera (Pancam) investigation, *J. Geophys. Res.*, *108*(E12), 8063, doi:10.1029/2003JE002070.
- Bell, J. F., III, J. Joseph, J. N. Sohl-Dickstein, H. M. Arneson, M. J. Johnson, M. T. Lemmon, and D. Savransky (2006), In-flight calibration and performance of the Mars Exploration Rover Panoramic Camera (Pancam) instruments, *J. Geophys. Res.*, *111*, E02S03, doi:10.1029/2005JE002444.
- Calvin, W. M., et al. (2008), Hematite spherules at Meridiani: Results from MI, Mini-TES, and Pancam, *J. Geophys. Res.*, doi:10.1029/2007JE003048, in press.
- Carlson, J., and J. P. Grotzinger (2001), Submarine fan environment inferred from turbidite thickness distributions, *J. Sediment. Res.*, *48*, 1331–1351, doi:10.1046/j.1365-3091.2001.00426.x.
- Choquette, P. W., and L. C. Pray (1970), Geologic nomenclature and classification of porosity in sedimentary carbonates, *Am. Assoc. Pet. Geol. Bull.*, *54*, 207–250.
- Clark, B. C., et al. (2005), Chemistry and mineralogy of outcrops at Meridiani Planum, *Earth Planet. Sci. Lett.*, *240*, 73–94, doi:10.1016/j.epsl.2005.09.040.
- Connolly, H. C., Jr., et al. (2006), The meteoritical bulletin, no. 90, 2006 September, *Meteorit. Planet. Sci.*, *41*(9), 1383–1418.
- Crisp, J. A., M. Adler, J. R. Matijevic, S. W. Squyres, R. E. Arvidson, and D. M. Kass (2003), Mars Exploration Rover mission, *J. Geophys. Res.*, *108*(E12), 8061, doi:10.1029/2002JE002038.
- Gorevan, S. P., et al. (2003), Rock Abrasion Tool: Mars Exploration Rover mission, *J. Geophys. Res.*, *108*(E12), 8068, doi:10.1029/2003JE002061.
- Greeley, R., and J. D. Iversen (1985), *Wind as a Geological Process*, 333 pp., Cambridge Univ. Press, Cambridge, U. K.
- Grotzinger, J. P., et al. (2005), Stratigraphy and sedimentology of a dry to wet eolian depositional system, Burns formation, Meridiani Planum, Mars, *Earth Planet. Sci. Lett.*, *240*, 11–72, doi:10.1016/j.epsl.2005.09.039.
- Grotzinger, J., et al. (2006), Sedimentary textures formed by aqueous processes, Erebus Crater, Meridiani Planum, Mars, *Geology*, *34*, 1085–1088, doi:10.1130/G22985A.1.
- Herkenhoff, K. E., et al. (2003), Athena Microscopic Imager investigation, *J. Geophys. Res.*, *108*(E12), 8065, doi:10.1029/2003JE002076.
- Herkenhoff, K., et al. (2004a), Mars Exploration Rover Project Microscopic Imager calibration report, *Rev. B. D-19830, MER 420–6-704*, Jet Propul. Lab., Pasadena, Calif.
- Herkenhoff, K. E., et al. (2004b), Evidence from Opportunity's Microscopic Imager for water on Meridiani Planum, *Science*, *306*, 1727–1730, doi:10.1126/science.1105286.
- Herkenhoff, K. E., et al. (2006), Overview of the Microscopic Imager investigation during Spirit's first 450 sols in Gusev Crater, *J. Geophys. Res.*, *111*, E02S04, doi:10.1029/2005JE002574.
- Jolliff, B. L., W. H. Farrand, J. R. Johnson, C. Schröder, C. M. Weitz, and the Athena Science Team (2006), Origin of rocks and cobbles on the Meridiani Plains as seen by Opportunity, *Lunar Planet. Sci.*, XXXVII, Abstract 2401.
- Klingelhöfer, G., et al. (2003), The Athena MIMOS II Mössbauer spectrometer investigation, *J. Geophys. Res.*, *108*(E12), 8067, doi:10.1029/2003JE002138.
- Klingelhöfer, G., et al. (2004), Jarosite and hematite at Meridiani Planum from Opportunity's Mössbauer spectrometer, *Science*, *306*, 1740–1746, doi:10.1126/science.1104653.
- Knauth, L. P., D. M. Burt, and K. H. Wohletz (2005), Impact origin of sediments at the Opportunity landing site on Mars, *Nature*, *438*, 1123–1128, doi:10.1038/nature04383.
- Knoll, A. H., et al. (2008), Veneers, rinds, and fracture fills: Relatively late alteration of sedimentary rocks at Meridiani Planum, Mars, *J. Geophys. Res.*, *113*, E06S16, doi:10.1029/2007JE002949.
- Lewis, K., A. Aharonson, J. P. Grotzinger, and S. W. Squyres (2008), Structure and stratigraphy of Home Plate from the Spirit Mars Exploration Rover, *J. Geophys. Res.*, doi:10.1029/2007JE003025, in press.
- Maki, J. N., et al. (2003), The Mars Exploration Rover engineering cameras, *J. Geophys. Res.*, *108*(E12), 8071, doi:10.1029/2003JE002077.
- McCormack, T. M., and B. M. Hynek (2005), A volcanic environment for bedrock diagenesis at Meridiani Planum on Mars, *Nature*, *438*, 1129–1131, doi:10.1038/nature04390.
- McLennan, S. M., et al. (2005), Provenance and diagenesis of the evaporate-bearing Burns formation, Meridiani Planum, Mars, *Earth Planet. Sci. Lett.*, *240*, 95–121, doi:10.1016/j.epsl.2005.09.041.
- Metz, J. M., J. P. Grotzinger, D. M. Rubin, K. Lewis, S. W. Squyres, and J. F. Bell III (2008), Sulfate-rich eolian and wet interdune deposits, Erebus Crater, Meridiani Planum, Mars, *J. Sediment. Res.*, in press.
- Morris, R. V., et al. (2006), Mössbauer mineralogy of rock, soil, and dust at Meridiani Planum, Mars: Opportunity's journey across sulfate-rich outcrop, basaltic sand and dust, and hematite lag deposits, *J. Geophys. Res.*, *111*, E12S15, doi:10.1029/2006JE002791.
- Perl, S. M., S. M. McLennan, J. P. Grotzinger, K. E. Herkenhoff, and the Athena Science Team (2007), Sedimentological constraints on an infiltrating paleowater table in the Burns formation, Meridiani Planum, Mars, *Seventh International Conference on Mars*, Abstract 3298, Jet Propul. Lab., Pasadena, Calif.
- Powers, M. (1953), A new roundness scale for sedimentary particles, *J. Sediment. Res.*, *23*, 117–119.
- Reid, R. J., et al. (1999), Imager for Mars Pathfinder (IMP) image calibration, *J. Geophys. Res.*, *104*, 8907–8926, doi:10.1029/1998JE000011.
- Rothman, D. H., and J. P. Grotzinger (1995), Scaling properties of gravity-driven sediments, *Nonlinear Processes Geophys.*, *2*, 178–185.
- Schröder, C., et al. (2008), Meteorites on Mars observed with the Mars Exploration Rovers, *J. Geophys. Res.*, *113*, E06S22, doi:10.1029/2007JE002990.
- Soderblom, J. M., J. F. Bell III, J. R. Johnson, J. Joseph, and M. J. Wolff (2008), Mars Exploration Rover Navigation Camera in-flight calibration, *J. Geophys. Res.*, *113*, E06S19, doi:10.1029/2007JE003003.
- Soderblom, L. A., et al. (2004), Soils of Eagle Crater and Meridiani Planum at the Opportunity Rover landing site, *Science*, *306*, 1723–1726, doi:10.1126/science.1105127.
- Southard, J. B., and L. A. Boguchwal (1990), Bed configuration in steady unidirectional water flows: Part 2. Synthesis of flume data, *J. Sediment. Res.*, *60*, 658–679.
- Sparks, R. S. J. (1976), Grain-size variations in ignimbrites and implications for transport of pyroclastic flows, *Sedimentology*, *23*, 147–188, doi:10.1111/j.1365-3091.1976.tb00045.x.
- Squyres, S. W., and A. H. Knoll (2005), Sedimentary rocks at Meridiani Planum: Origin, diagenesis, and implications for life on Mars, *Earth Planet. Sci. Lett.*, *240*, 1–10, doi:10.1016/j.epsl.2005.09.038.

- Squyres, S. W., et al. (2003), The Mars Exploration Rover Athena investigation, *J. Geophys. Res.*, *108*(E12), 8062, doi:10.1029/2003JE002121.
- Squyres, S. W., et al. (2004a), The Opportunity Rover's Athena science investigations at Meridiani Planum, Mars, *Science*, *306*, 1698–1703, doi:10.1126/science.1106171.
- Squyres, S. W., et al. (2004b), In situ evidence for an ancient aqueous environment at Meridiani Planum, Mars, *Science*, *306*, 1709–1714, doi:10.1126/science.1104559.
- Squyres, S. W., et al. (2006), Two years at Meridiani Planum: Results from the Opportunity Rover, *Science*, *313*, 1403–1407, doi:10.1126/science.1130890.
- Sullivan, R., et al. (2005), Aeolian processes at the Mars Exploration Rover Meridiani Planum landing site, *Nature*, *436*, 58–61, doi:10.1038/nature03641.
- Sullivan, R., R. Arvidson, J. Grotzinger, A. Knoll, M. Golombek, B. Jolliff, S. Squyres, and C. Weitz (2007), Aeolian geomorphology with MER Opportunity at Meridini Planum, Mars, *Lunar Planet. Sci.*, *XXXVIII*, Abstract 2048.
- Tucker, M. E. (1981), *Sedimentary Petrology*, 252 pp., Blackwell Sci., New York.
- Weitz, C. M., R. C. Anderson, J. F. Bell III, W. H. Farrand, K. E. Herkenhoff, J. R. Johnson, B. L. Jolliff, R. V. Morris, S. W. Squyres, and R. J. Sullivan (2006), Soil grain analyses at Meridiani Planum, Mars, *J. Geophys. Res.*, *111*, E12S04, doi:10.1029/2005JE002541.
- Yen, A. S., et al. (2005), An integrated view of the chemistry and mineralogy of Martian soils, *Nature*, *436*, 49–54, doi:10.1038/nature03637.
- B. A. Archinal, J. M. Barrett, K. J. Becker, M. G. Chapman, D. Cook, L. R. Gaddis, D. M. Galuszka, P. A. Garcia, P. Geissler, T. M. Hare, K. E. Herkenhoff, E. Howington-Kraus, J. R. Johnson, L. Keszthelyi, R. L. Kirk, E. M. Lee, K. F. Mullins, B. L. Redding, M. R. Rosiek, L. A. Soderblom, R. M. Sucharski, T. Sucharski, and J. M. Torson, Astrogeology Team, U.S. Geological Survey, Flagstaff, AZ 86001, USA. (kherkenhoff@usgs.gov)
- R. E. Arvidson and B. Ehlmann, Department of Earth and Planetary Sciences, Washington University, St. Louis, MO 63130, USA.
- J. F. Bell III, S. W. Squyres and R. Sullivan, Department of Astronomy, Cornell University, Space Sciences Building, Ithaca, NY 14853, USA.
- J. Grotzinger and D. Stolper, Division of Geological and Planetary Sciences, California Institute of Technology, Pasadena, CA 91125, USA.
- A. H. Knoll, Department of Organismic and Evolutionary Biology, Harvard University, Cambridge, MA 02138, USA.
- P. Lanagan, Lunar and Planetary Laboratory, University of Arizona, Tucson, AZ 85721, USA.
- S. M. McLennan, Department of Geosciences, State University of New York at Stony Brook, Stony Brook, NY 11794, USA.
- M. H. Sims, NASA Ames Research Center, Mail Stop 269-3, Moffett Field, CA 94035, USA.
- C. Weitz, Planetary Science Institute, 1700 East Fort Lowell Road, Tucson, AZ 85719, USA.
- A. Yingst, Department of Natural and Applied Sciences, University of Wisconsin, Green Bay, WI 54311, USA.

R. Anderson, C. Budney, B. Franklin, C. Leff, J. N. Maki, T. J. Parker, N. Spanovich and R. Springer, Jet Propulsion Laboratory, California Institute of Technology, Pasadena, CA 91109, USA.